Deep material networks for the efficient multi-scale simulation of short fiber reinforced plastics under long-term loading

Zur Erlangung des akademischen Grades eines

Doktors der Ingenieurwissenschaften (Dr.-Ing.)

....bei der KIT-Fakultät für Maschinenbau des
Karlsruher Instituts für Technologie (KIT)
angenommene

Dissertation

von

M. Sc. Argha Protim Dey

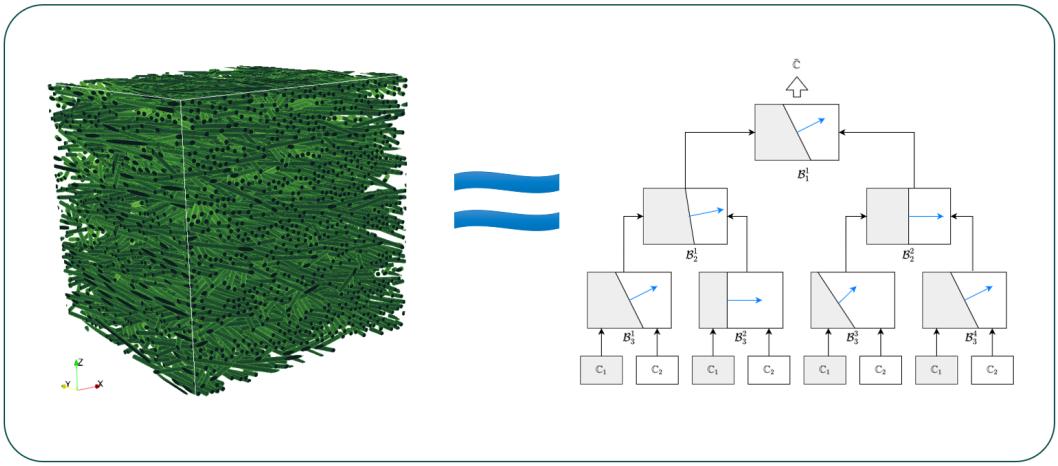

Tag der mündlichen Prüfung: 27. März 2025

Hauptreferent	Prof. Dr. rer. nat. Matti Schneider
Korreferent	Prof. Dr.-Ing. Thomas Böhlke
Korreferent	Prof. Dr. rer. nat. Oliver Weeger

Zusammenfassung

Faserverstärkte Polymere sind eine wachsende Klasse von Materialien, die in industriellen Anwendungen eingesetzt werden. Der Grund dafür ist der Bedarf an leichten Strukturen mit ausreichender struktureller Festigkeit. Ziel dieser Arbeit ist die vollständig virtuelle Charakterisierung von Bauteilen, die aus kurzfaserverstärkten Thermoplasten hergestellt sind und durch Langzeitbelastungen wie Kriechen und Ermüdung beansprucht werden. Diese Werkstoffklasse unterscheidet sich von thermosetbasierten Materialien durch ihre Wiederverwertbarkeit. Außerdem ermöglichen kurze Fasern im Gegensatz zu langen Fasern die einfache und effiziente Herstellung geometrisch komplexer Bauteile.
Eine große Herausforderung für die virtuelle Charakterisierung von kurzglasfaserverstärktern Thermoplastbauteilen ist die inhärente Anisotropie, die sich aus dem Herstellungsprozess ergibt. Eine präzise Beschreibung des Langzeitverhaltens solcher Bauteile erfordert die Betrachtung mehrerer Skalen, sowohl räumlich (aufgrund der verstärkenden Fasern) als auch zeitlich (kurz- und langfristige Deformations- und Schädigungsvorgänge der Polymermatrix). In dieser Arbeit werden Deep Material Networks (DMNs) betrachtet, eine neue Multiskalentechnologie, die es ermöglicht, mit Hilfe leistungsfähiger Ersatzmodelle für das mikromechanische Problem hochpräzise Multiskalensimulationen im industriellen Maßstab durchzuführen. Dies ermöglicht die Einbindung von Mikrostrukturinformationen in eine makroskopische Simulation.
Klassischerweise werden die Parameter der DMNs auf der Grundlage linear elastischer Vorberechnungen ermittelt. Sind die Parameter identifiziert, können DMNs inelastische Materialmodelle für die Einzelphasen verarbeiten und damit sehr effizient die zeitabhängige Materialantwort des Verbundwerkstoffs vorhersagen. Die Genauigkeit dieser Vorhersagen liegt in der gleichen Größenordnung wie die einer numerisch teuren Vollfeldsimulation. Im ersten Teil der Arbeit wird gezeigt, dass die klassische Trainingsstrategie, die nur auf linear-elastischen Vorberechnungen basiert, nicht garantiert, dass DMNs erzeugt werden, die das Langzeit-Kriechverhalten mit zufriedenstellender Genauigkeit

vorhersagen können. Um diesen Nachteil auzumerzen wird eine inelastisch informierte Early-Stop-Methode für das Offline-DMN-Training vorgeschlagen. Darüber hinaus wird eine neuartige Strategie vorgestellt, die auf einem Ersatzmaterialmodell basiert, das die wichtigsten nichtlinearen Effekte mit dem exakten Modell gemeinsam hat, aber in der Analyse wesentlich kostengünstiger ist. Diese Methode ermöglicht eine erhebliche Zeitersparnis in der gesamten Phase der Parameteridentifikation für das jeweilige Problem.
Zur Modellierung des Kriechens in kurzfaserverstärkten Thermoplasten wird weiter ein vollständig gekoppeltes Plastizitäts- und Kriechmodell für die Polymermatrix vorgestellt, um sowohl Plastizität als auch Kriechen auf verschiedenen Zeitskalen zu modellieren. Ist die geometrische Darstellung der Mikrostruktur bekannt, bietet die numerische Mikromechanik eine elegante Möglichkeit den Verbundwerkstoff zu beschreiben und die Stoffgesetze für die Einzelphasen zu kalibrieren. Leider ist die Kalibrierung der konstitutiven Modelle nicht trivial, und zwar im Wesentlichen aus zwei Gründen. Zum einen ist der Werkstoffzustand einer reinen Polymerprobe nicht mit dem Polymerverhalten im Verbund vergleichbar. Außerdem kann der Herstellungsprozess das Materialverhalten verändern. Daher werden, mit einem schnellen Ersatzmodell an der Hand, die Materialmodelle der einzelnen Phasen direkt anhand von Experimenten am Verbundwerkstoff kalibriert. Die DMNs spielen in diesem Zusammenhang eine zentrale Rolle um teure Vollfeldsimulationen zu ersetzen: Eine inverse Parameteroptimierung für das stark nichtlineare Plastizitäts- und Kriechmodell kann effizient durchgeführt werden.
Eine Anwendung der DMNs ist nicht nur auf das Deformationsverhalten von Kunststoffen beschränkt. In einem weiteren Schritt werden die DMNs erweitert um das Schädigungsverhalten von kurzfaserverstärkten Thermoplasten unter Ermüdungsbelastung zu beschreiben. Ein besonderer Fokus liegt auf der Vorherage des Steifigkeitsabbaus unter Ermüdungsbelastung mit Hilfe eines passenden Schädigungsmodells für die Polymermatrix. Dank einer präzisen und numerisch effizienten Auflösung der Mikrostruktur-Eigenschaftsbeziehung sind DMNs dazu in der Lage, das hochgradig nichtlineare Deformations und Versagensverhalten von kurzfaserverstärkten Thermoplasten abzubilden. Es liegt daher nahe, dieses Konzept als generalistischen Ansatz für diese Werkstoffklasse zu betrachten und entsprechend zu erweitern. Zu diesem Zweck erweitern wir das DMN-Rahmenwerk mit einem a posteriori Ansatz zur Interpolation des Faserorientierungstensors. Wir zeigen, dass der DMN-Rahmen es uns ermöglicht, Materialmodelle effektiv zu erweitern und Modellparameter auf der Grundlage von Verbundexperimenten für alle möglichen Orientierungszustände und eine Vielzahl von Materialmodellen

invers zu identifizieren. DMNs bieten uns somit eine umfassende All-inclusive-Lösung für die multiskalige Bewertung von kurzfaserverstärkten Thermoplasten unter Langzeitbelastung.

Summary

Fiber reinforced polymers are a growing class of materials being used in industrial applications. This is driven by the need of light-weight structures with sufficient structural strength. This thesis aims for the complete virtual characterization of components manufactured using short fiber-reinforced thermoplastics (SFRTs) under long-term load cases such as creep and fatigue. This class of materials differs from thermoset-based materials in terms of their recyclability. Furthermore, unlike long fibers, short glass-fibers enable for the simple and efficient fabrication of components with complex geometry.

A key challenge for the virtual characterization of components manufactured using SFRTs is the inherent anisotropy which stems from the manufacturing process. Moreover, in the context of long-term loading, multiple scales appear, both in space (due to the reinforcements) and in time (short- and long-term effects). In this thesis, we make use of deep material networks (DMNs), which are a recent multiscale technology which enable running concurrent multiscale simulations on industrial scale with the help of powerful surrogate models for the micromechanical problem. This enables the incorporation of microstructure information into a macroscopic simulation.

Classically, the parameters of the DMNs are identified based on linear elastic precomputations. Once the parameters are identified, DMNs may process inelastic material models, and were shown to reproduce micromechanical full-field simulations with the original microstructure to high accuracy. However, the first part of the thesis demonstrates that the classical training strategy based on linear elastic precomputations is not guaranteed to produce DMNs whose long-term creep response accurately matches high-fidelity computations. As a remedy, an inelastically-informed early-stopping method for offline DMN training is proposed. Furthermore, we present a novel strategy based on a surrogate material model that shares the main non-linear effects with the exact model but is substantially less expensive to analyze. This method allows for considerable time savings throughout the parameter-identification phase for the problem at hand.

Thereafter, we move to the material modeling of creep in SFRTs and introduce a novel fully coupled plasticity and creep model for the matrix material for modeling both plasticity and creep at different time scales. Micromechanics offers an elegant way to calibrate constitutive models of materials with complex microstructure, as these emerge naturally once an accurate geometrical representation of the microstructure and expressive material models of the constituents forming the material (in our case, the fully coupled plasticity creep model) are known. Unfortunately, calibrating the constitutive model is non-trivial, essentially for two reasons. For a start, experiments on samples with neat polymer may not accurately represent the conditions present in the composite. Moreover, the manufacturing process may alter the material behavior, and a subsequent modification is necessary. To avoid modeling the physics of the manufacturing process, we seek to identify the material models of the individual phases of the composite based on experiments on the composite. Therefore, we use DMNs to replace full-field simulations, and to carry out an inverse parameter optimization of the fully coupled plasticity and creep matrix model in a SFRT.

Furthermore, we extend the DMN framework to another important class of long-term behavior of SFRTs: stiffness degradation under fatigue loading using a linear fatigue-damage law for the matrix. Then, we are interested in using the DMN framework as a one-stop solution for the multi-scale simulation of SFRTs under highly non-linear long-term load cases like creep and fatigue. To this effect we extend the DMN framework using a posteriori fiber orientation tensor interpolation approach. Finally, we leverage the quasi-model-free nature of the DMN, i.e., it models the microstructure independent of the material models attached to the constituents of the microstructure to introduce a new power-law fatigue damage model for the matrix in the micro-scale. We demonstrate that the DMN framework enables us to effectively extend material models and inversely identify model parameters based on composite experiments for all possible orientation states and a variety of material models. As a result, DMNs provide us with a comprehensive all-inclusive solution for multiscale evaluation of SFRTs under long-term loading.

Acknowledgements

This thesis culminates the time spent at Corporate Research of Robert Bosch GmbH and the Institute of Engineering Mechanics (ITM) of the Karlsruhe Institute of Technology (KIT) between 2020 and 2023.

I would like to express my sincere gratitude to Matti Schneider, who shared his extensive knowledge and convincingly guided me for the completion of this thesis. Without his in-depth feedback and ability to push me in the right direction, during countless discussions, the goals of this thesis would not have been realized. I also wish to thank Fabian Welschinger for his guidance and many interesting discussions. His in-depth knowledge of the subject and ability to provide the correct tools necessary for the work have significantly sped up and improved the quality of this thesis. I am grateful to Thomas Böhlke for giving me the opportunity to work on my thesis at the Institute of Engineering Mechanics (ITM) and for his insights in material modeling. Last but not least, I would like to thank Oliver Weeger, who has a strong background in AI methods, for agreeing to act as an external reviewer.

Furthermore, I am incredibly grateful to my colleagues and fellow doctoral candidates at Robert Bosch GmbH who were always very forthcoming to my questions and helped me with many problems I encountered during the course of this work. I really enjoyed the lively coffee breaks and also the activities outside of work. I would also like to thank the colleagues at ITM for the enjoyable online coffee breaks and always making me feel at home when I was physically there at Karlsruhe.

I am extremely grateful to my parents and grandparents for their constant love, support and sacrifices which have enabled me to progress in life. A special mention goes out to my friends, especially my friends from Germany, for their interest shown in my work and for supporting me during my challenging times.

I would like to thank my girlfriend Hema from the bottom of my heart for her love, patience, and support. I knew I could always rely on you to have my back.

Publications and citation

This thesis adheres to the guidelines outlined in §12 (3) of the KIT doctoral regulations for mechanical engineering, incorporating scientific publications within a broader framework. A general introduction (Chapter 1) along with an additional introductory method section outlining the fundamental concepts (Chapter 2), followed by a concluding chapter 6 serves to put the publications in context.
If (and only if) material from the publications has been used, it is indicated by a footnote in the relevant chapter or section heading. We define and apply the clause *based on* as follows in order to define how the publication content is used.

- Selected material from the publications that are cited may be included in chapters or sections that are *based on* one or more publications, but they are not limited to it. The footnotes contain the sections that the publication's content was taken from.
- The thesis introduces references to other chapters and homogenizes the notation, spelling, and citation style of the contents of the publications, throughout.
- Repetitive content was appropriately replaced with references to other sections of this thesis.
- The numbering of equations, figures, and tables was adapted.

Furthermore, the *adapted from* clause is provided in the captions of the figures and tables that were taken from the publications. It is possible that the formatting of tables and figures that were taken from publications was altered and standardized. The captions include the relevant figure or table number and the corresponding reference publication.

List of Publications

The contents of the following publications are included in this publication-based thesis:

- A. P. Dey, F. Welschinger, M. Schneider, S. Gajek, and T. Böhlke, "Training deep material networks to reproduce creep loading of short fiber-reinforced thermoplastics with an inelastically-informed strategy," *Archive of Applied Mechanics*, vol. 92, p. 2733–2755, 2022.

- A. P. Dey, F. Welschinger, M. Schneider, S. Gajek, and T. Böhlke, "Rapid inverse calibration of a multiscale model for the viscoplastic and creep behavior of short fiber-reinforced thermoplastics based on Deep Material Networks," *International Journal of Plasticity*, vol. 160, p. 103484, 2023.

- A. P. Dey, F. Welschinger, M. Schneider, J. Köbler and T. Böhlke, "On the effectiveness of Deep Material Networks for the multi-scale virtual characterization of short fiber-reinforced thermoplastics under highly non-linear load cases," *Archive of Applied Mechanics*, vol. 94, p. 1177-1202, 2024.

Contents

1 Introduction **1**

1.1 Motivation 1

1.2 Key questions of the present work 2

1.3 State of the art 4

1.3.1 Multi-scale approaches 4

1.3.2 Modeling of creep 7

1.3.3 Modeling of fatigue 7

1.4 Outline and originality of this thesis 8

1.5 Notation 10

2 Fundamental concepts **11**

2.1 Continuum mechanics 11

2.1.1 Kinematics 11

2.1.2 Balance equations 13

2.1.3 Generalized standard materials 15

2.2 Homogenization 16

3 Training deep material networks to reproduce creep loading of short fiber-reinforced thermoplastics with an inelastically-informed strategy **19**

3.1 Introduction 19

3.2 Deep material networks 20

3.2.1 Basic concepts 20

3.2.2 Direct deep material networks 22

3.2.3 An inelastically-informed training strategy 27

3.3 Computational investigations 28

3.3.1 Setup 28

3.3.2 Performance of classical sampling 31

3.3.3 Accurate creep predictions with early stopping and a surrogate material model . . . 36
3.4 Conclusion . . . 46

4 Rapid inverse calibration of a multiscale model for the viscoplastic and creep behavior of short fiber-reinforced thermoplastics based on Deep Material Networks 48
4.1 Introduction . . . 48
4.2 Background for application to plasticity and creep of SFRTs . . . 51
4.2.1 Microstructural investigations . . . 51
4.2.2 Experimental investigations . . . 53
4.2.3 Coupled plasticity and creep law . . . 57
4.2.4 Forward calibration of the constitutive law . . . 60
4.3 Towards reducing the experimental effort . . . 64
4.3.1 On the influence of the microstructure . . . 64
4.3.2 Training of the DMN model . . . 70
4.3.3 Inverse calibration of the constitutive law . . . 75
4.3.4 On the influence of loading directions . . . 80
4.3.5 Comparison between forward and inverse calibration of constitutive model . . . 82
4.4 Conclusion . . . 85

5 On the effectiveness of Deep Material Networks for the multi-scale virtual characterization of short fiber-reinforced thermoplastics under highly nonlinear load cases 89
5.1 Introduction . . . 89
5.2 Generalized DMN-based database for variable fiber orientation . . . 91
5.2.1 Fatigue-damage model for matrix . . . 91
5.2.2 Deep Material Networks . . . 92
5.2.3 Fiber orientation interpolation . . . 96
5.3 Identification of a DMN-based database for variable fiber orientations . . . 100
5.3.1 Microstructural investigations . . . 100
5.3.2 On the runtime of linear elastic full-field simulations . . . 101
5.3.3 Training the DMN database . . . 103
5.3.4 Validation of DMN database . . . 107

5.3.5 Computation time 113
5.4 Extension of fatigue-damage model 114
5.4.1 Experimental investigations 114
5.4.2 Power-law fatigue-damage model 116
5.4.3 Inverse calibration of power-law fatigue-damage model 118
5.5 Conclusion 121

6 Conclusion **124**

Bibliography **127**

1 Introduction

1.1 Motivation

Polymers are increasingly being used in industrial applications. This increase has been fueled by contemporary demands for weight reduction and environmentally beneficial products (for example, natural fiber composites). Due to their light weight and durability, they are especially important in the automotive and aerospace industries. In most situations, polymers are further reinforced with fibers to improve their mechanical properties. Fiber features such as fiber length, fiber volume fraction, and fiber orientation have a considerable influence on the mechanical properties of polymers.

Polymer components are primarily produced by injection and compression molding procedures. Injection molding is one of the most important processes for producing polymers. This procedure is repeatable and can be used to manufacture pieces of varying sizes, characteristics, and quantities [1]. Injection molding with long fibers causes more fiber breakage than injection molding with short fibers, reducing the overall strength of the products [2]. Short fiber reinforced thermoplastics, therefore, are an appealing choice for industrial use because of their improved processability. Fiber length to diameter ratios in SFRTs are typically in the order of 10, and fibers are swirled into the molten matrix before injection. The thermoplastic matrix is commonly used, which makes it easier to recycle than thermoset-based composite materials. Carbon and glass are commonly used fiber materials, and polypropylene (PP), polyamide (PA), and polybutylene terephthalate (PBT) are common matrix materials.

The ease of manufacturing components made with SFRTs is offset by the difficulty in their characterization, particularly under long-term load cases such as creep and fatigue. Therefore, during the past few decades, there has been a lot of research on the experimental characterization and numerical prediction of their mechanical behavior. The geometry

of the reinforcements, such as aspect ratio and orientation [3, 4], has an impact on the polymer material's complex overall response. This is also affected by external factors such as temperature [5] and humidity [6]. In general, the composite material exhibits distinct anisotropic behavior at every material point of the macro-scale component because the local fiber orientations rely on the injection-molding process. An example of the complex fiber geometry obtained using μCT scan for a sample microstructure is depicted in Fig. 1.1. A traditional characterization workflow for SFRTs requires the injection molding of test plates, milling of samples with various orientations with respect to the main flow direction, and finally physical testing. Our goal is to reduce this experimental burden and propose an accurate simulative characterization of elasto-plasticity, creep and fatigue of SFRTs using a minimal number of experiments.

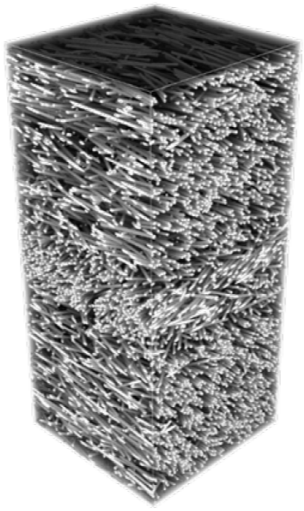

Figure 1.1: μCT scan of sample microstructure of material used in Hessman et al. [7].

1.2 Key questions of the present work

The main goal of this work is the complete virtual characterization of the SFRT composite under the highly non-linear long-term load cases like creep and fatigue. To this effect, an efficient multi-scale procedure using the concept of homogenization by resolving the problem into two scales, i.e., micro and macro [8, 9] is opted for. The two essential ingredients of the micro-scale problem are the constitutive models for each phase of the

composite (in our case, the polymer matrix and glass fibers) and the geometric representation of the microstructure. As the microstructure varies throughout the component, i.e., due to changing volume fraction or fiber orientation, the micro-scale problem to be solved changes at different points of the composite part.
This work uses the direct DMN framework developed during the Ph.D. thesis of Sebastian Gajek [10] for the solution of the micromechanical problem. The result of his work established a data-driven workflow for the fast and accurate surrogate model for the multi-scale simulation under inelastic thermomechanical loadings. We build upon this framework in the context of SFRTs and seek to answer the following questions:

1. How can the direct DMN framework be extended for reproducing the material response under the harsh conditions of long-term load cases like creep/fatigue?

2. Which models for matrix are able to accurately predict creep/fatigue?

3. How can we calibrate the creep/fatigue model using the DMN framework with minimal experimental effort?

4. How can we use the DMN framework as a complete all-inclusive solution for the virtual characterization of the composite with a spatially varying microstructure using different material models and further fine-tune them?

The development of a plasticity-creep coupled model, a power-law fatigue model and the subsequent integration with an inelastically-informed DMN database, in this thesis, addresses the above questions. The current state of the art is discussed in the following section. The outline in Section 1.4 provides an overview of the chapters that follow. The conclusion in Section 6 provides a holistic discussion regarding the above questions and further outlook.

1.3 State of the art[1]

1.3.1 Multi-scale approaches

Traditionally, mean-field approaches or variational estimates [14–17] were used to approximate the effective properties of composites. However, such methods rely upon simplifying assumptions on the considered microstructures and material models, and may come with a significant error. Alternatively, computational homogenization approaches may be used, which compute the effective response of a material by solving the balance of linear momentum on a spatially resolved representation of the material's microstructure. In the last decades, different rather efficient computational strategies were developed for this purpose [18]. Particularly successful are strategies based on the fast Fourier transform (FFT) [19, 20], which operate on a regular grid and exploit the quality of modern FFT implementations. We refer to the recent review articles [21–23] for a discussion of the latest developments.

Computational homogenization methods may be used for computing the response of a material under a specific load quite efficiently. However, when a large number of such analyses are required, for instance when the effective model is used as a material model on component scale [24–26], this approach faces limitations. Based on the realization that, in a multiscale context, the problems to be solved actually form variations of each other, strategies were sought which are able to re-use simulation data to derive a simplified effective model whose evaluation is significantly less costly. The transformation field analysis (TFA) of Dvorak and co-workers [27–29] clusters the internal variables into regions of spatial homogeneity. In this way, mean-field type models are created which are informed by the actual location of the individual phases of the material. Unfortunately, restricting to piece-wise homogeneous internal variables limits the predictive capabilities of such models. As a remedy, Michel and Suquet [30–32] generalized the method to

[1] This section is *adapted* in parts *from* the introductions of the publications "Training deep material networks to reproduce creep loading of short fiber-reinforced thermoplastics with an inelastically-informed strategy" (Dey et al., 2022 [11]), "Rapid inverse calibration of a multiscale model for the viscoplastic and creep behavior of short fiber-reinforced thermoplastics based on Deep Material Networks" (Dey et al., 2023 [12]) and "On the effectiveness of Deep Material Networks for the multi-scale virtual characterization of short fiber-reinforced thermoplastics under highly non-linear load cases" (Dey et al., 2024 [13]).

permit superpositions of spatially heterogeneous fields of internal variables. To identify these fields, techniques from model-order reduction were used [33–35]. Unfortunately, due to the nonlinear dependence of the stress on the internal variables, the difficulty was shifted to finding expressive closed-form expressions of the effective material [36–38]. Further data-driven approaches were exploited, for instance based on clustering [39–41] or proper orthogonal decomposition [42, 43]. The combination of FFT approaches [44–47] and model order reduction (MOR) frameworks [33, 40, 48] yields promising results. However, the MOR-based approach is restricted to the models in the micro-scale that it is trained on. Moreover, the selection of a proper quadrature is critical for the MOR framework since it has a significant influence on the computational performance [49].

Data-driven approaches present a viable alternative for approximating the effective characteristics directly instead of solving the micromechanical problems on unit cells. Artificial neural networks (ANNs) are particularly well-suited for such approaches since they may operate on a multi-dimensional region of interest, although the training of the ANNs requires a large data set. Several studies investigated using artificial neural networks to approximate the effective elastic energy [50–52] of a nonlinear elastic media or the relationship between stress and strain of inelastic problems [53–55]. ANNs have been used to model inelastic material laws such as plasticity [56–58], damage [59] and creep [60]. However, the prediction quality of such data-driven approaches appears to be low outside of the training domain, and accounting for the intrinsic physics, such as monotonicity and thermodynamic consistency, may be problematic. Nevertheless, physics-informed neural networks (PINNs) were proposed as a remedy [61]. For PINNs, an artificial neural network approximates the solution field of a PDE, typically by enforcing the PDE to be satisfied at specific collocation points via penalization. Applied to micromechanics, PINNs run into problems as the solution fields are typically (weakly) discontinuous, which, together with the sheer complexity of microstructured materials used in industry, limit the efficiency of such networks. Several alternative strategies involving varying neural network topologies like recurrent neural networks (RNNs) and convolutional neural networks (CNNs) emerged for modeling the multi-scale inelastic behavior. Wu et al. [62] used an RNN-based surrogate model in an FE^2 setting for modeling the elasto-plastic response in heterogeneous materials. A similar approach was adopted by Ghavamian et al. [63], where an RNN models the history-dependent micro level response. Tandale et al. [64] used both CNNs and RNNs for modeling history dependent behavior to speed-up non-linear structural deformation. Linden et al. [65] introduced a neural network based

constitutive law for hyperelasticity and further advanced discretization techniques were developed in Franke et al. [66]. These physics-augmented neural networks were also extended to model electro-mechanically coupled material behavior [67, 68].

Liu et al. [69, 70] proposed a framework for a surrogate model of micromechanical computations known as deep material networks. Instead of attempting to learn a material's mechanical response, DMNs attempt to learn the material's microstructure, i.e., they seek a simplified effective model of the geometrical interactions unique to the microstructure. Once a simplified surrogate model of the microstructure is obtained, various inelastic material laws can be inserted into the surrogate microstructure model to find the effective material response. The decoupling of the material law from the microstructural arrangement enables the DMNs to effectively model the spatially varying microstructure for a variety of different constitutive laws. Gajek et al. [71, 72], in later works, proposed direct DMNs which have lesser fitting parameters compared to the original DMNs of Liu and coworkers. The inheritance of the thermodynamic consistency of the DMNs from the constitutive laws of the constituents was demonstrated by Gajek et al. [71]. Nguyen et al. [73] proposed an interaction-based deep material network for modeling porous microstructures using a non-linear training strategy. Dey et al. [11] used the DMNs to model long-term creep deformation using an early-stopping approach and further used it for the inverse characterization of a coupled plasticity-creep model [12]. DMNs were also employed to estimate the uncertainties in the sheet molding compound manufacturing process [74] and for fully coupled thermomechanical two-scale simulations [75]. Liu et al. [76] used a transfer learning approach to model microstructures having varying fiber orientation tensors (FOTs). The versatility of the DMNs was leveraged by Gajek et al. [72] in a FE-DMN framework for simulation of an injection molded component having a spatially varying microstructure under elasto-plastic loading by using a priori interpolation, i.e., the parameters of the identified DMN are a function of the fiber orientation state in the online phase. However, such approaches seem limited for the harsh conditions of long-term loading scenarios such as creep and fatigue since the proposed theory [71] suggests that engineering accuracy may be lost if the constitutive laws are highly nonlinear, as shown in Dey et al [11]. Therefore, the a priori fiber orientation tensor interpolation for quasi-static loading [72] using DMNs is extended using a posteriori approach for long-term load cases in Dey et al. [13].

1.3.2 Modeling of creep

Creep refers to an inelastic deformation of a material which emerges upon long-term steady loading on time scales much larger than typical for visco-plastic processes. The time-dependent creep deformation was analyzed in Andrade [77], wherein three different regions were identified: primary, secondary, and tertiary. The creep strain rate starts with a high value at the beginning of the primary creep stage and reaches an approximately constant value during the secondary creep stage. The tertiary state is characterized by an increase in creep strain rate, leading to fracture of the specimen, eventually [78]. Further investigation of the effect of microstructure of steel on creep response can be found in the book of Norton [79]. Odqvist [80] and Bailey [81], in their works, introduced the triaxial state of creep. In a further step, Rabotnov et al. [82] used damage induced creep in technical applications. Although a lot of research on creep was focused on metals, Chaboche [83] showed that creep in polymers can be treated similar to metals. However, modelling of creep for polymers is not straightforward since polymers can respond in different ways such as linear elastic, linear viscoelastic, and non-linear viscoelastic, depending on the stress and temperature they are exposed to [84]. For an overview of various modelling approaches for creep we refer to the book of Naumenko and Altenbach [78].

1.3.3 Modeling of fatigue

We are interested in characterizing the stiffness degradation before failure under high-cycle fatigue for SFRTs. The fatigue behavior of thermoplastic materials differs from that of metallic materials, which is widely researched. In contrast to metals, thermoplastic materials exhibit a significant stiffness loss prior to failure under fatigue loading [85, 86]. This stiffness drop is further influenced by fiber orientation and stress amplitude. Fatigue modeling techniques for polymer composites include phenomenological macro-scale damage models which calibrate damage growth on the basis of macroscopic observable features, requiring time and cost intensive experimental studies [87–89]. Another method, using physics-based progressive damage models, specifically takes into account microstructural fatigue effects such as matrix degradation, fiber fracture, and matrix-fiber debonding.

The macroscopic composite response is a product of homogenization [90] provided localizing effects such as fracture due to damage are accounted for. A multi-scale non-local fatigue-damage model was introduced by Köbler et al. [9] for short-fiber reinforced thermoplastics based on a modified classical phase-field fracture ansatz [91]. The computation at the micro-scale is performed using fiber orientation interpolation and a full-field/MOR based strategy [92]. Recently, Magino et al. [93] introduced a fatigue-damage model based on the compliance tensor [94] in order to exploit the stability of the second phase in the fatigue-damage evolution. In fact, the intrinsic convexity of these class of models aims to reduce the computational cost related with gradient extension based damage models [95]. Although the chosen fatigue-damage model leads to an efficient model-order reduction, the MOR strategy put forward in Magino et al. [93] is limited to this particular class of material models. Further works have also used similar models for upscaling fatigue-damage models [96] and accounting for the viscous effects [97] under fatigue loading of SFRTs.

1.4 Outline and originality of this thesis

This thesis presents studies conducted by the author while he was a doctoral candidate, which have been published in scientific journals. The purpose of this thesis is to put the findings into context. We use the direct DMN framework [10] as a time and cost-efficient surrogate of the micromechanical problem and aim to address the questions put forth in Section 1.2. However, we limit ourselves to small strain setting and a non-porous defect-free industrially relevant fiber-reinforced composite.
The rest of this thesis is structured as follows:

- In **Chapter 2**, we discuss small-strain continuum mechanics and its fundamental building blocks, i.e., kinematic relations, universal balance laws and constitutive relations. Additionally, we provide an overview on the basics of homogenization.
- **Chapter 3** introduces the deep material networks which, in principle, act as a high-level surrogate for a finite element discretization of an N-phase microstructure. We extend the DMN framework to long-term creep loading. Furthermore, we show that in the case of multiple scales, in space (due to the reinforcements) and in time (due to the long-term loading) the classical DMN training may or may not lead to good

creep predictions. We resolve this issue by delivering an inelastic input during the offline elastic training of the DMN using an early-stopping strategy, a classic in machine learning.

- In **Chapter 4**, we introduce a novel fully coupled plasticity-creep law for modeling plasticity and creep of the matrix at different time scales. However, the characterization of the SFRT under plasticity and creep loadings involves the calibration of the constitutive law based on experimental results. Individual experiments need to be performed for both the constituents (pure matrix and fibers in our case) and the composite. To characterize the anisotropy of the mechanical response, experiments with samples cut from test plates with various orientations to the main flow direction need to be carried out as well. We circumvent this time and cost intensive endeavor using an *inverse* calibration workflow with the help of trained DMNs. The trained DMN, in the online phase, predicts the material response for inelastic laws like elasto-plasticity and creep accurately, thus decoupling the geometric model from the constitutive response. Furthermore, we use the DMN framework for solving the inverse problem, wherein we identified the parameters for the constitutive model (in our case, a fully coupled plasticity-creep law) of the polymer matrix by experiments performed on the composite. Finally, we show that such an approach is able to accurately identify the material parameters from the composite experiments and to represent the anisotropic response of the composite with sufficient fidelity.

- **Chapter 5** extends the DMN framework for modeling the stiffness degradation of SFRTs under high-cycle fatigue loading using an elegant fatigue-damage law introduced in Magino et al. [93]. Furthermore, we are interested in using the DMN framework as a one-stop solution for the multi-scale simulation of SFRTs under highly non-linear long-term load cases like creep and fatigue. To this effect, we introduce a posteriori fiber orientation tensor approach coupled with the DMNs. The interpolation over fiber orientations makes the simulation framework suitable not only for the calibration of various material models for different classes of SFRTs but also for component simulation with a spatially varying fiber orientation. Finally, we introduce a new power-law fatigue damage model for the matrix in the micro-scale, leveraging the quasi-model-free nature of the DMN, i.e., it models the microstructure independent of the material models attached to the constituents of the microstructure. We demonstrate that the DMN framework enables us to ef-

fectively extend material models and inversely identify model parameters based on composite experiments for all possible orientation states and a variety of material models. Thus, DMNs provide us a complete all-inclusive solution for the multiscale characterization of SFRTs.

- Finally, in **Chapter 6**, we provide a brief summary of this thesis along with concluding remarks.

1.5 Notation

In this thesis, we represent scalars with non-bold letters, vectors with bold letters, second-order tensors with italicised bold letters letters and fourth-order tensor with double-stroke symbols, e.g., the fourth-order stiffness tensor $\mathbb{C}$.
We use tensor notation and denote the contraction operation by ., which is a mathematical operation that involves summing over the product of corresponding components of two tensors to produce a new tensor. The double contraction, denoted by :, involves summing over the product of corresponding components of two tensors to produce a scalar quantity. We define a list of commonly used operators in Table 1.1.

det	Determinant
div	Divergence
`dev`	Deviatoric
`exp`	Exponential
sup	Supremum
inf	Infimum
$\langle . \rangle_+$	Macaulay brackets
tr	Trace
$\langle . \rangle_Y$	mean value over volume Y
abs	Absolute value
∇	Gradient

Table 1.1: Operators.

2 Fundamental concepts

2.1 Continuum mechanics

The section seeks to present a summary of the essential concepts of continuum mechanics useful for subsequent discussion and is by no means complete or novel. The same can be said of Chapter 2 and for extensive information we refer to the textbooks [98, 99].

2.1.1 Kinematics

The motion of a material body $\mathcal{B}$ is conveniently described with the help of a reference configuration of the body $\mathcal{B}_0$. The initial configuration is described using reference or material coordinates, see Fig. 2.1. Such a description of the body using the reference coordinates $\mathbf{X}$ is called Lagrangian description.
The path of a particle $\mathbf{X}$ under motion is defined using the function χ as

$$\mathbf{x} = \chi(\mathbf{X}, t). \tag{2.1.1}$$

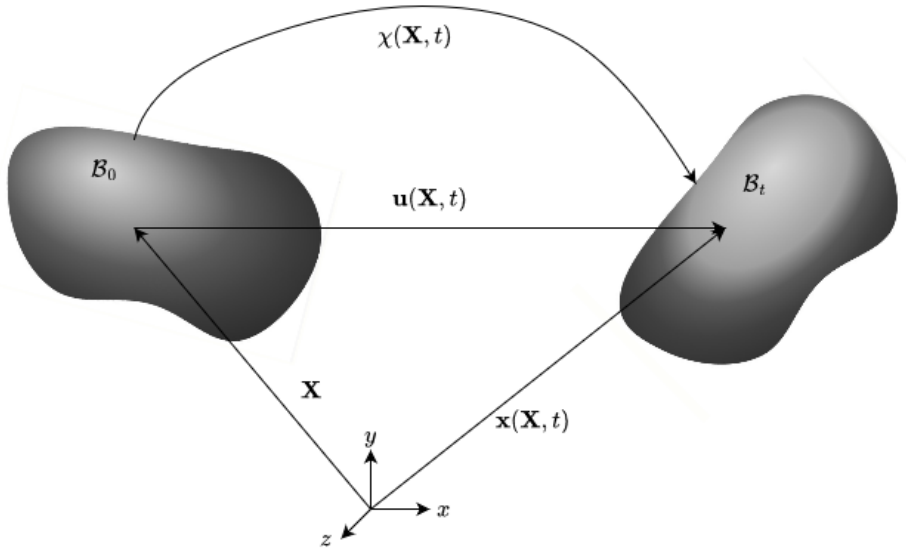

Figure 2.1: Motion of the material body $\mathcal{B}$.

The description of a quantity in terms of coordinates in the current configuration $\mathbf{x}$ is known as Eulerian description. The displacement vector $\mathbf{u}$ is the difference between current and reference positions given as

$$\mathbf{u} = \mathbf{x} - \mathbf{X}. \tag{2.1.2}$$

The deformation gradient $\boldsymbol{F}$ is defined based on the reference and current configurations as

$$\boldsymbol{F}(\mathbf{X},t) = \frac{\partial \chi}{\partial \mathbf{X}}(\mathbf{X},t). \tag{2.1.3}$$

The displacement gradient $\boldsymbol{H}$ is defined in terms of the second-order identity tensor as

$$\boldsymbol{H} = \frac{\partial \mathbf{u}}{\partial \mathbf{X}} = \boldsymbol{F} - \boldsymbol{I}. \tag{2.1.4}$$

The infinitesimal material line element $\mathrm{d}\mathbf{X}$, area element $\mathrm{d}\mathbf{A} = \mathrm{d}A \cdot \mathbf{N}$ and volume element $\mathrm{d}V = \mathrm{d}\mathbf{A}^T \cdot \mathrm{d}$, in the reference configuration, are expressed in the current configuration using the deformation gradient

$$\begin{aligned} \mathrm{d}\mathbf{x} &= \boldsymbol{F} \cdot \mathrm{d}\mathbf{X}, \\ \mathrm{d}\mathbf{a} &= \det(\boldsymbol{F})\, \boldsymbol{F}^{-T} \cdot \mathrm{d}\mathbf{A}, \\ \mathrm{d}v &= \det(\boldsymbol{F})\, \mathrm{d}V, \end{aligned} \tag{2.1.5}$$

with the help of Nanson's relation. The Green-Lagrange strain tensor $\boldsymbol{E}_G$, a commonly used measure of strain,

$$\boldsymbol{E}_G = \frac{1}{2}\left(\boldsymbol{F}^T\boldsymbol{F} - \boldsymbol{I}\right) = \frac{1}{2}\left(\boldsymbol{H} + \boldsymbol{H}^T + \boldsymbol{H}^T\boldsymbol{H}\right), \tag{2.1.6}$$

quantifies the change in length and angles in the infinitesimal neighborhood of a material point $\mathbf{X}$. In case of small deformations the displacement gradient can be defined as

$$\|\boldsymbol{H}\| \ll 1, \tag{2.1.7}$$

where $\|\cdot\|$ denotes the Frobenius norm. Thus, linearizing the Green-Lagrange strain tensor $\boldsymbol{E}_G$ in the reference state yields

$$\boldsymbol{E}_G \approx \frac{1}{2}\left(\boldsymbol{H} + \boldsymbol{H}^T\right) \tag{2.1.8}$$

where, due to the small-strain assumption (2.1.7), it is not necessary to distinguish between the current and reference configuration, i.e.,

$$\mathbf{x} \approx \mathbf{X}. \tag{2.1.9}$$

Therefore, the various strain measures at finite strains, all of which coincide at small strains, is defined as the linearized strain tensor

$$\boldsymbol{\varepsilon} = \frac{1}{2}\left(\boldsymbol{H} + \boldsymbol{H}^T\right). \tag{2.1.10}$$

In the current work, all further discussions are limited to small strain kinematics, where linear deformation theory can be used.

2.1.2 Balance equations

In this section, the continuum mechanics balance equations are discussed based on Liu's textbook [100, § 2]. To explain the generalized conservation equations of continuum mechanics, firstly, the *general balance equation* of a quantity ψ within any bounded regular subregion $\mathcal{V}_t \in \mathcal{B}$ of a body $\mathcal{B}$ is defined as

$$\frac{\mathrm{d}}{\mathrm{d}t}\int_{\mathcal{V}_t} \psi \,\mathrm{d}v = \int_{\partial\mathcal{V}_t} \Phi_\psi \cdot \mathbf{n} \,\mathrm{d}a + \int_{\mathcal{V}_t} s_\psi \,\mathrm{d}v, \tag{2.1.11}$$

where Φ_ψ represents the flux of ψ and s_ψ is the source term of ψ.
The local form at a regular point $\mathbf{x}$ is obtained using the divergence theorem

$$\frac{\partial \psi}{\partial t} + \operatorname{div}\left(\psi\dot{\mathbf{x}}\right) = s_\psi + \operatorname{div}\Phi_\psi. \tag{2.1.12}$$

Conservation of mass

The mass density ρ is essential for discussing the *balance equation of mass*, i.e., $\psi \equiv \rho$. The mass source term s_ρ is set to zero based on classical mechanics. Moreover, there exists no mass flux $\Phi_\rho = 0$ in most solid materials. Therefore, the balance equation, in integral form, reads

$$\frac{\mathrm{d}}{\mathrm{d}t}\int_{\mathcal{V}_t} \rho \,\mathrm{d}v = 0, \tag{2.1.13}$$

and in local form

$$\frac{\partial \rho}{\partial t} + \mathrm{div}\,(\rho\dot{\mathbf{x}}) = 0. \tag{2.1.14}$$

Balance of linear momentum

The discussion of the *balance equation of linear momentum* is based on the linear momentum density $\rho\dot{\mathbf{x}}$, i.e., $\psi \equiv \rho\dot{\mathbf{x}}$. The dependence of the source term on the external body force density $\mathbf{b}$ acting on point $\mathbf{x}$, e.g., a gravitational force, $s_\psi = \rho\mathbf{b}$ is based on the Euler's law of motion. The flux of linear momentum is defined using the Cauchy stress tensor $\boldsymbol{\sigma}$ which associates the stress vector $\mathbf{t}$ to the normal vector $\mathbf{n}$ with the help of Cauchy's stress theorem

$$\mathbf{t} = \boldsymbol{\sigma}\cdot\mathbf{n}. \tag{2.1.15}$$

The symmetricity of the stress tensor is discussed in the following section. Therefore, the balance of linear momentum is defined as

$$\frac{\mathrm{d}}{\mathrm{d}t}\int_{\mathcal{V}_t} \rho\dot{\mathbf{x}} \,\mathrm{d}v = \int_{\mathcal{V}_t} \rho\mathbf{b} \,\mathrm{d}v + \int_{\partial\mathcal{V}_t} \boldsymbol{\sigma}\cdot\mathbf{n} \,\mathrm{d}a \quad \text{and} \quad \rho\ddot{\mathbf{x}} = \rho\mathbf{b} + \mathrm{div}\boldsymbol{\sigma}, \tag{2.1.16}$$

in integral and local forms, respectively.

Balance of angular momentum

The *balance equation of angular momentum* requires the definition of the angular momentum density $\rho(\mathbf{x}-\mathbf{x}_0)\times\dot{\mathbf{x}}$ w.r.t. a reference point $\mathbf{x}_0$, i.e., $\psi \equiv \rho(\mathbf{x}-\mathbf{x}_0)\times\dot{\mathbf{x}}$, where $\times$ denotes the vector product.

The dependence of the source term on the external body force density $\mathbf{b}$, i.e, $s_\psi = \rho(\mathbf{x}-\mathbf{x}_0)\times\mathbf{b}$ is based on the Euler's law of motion. The flux of angular momentum

incorporates the Cauchy stress tensor $\boldsymbol{\sigma}$, resulting in the balance equation of angular momentum in its integral form,

$$\frac{\mathrm{d}}{\mathrm{d}t}\int_{\mathcal{V}_t}\rho(\mathbf{x}-\mathbf{x}_0)\times\dot{\mathbf{x}}\,\mathrm{d}v=\int_{\mathcal{V}_t}\rho(\mathbf{x}-\mathbf{x}_0)\times\mathbf{b}\,\mathrm{d}v+\int_{\partial\mathcal{V}_t}(\mathbf{x}-\mathbf{x}_0)\times(\boldsymbol{\sigma}\cdot\mathbf{n})\,\mathrm{d}a. \tag{2.1.17}$$

Given that the balance of linear momentum holds, then the local form of the balance of angular momentum is equivalent to the symmetry of Cauchy's stress tensor

$$\boldsymbol{\sigma}=\boldsymbol{\sigma}^T. \tag{2.1.18}$$

Conservation of energy

The *balance equation of energy* requires the total energy, i.e, the sum of the internal energy ρe and the kinetic energy $\rho\dot{\mathbf{x}}\cdot\dot{\mathbf{x}}/2$ to be specified. Here, we set $\psi\equiv\rho e+\rho\dot{\mathbf{x}}\cdot\dot{\mathbf{x}}/2$. The flux of the total energy includes a mechanical part $\boldsymbol{\sigma}\cdot\dot{\mathbf{x}}$ and a heat flux $\mathbf{q}$, i.e., $\Phi_\psi=\boldsymbol{\sigma}\cdot\dot{\mathbf{x}}-\mathbf{q}$. The source term s_ψ in the balance energy is defined using the power of the external body forces $\rho\dot{\mathbf{x}}\cdot\mathbf{b}$ and the heat source r. Therefore, the conservation of energy, in the integral form, reads

$$\frac{\mathrm{d}}{\mathrm{d}t}\int_{\mathcal{V}_t}\left(\rho e+\frac{\rho}{2}\dot{\mathbf{x}}\cdot\dot{\mathbf{x}}\right)\,\mathrm{d}v=\int_{\mathcal{V}_t}(\rho\dot{\mathbf{x}}\cdot\mathbf{b}+\rho r)\,\mathrm{d}v+\int_{\partial\mathcal{V}_t}(\dot{\mathbf{x}}\cdot\boldsymbol{\sigma}\cdot\mathbf{n}-\mathbf{q}\cdot\mathbf{n})\,\mathrm{d}a \tag{2.1.19}$$

or, using the balance of linear momentum, in the local form

$$\rho\dot{e}+\operatorname{div}\mathbf{q}=\boldsymbol{\sigma}:\nabla\dot{\mathbf{x}}+\rho r. \tag{2.1.20}$$

2.1.3 Generalized standard materials

The kinematic and balance equations introduced in Sections 2.1.1 and 2.1.2, respectively, are not enough to uniquely solve the system. The missing piece is the material equations or constitutive laws, which are material dependent as opposed to the balance equations and kinematics.

The consistent definition of new material laws comes with certain constraints, which include thermodynamic consistency. Nguyen et al. [101] introduced a useful class of material models known as *Generalized Standard Materials* (GSM) defined by the scalar and non-negative Helmholtz free energy potential

$$\psi:\operatorname{sym}(3)\times\mathbb{R}^M\to\mathbb{R},\quad(\boldsymbol{\varepsilon},\mathbf{q})\mapsto\psi(\boldsymbol{\varepsilon},\mathbf{q}), \tag{2.1.21}$$

along with a convex dissipation potential

$$\phi : \mathbb{R}^M \to \mathbb{R}, \quad \dot{\mathbf{q}} \mapsto \phi(\dot{\mathbf{q}}), \tag{2.1.22}$$

where $\mathbf{q}$ defines the vector of internal variables, both of which are differentiable w.r.t. their arguments. Therefore, the stress $\boldsymbol{\sigma}$ and the generalized driving forces $\boldsymbol{B}_{\mathbf{q}}$ of the internal variables $\mathbf{q}$ are defined as

$$\boldsymbol{\sigma} = \frac{\partial \psi}{\partial \boldsymbol{\varepsilon}} \quad \text{and} \quad \boldsymbol{B}_{\mathbf{q}} = -\frac{\partial \psi}{\partial \mathbf{q}}. \tag{2.1.23}$$

In case of the potential, the conditions

$$\psi(\mathbf{0}, \mathbf{0}) = 0, \quad \phi(\mathbf{0}) = 0 \quad \text{and} \quad \frac{\partial \phi}{\partial \dot{\mathbf{q}}}(0) = 0 \tag{2.1.24}$$

hold. The complimentary law governs the evolution of the internal variables

$$\boldsymbol{B}_{\mathbf{q}} = \frac{\partial \phi}{\partial \dot{\mathbf{q}}}, \tag{2.1.25}$$

and yields the Biot equation, which can be re-formulated as

$$\frac{\partial \psi}{\partial \mathbf{q}} + \frac{\partial \phi}{\partial \dot{\mathbf{q}}} = 0. \tag{2.1.26}$$

The Clausius-Duhem inequality gives the second law of thermodynamics, in the isothermal case,

$$\mathcal{D} = \boldsymbol{\sigma} : \dot{\boldsymbol{\varepsilon}} - \dot{\psi} \geq 0, \tag{2.1.27}$$

where the dissipation is represented by $\mathcal{D}$. In the case of a GSM, the inequality reduces to

$$\frac{\partial \phi}{\partial \dot{\mathbf{q}}} \cdot \dot{\mathbf{q}} \geq 0, \tag{2.1.28}$$

which is retained by the design of the dissipation potential (2.1.24).

2.2 Homogenization

The material modeling of a composite involves the modeling of multiple constituents. To that end, an efficient multi-scale technique by dividing the problem into two scales, namely micro and macro is used. The constitutive model for each phase of the composite (in our case, the polymer matrix and glass fibers) and the geometric description of the microstructure are two crucial components of the micro-scale problem. The overall effective

material response of the micro-scale is determined using homogenization. The purpose of homogenization techniques is to replace a heterogeneous (and complicated) material with a homogenous one having the same material response.
Voigt [102] and Reuss [103] established the foundations of analytic homogenization methods in solid mechanics by proposing limitations for the composite stiffness using the harmonic and arithmetic average of its elements. Hashin and Shtrikman [104] refined these constraints for isotropically distributed inclusions, assuming that both the matrix and the inclusion have isotropic material properties.
An accurate representation of the microstructure, i.e., a *representative volume element* (RVE), is used to get macroscopic effective properties of the microstructure. Different definitions exist for what it means for a volume element to be considered representative [105, 106]. One such interpretation is that the stiffness tensor of an elastic composite must be nearly independent of the imposed boundary conditions [107]. Another possibility is that its effective properties are similar to those of an infinitely vast volume with macroscopic homogeneous properties. Nevertheless, the characteristic length l_{char}, for example, the length of an inclusion, must be substantially lower than the representative volume element's characteristic length l_{RVE}

$$l_{\text{char}} \ll l_{\text{RVE}} \tag{2.2.1}$$

so that the behavior of the microstructure is accurately represented. On the other hand, the characteristic length of the RVE needs to be significantly smaller than the macroscopic component length L

$$l_{\text{RVE}} \ll L \tag{2.2.2}$$

to ensure the validity of the scale separation. The various length scales are depicted in Fig. 2.2.
Considering a representative volume element Y, wherein a stress field $\boldsymbol{\sigma}$ and a strain field $\boldsymbol{\varepsilon}$ are given. Now, the macroscopic stress $\langle\boldsymbol{\sigma}\rangle_Y$ and strain $\langle\boldsymbol{\varepsilon}\rangle_Y$ are calculated as

$$\begin{aligned} \langle\boldsymbol{\sigma}\rangle_Y &= \frac{1}{|Y|}\int_Y \boldsymbol{\sigma}\,\mathrm{d}Y, \\ \langle\boldsymbol{\varepsilon}\rangle_Y &= \frac{1}{|Y|}\int_Y \boldsymbol{\varepsilon}\,\mathrm{d}Y, \end{aligned} \tag{2.2.3}$$

where

$$|Y| = \int_Y \mathrm{d}Y \tag{2.2.4}$$

defines the volume of the representative body Y. The Hill-Mandel condition [17]

$$\langle \boldsymbol{\sigma} : \dot{\boldsymbol{\varepsilon}} \rangle_Y = \langle \boldsymbol{\sigma} \rangle_Y : \langle \dot{\boldsymbol{\varepsilon}} \rangle_Y \tag{2.2.5}$$

postulates that, considering the average stress and strain rate as macroscopic variables, the virtual power on the macroscale equals the power on the microscale. The Hill-Mandel condition holds for linear displacement, uniform stress and periodic boundary conditions. In this work, we use the deep material networks, which is a binary tree of laminates, as a homogenization function for a particular microstructure. The binary tree of laminates represents a simplified model for the complex microstructure and enables the fast evaluation of the homogenization function $\mathcal{DMN}_Y$. The homogenization function finds an effective material response on the microstructure scale while reflecting the mechanical behavior of the heterogeneous phases of the microstructure Y on the smaller scale. We refer to Sections 3.2 and 5.2.2 for more details.

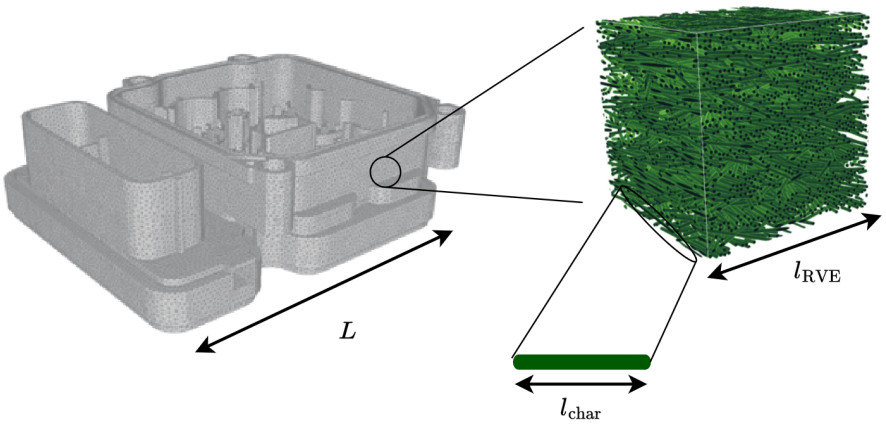

Figure 2.2: Length scales in homogenization adapted from Henkelmann [108].

3 Training deep material networks to reproduce creep loading of short fiber-reinforced thermoplastics with an inelastically-informed strategy[1]

3.1 Introduction

Classically, deep material networks are trained on linear elastic data alone. However, when considering long-term creep loading of SFRT composites on an industrial scale, the framework needs to be re-evaluated with care. Indeed, for such a scenario, multiple scales are involved both in space (due to the reinforcements) and in time (due to the long-term loading). We demonstrate by computational experiments that the identified DMNs may or may not lead to good creep predictions. We show that this is caused by overfitting the linear elastic data relative to the creep response. In particular, an early-stopping strategy, a classic in machine learning [109, § 7.8], may be used to resolve this issue.
Section 3.2 outlines the basic construction principles of DMNs, together with the classical elasticity-based training and the novel inelastically-informed training strategy. Section 3.3

[1] This chapter is *based on* Sections 2, 3 and 4 of the publication A. P. Dey, F. Welschinger, M. Schneider, S. Gajek, and T. Böhlke, "Training deep material networks to reproduce creep loading of short fiber-reinforced thermoplastics with an inelastically-informed strategy," *Archive of Applied Mechanics*, vol. 92, p. 2733–2755, 2022. The introduction has been condensed to eliminate redundancy with Chapter 1, and the notation has been standardized.

reports on the considered setup (E-glass fiber reinforced polybutylene terephthalate-PBT) and examines the various training procedures and their inelastic generalizations with care. Particularly powerful turns out to be a hybrid strategy, where the early stopping is itself based on an inelastic surrogate material model which shares the basic phenomena with the "real" material model but may be evaluated with less expense.

3.2 Deep material networks

3.2.1 Basic concepts

A Deep Material Network (DMN) [69, 71, 110] with N phases in three spatial dimensions consists of the following data.

1. A set $\mathcal{N}$ of nodes with indices $1, \dots, n$.
2. A set $\mathcal{G}$ of (formal) integration points with indices $1, \dots, m$.
3. A partition of the set of integration points $\mathcal{G}$ into N subsets $\mathcal{G}_i$ $(i = 1, \dots, N)$ which are disjoint and cover the set $\mathcal{G}$. The set $\mathcal{G}_i$ contains all integration points which are occupied by the i-th material.
4. A set of positive weights $w_1, \dots, w_m$, which sum to unity.
5. A symmetrized gradient operator $\boldsymbol{D} \in \mathbb{R}^{6m \times 3n}$.

The weights may be collected in the diagonal matrix $\boldsymbol{W} \in \mathbb{R}^{6m \times 6m}$ with

$$\boldsymbol{W}_{ii} = w_{\lfloor i/6 \rfloor} \quad \text{(floor division)}. \tag{3.2.1}$$

To express the compatibility conditions, we introduce the averaging matrix $\boldsymbol{A} \in \mathbb{R}^{6 \times 6m}$, an m-fold copy of the 6×6-identity matrix. Then, the symmetrized gradient operator $\boldsymbol{D}$ and the weights w_i should satisfy the condition

$$\boldsymbol{A}\boldsymbol{W}\boldsymbol{D} = 0, \tag{3.2.2}$$

which states that the weighted average of the compatible strains vanishes.
Suppose a nonlinear stress-strain relationship $\boldsymbol{f}_i : \mathbb{R}^6 \to \mathbb{R}^6$ at small strains is given

for each material $i = 1, \dots, N$. Then, for prescribed strain $\overline{\boldsymbol{\varepsilon}}$, which we consider as an element of $\mathbb{R}^6$, we seek a displacement field $\vec{\boldsymbol{u}} \in \mathbb{R}^{3n}$, s.t. the balance of linear momentum

$$\boldsymbol{D}^T \boldsymbol{W} \boldsymbol{f}(\boldsymbol{A}^T \overline{\boldsymbol{\varepsilon}} + \boldsymbol{D}\vec{\boldsymbol{u}}) = 0 \tag{3.2.3}$$

holds, where the function $\boldsymbol{f}$ applies the nonlinearity $\boldsymbol{f}_i$ at the i-th integration point and the vector $\boldsymbol{A}^T \overline{\boldsymbol{\varepsilon}}$ contains m identical copies of the average strain $\overline{\boldsymbol{\varepsilon}}$. The effective stress is subsequently computed via

$$\overline{\boldsymbol{\sigma}} = \boldsymbol{A}\boldsymbol{W} \boldsymbol{f}\left(\boldsymbol{A}^T \overline{\boldsymbol{\varepsilon}} + \boldsymbol{D}\vec{\boldsymbol{u}}\right). \tag{3.2.4}$$

Deep material networks serve as a high-level abstraction for a finite-element discretization of an N-phase microstructure. Indeed, for such a microstructure Y, decomposed into N subdomains Y_i, any finite element discretization gives rise to a node set $\mathcal{N}$, a set of integration points $\mathcal{G}$ with associated quadrature weights w_i. The gradient operator $\boldsymbol{D}$ arises by evaluating the FE B-matrix at the integration points, and a nodal decomposition $\mathcal{G}_i$ emerges by associating any integration point $y_j \in Y$ to the material domain which it lies in, $y_j \in \mathcal{G}_i \iff y_j \in Y_i$. Then, the classical weak form of the finite-element problem is equivalent to the equilibrium equation (3.2.3) for any type of nonlinearity $\boldsymbol{f}_i$.

Deep material networks give rise to an effective material behavior which automatically satisfies the Hill-Mandel condition, inherits thermodynamical consistency from its phases, preserves elementary micromechanical bounds and gives rise to a uniquely solvable nonlinear system of equations (3.2.3) (provided the kernel of $\boldsymbol{D}$ is factored out and the nonlinearities $\boldsymbol{f}_i$ are strictly monotone) [71, 110].

Deep material networks serve as an abstraction of finite-element discretizations of micromechanical problems. They inherit the positive characteristics, but dispense with the constraints of a physical realization of the finite-element discretization. In particular, the node sets $\mathcal{N}$ and $\mathcal{G}$ have no intrinsic physical meaning. Still, DMNs may be regarded as statistically similar representative volume elements [111, 112], which reflect - on an abstract level - the topology of the microstructure which they should serve as a surrogate model for.

To start with, DMNs typically fix the node set $\mathcal{N}$ and the integration points $\mathcal{G}$ (with the decomposition $\mathcal{G}_i$) a priori. Then, a model for the gradient and the weights

$$\boldsymbol{D} \equiv \boldsymbol{D}(\vec{\boldsymbol{p}}), \quad \boldsymbol{W} \equiv \boldsymbol{W}(\vec{\boldsymbol{p}}) \tag{3.2.5}$$

in terms of a suitable (hyper)parameter vector $\vec{\boldsymbol{p}}$ is postulated. In the literature, different possibilities to choose the parametrized matrices $\boldsymbol{D}(\vec{\boldsymbol{p}})$ and $\boldsymbol{W}(\vec{\boldsymbol{p}})$ were proposed.

Liu and coworkers [69, 70, 113, 114] considered a hierarchy of rotated laminates. Gajek et al. [71] introduced a hierarchical construction with laminates of variable direction of lamination, see Section 3.2.2. This construction has fewer parameters than rotated laminates, but was shown to provide similar accuracy. Nguyen and Noels [73] introduced polytopal DMNs which permit more general rank-one jumps than pure laminates to deal with porous microstructures. All these approaches have in common that the matrix $\boldsymbol{D}$ is sparse, reflecting a further characteristic of finite element discretizations.

In any case, once the construction plan (3.2.5) is fixed, DMNs are operated in two stages. In the first stage, the parameters $\vec{\boldsymbol{p}}$ are fitted to a suitable objective

$$J(\vec{\boldsymbol{p}}) \equiv \sum_{s=1}^{n_{\mathtt{obs}}} J_s(\vec{\boldsymbol{p}}) + \Psi(\vec{\boldsymbol{p}}) \longrightarrow \min_{\vec{\boldsymbol{p}}} \tag{3.2.6}$$

with contributions J_s that measure data fidelity to $n_{\mathtt{obs}}$ observations and, possibly, a regularization term Ψ. This so-called offline training is typically based on linear elastic precomputations obtained from full-field simulations on a high-fidelity representation of the microstructure [69, 70], giving rise to the contributions J_s. Once the parameters $\vec{\boldsymbol{p}}$ are identified, the deep material network may be used as a high-fidelity full-field surrogate model for inverse parameter identification or for concurrent multiscale simulations [72, 75, 76]. For this purpose, equation (3.2.3) is solved for nonlinearities that arise from a time discretization of inelastic constitutive laws.

As an alternative to a parameter identification based on linear elastic data alone, the nonlinear effective behavior may be taken into consideration [73]. However, such a procedure may be delicate, as modern gradient-based learning techniques are based on automatic differentiation, which may prove rather computationally expensive for sophisticated material models. The work at hand proposed an alternative strategy based on early stopping [109, § 7.8], see Section 3.2.3.

3.2.2 Direct deep material networks

As a construction strategy for the symmetrized gradient operator $\boldsymbol{D}(\vec{\boldsymbol{p}})$ and the weight matrix $\boldsymbol{W}(\vec{\boldsymbol{p}})$, we use a hierarchy of N-phase laminates where a scale separation is assumed at each level of the hierarchy. For $K-1$ such scale-separations, we obtain a perfect, ordered N-ary tree of depth K comprising

$$1 + N + N^2 + \ldots + N^{K-1} = \frac{N^K - 1}{N - 1} \tag{3.2.7}$$

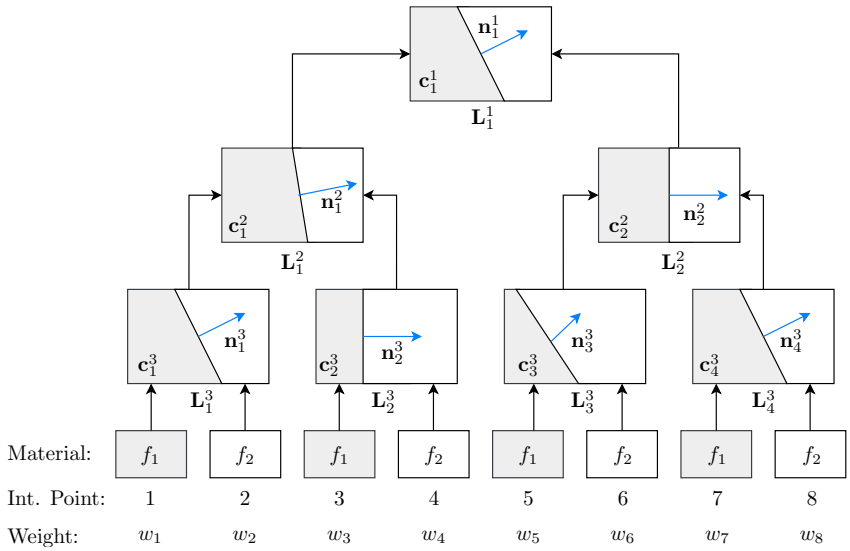

Figure 3.1: Example of a two-phase direct DMN with depth $K = 3$ adapted from Dey et al. [11, Fig. 1]

individual N-phase laminates. We call such an N-ary tree a *direct DMN* [71, 72, 75]. Fig. 3.1 shows an example of a direct DMN with $K = 3$ layers and $N = 2$ phases.

To build the DMN, we first consider a single N-phase laminate with lamination direction $\boldsymbol{n} \in \mathbb{R}^3$ and a vector $\boldsymbol{c} \in \mathbb{R}^N$ of volume fractions, which are positive and sum to one. The elastic behavior of such a laminate may be expressed in terms of $N-1$ displacement-jump vectors $\vec{\boldsymbol{a}} = [\boldsymbol{a}_1, \dots, \boldsymbol{a}_{N-1}]^T \in \mathbb{R}^{3(N-1)}$, see Ospald et al. [115]. Classically, a N-phase laminate has N displacement-jump vectors whose weighted average vanishes. In our representation, this constraint has been explicitly resolved by expressing the last displacement-jump vector in terms of the previous $N-1$ vectors.

For fixed kinematics, the N strain fluctuations, one for each phase, emerge by applying the symmetrized gradient operator $\boldsymbol{L}(\boldsymbol{c}, \boldsymbol{n}) \in \mathbb{R}^{6N \times 3(N-1)}$, given by the formula

$$\boldsymbol{L}(\boldsymbol{c},\boldsymbol{n}) = \begin{bmatrix} \left(\sum_{i=1}^{1} c_i - 1\right)\boldsymbol{B}(\boldsymbol{n}) & \left(\sum_{i=1}^{2} c_i - 1\right)\boldsymbol{B}(\boldsymbol{n}) & \dots & \left(\sum_{i=1}^{N-1} c_i - 1\right)\boldsymbol{B}(\boldsymbol{n}) \\ \sum_{i=1}^{1} c_i\boldsymbol{B}(\boldsymbol{n}) & \left(\sum_{i=1}^{2} c_i - 1\right)\boldsymbol{B}(\boldsymbol{n}) & \dots & \left(\sum_{i=1}^{N-1} c_i - 1\right)\boldsymbol{B}(\boldsymbol{n}) \\ \sum_{i=1}^{1} c_i\boldsymbol{B}(\boldsymbol{n}) & \sum_{i=1}^{2} c_i\boldsymbol{B}(\boldsymbol{n}) & \dots & \left(\sum_{i=1}^{N-1} c_i - 1\right)\boldsymbol{B}(\boldsymbol{n}) \\ \vdots & \vdots & \ddots & \vdots \\ \sum_{i=1}^{1} c_i\boldsymbol{B}(\boldsymbol{n}) & \sum_{i=1}^{2} c_i\boldsymbol{B}(\boldsymbol{n}) & \dots & \left(\sum_{i=1}^{N-1} c_i - 1\right)\boldsymbol{B}(\boldsymbol{n}) \\ \sum_{i=1}^{1} c_i\boldsymbol{B}(\boldsymbol{n}) & \sum_{i=1}^{2} c_i\boldsymbol{B}(\boldsymbol{n}) & \dots & \sum_{i=1}^{N-1} c_i\boldsymbol{B}(\boldsymbol{n}) \end{bmatrix}, \tag{3.2.8}$$

to the vector of displacement-jump vectors. Here, for any vector $\boldsymbol{a}$, the symmetrized tensor product $\boldsymbol{n} \otimes_s \boldsymbol{a}$ may be expressed by the matrix-vector product $\boldsymbol{B}(\boldsymbol{n})\boldsymbol{a}$ in Mandel's notation. Explicitly, the strain-displacement-jump matrix $\boldsymbol{B} : \mathbb{R}^3 \to \mathbb{R}^{6\times 3}$ reads

$$\boldsymbol{B}(\boldsymbol{n}) = \begin{bmatrix} n_1 & 0 & 0 \\ 0 & n_2 & 0 \\ 0 & 0 & n_3 \\ \frac{1}{\sqrt{2}} n_2 & \frac{1}{\sqrt{2}} n_1 & 0 \\ \frac{1}{\sqrt{2}} n_3 & 0 & \frac{1}{\sqrt{2}} n_1 \\ 0 & \frac{1}{\sqrt{2}} n_3 & \frac{1}{\sqrt{2}} n_2 \end{bmatrix}. \tag{3.2.9}$$

With these expressions for a single laminate at hand, let us consider an N-ary tree of such N-phase laminates. To each laminate, a unit direction of lamination $\boldsymbol{n}_j^k$ is associated. We collect these normals in a large vector

$$\vec{\boldsymbol{n}} = \left[\boldsymbol{n}_1^1, \boldsymbol{n}_1^2, \ldots, \boldsymbol{n}_N^2, \ldots, \boldsymbol{n}_1^K, \ldots, \boldsymbol{n}_{N^{K-1}}^K\right]^T \in \mathbb{R}^{3\frac{N^K-1}{N-1}} \tag{3.2.10}$$

with an ordering which traverses the tree from the root to the leafs through each level from left to right (like a breadth-first search of the corresponding tree). Moreover, to each laminate, N volume fractions are associated. We parametrize those in terms of a collection $\vec{\boldsymbol{w}} = [w_1, \ldots, w_{N^K}] \in \mathbb{R}^{N^K}$ of positive weights (formally) residing on level $K+1$. The volume fractions are then computed by a weighted average [71, eq. (3.8)-(3.9)].

The set of $m = N^K$ integration points $\mathcal{G}$ corresponds to the individual phases of the laminates on level K, and is partitioned into N subsets $\mathcal{G}_i$ $(i = 1, \ldots, N)$ in a alternating manner

$$\mathcal{G}_i = \left\{ m \in \mathcal{G} \,\middle|\, m = i + lN, \quad l = 0, 1, \ldots, N^{K-1} \right\}, \tag{3.2.11}$$

see Fig. 3.1 for an illustration for the special case of $N = 2$. Thus, each laminate on the lowest level receives one of the N phases as input.

The kinematics of each of the laminates is governed by $N-1$ (local) displacement jumps

$$\vec{\boldsymbol{a}}_j^k = [\boldsymbol{a}_{1+(j-1)(N-1)}^k, \ldots, \boldsymbol{a}_{j(N-1)}^k]^T \in \mathbb{R}^{3(N-1)}. \tag{3.2.12}$$

Here, the upper index $k = 1, \ldots, K$ labels the depth and the lower index $j = 1, \ldots, N^{k-1}$ corresponds the horizontal position in the N-ary tree. We collect these individual displacement jumps in a (global) displacement vector

$$\vec{\boldsymbol{u}} = \left[\boldsymbol{a}_1^1, \ldots, \boldsymbol{a}_{N-1}^1, \boldsymbol{a}_1^2, \ldots, \boldsymbol{a}_{N(N-1)}^2, \ldots, \boldsymbol{a}_1^K, \ldots, \boldsymbol{a}_{N^{K-1}(N-1)}^K\right]^T \in \mathbb{R}^{3(N^K-1)} \tag{3.2.13}$$

with the same ordering as for the lamination directions. These serves as the displacement-type degrees of freedom of the deep material network. Thus, the direct DMN comprises $n = N^K - 1$ nodes, one for each displacement jump.

The (global) symmetrized gradient operator $\boldsymbol{D} \in \mathbb{R}^{6N^K \times 3(N^K-1)}$ may be assembled from the local symmetrized gradient operators (3.2.8) in a similar fashion as finite elements [116]. More precisely, we obtain a representation

$$\boldsymbol{D} = \sum_{k=1}^{K} \sum_{j=1}^{N^{k-1}} \boldsymbol{J}_j^k \boldsymbol{L}(\boldsymbol{c}_j^k, \boldsymbol{n}_j^k) \boldsymbol{E}_j^k \tag{3.2.14}$$

in terms of suitable extraction $\boldsymbol{E}_j^k$ and prolongation matrices $\boldsymbol{J}_j^k \in \mathbb{R}^{6N^K \times 6N}$. These matrices contain only zeros and ones and establish the connection between local quantities and global quantities. Moreover, the matrices $\boldsymbol{E}_j^k$ and $\boldsymbol{J}_j^k$ depend only on the topology of the tree and are independent of the DMN parameters $\vec{\boldsymbol{p}}$. The extraction matrix $\boldsymbol{E}_j^k \in \mathbb{R}^{3(N-1)\times 3(N^K-1)}$ picks out the (local) displacement jumps $\vec{\boldsymbol{a}}_j^k$ from the global vector $\vec{\boldsymbol{u}}$, i.e., $\vec{\boldsymbol{a}}_j^k = \boldsymbol{E}_j^k \vec{\boldsymbol{u}}$ holds, and may be expressed in terms of the Kronecker product [117]

$$\boldsymbol{E}_j^k = \boldsymbol{e}_{j-1+N^{k-1}}^T \otimes \mathrm{diag}(\underbrace{\mathbf{1}, \ldots, \mathbf{1}}_{N-1 \text{ times}}) \quad \text{with} \quad \mathbf{1} \equiv \mathrm{diag}(1,1,1) \in \mathbb{R}^{3\times 3} \tag{3.2.15}$$

and the Cartesian basis vector $\boldsymbol{e}_{j-1+N^{k-1}} \in \mathbb{R}^{\frac{N^K-1}{N-1}}$. Similarly, the injection matrix $\boldsymbol{J}_j^k$ admits the Kronecker-product representation

$$\boldsymbol{J}_j^k = \boldsymbol{e}_j^T \otimes \mathrm{diag}(\underbrace{1, \ldots, 1}_{N \text{ times}}) \otimes \vec{1}^k \otimes \boldsymbol{I} \quad \text{with} \quad \boldsymbol{I} \equiv \mathrm{diag}(1,1,1,1,1,1) \in \mathbb{R}^{6\times 6}, \tag{3.2.16}$$

the Cartesian basis vector $\boldsymbol{e}_j \in \mathbb{R}^{N^{k-1}}$ and the column vector of ones $\vec{1}^k = [1, \ldots, 1] \in \mathbb{R}^{N^{K-k}}$.

To illustrate the procedure, we record these matrices for the two-phase DMN of depth $K = 3$ shown in Fig. 3.1. The extraction matrices read

$$\boldsymbol{E}_1^1 = \begin{bmatrix} \mathbf{1} & 0 & 0 & 0 & 0 & 0 & 0 \end{bmatrix}, \boldsymbol{E}_1^2 = \begin{bmatrix} 0 & \mathbf{1} & 0 & 0 & 0 & 0 & 0 \end{bmatrix}, \ldots, \boldsymbol{E}_4^3 = \begin{bmatrix} 0 & 0 & 0 & 0 & 0 & 0 & \mathbf{1} \end{bmatrix}, \tag{3.2.17}$$

whereas the prolongation operators take the form

$$\boldsymbol{J}_1^1 = \begin{bmatrix} \boldsymbol{I} & 0 \\ \boldsymbol{I} & 0 \\ \boldsymbol{I} & 0 \\ \boldsymbol{I} & 0 \\ 0 & \boldsymbol{I} \\ 0 & \boldsymbol{I} \\ 0 & \boldsymbol{I} \\ 0 & \boldsymbol{I} \end{bmatrix}, \quad \boldsymbol{J}_1^2 = \begin{bmatrix} \boldsymbol{I} & 0 \\ \boldsymbol{I} & 0 \\ 0 & \boldsymbol{I} \\ 0 & \boldsymbol{I} \\ 0 & 0 \\ 0 & 0 \\ 0 & 0 \\ 0 & 0 \end{bmatrix}, \quad \boldsymbol{J}_2^2 = \begin{bmatrix} 0 & 0 \\ 0 & 0 \\ 0 & 0 \\ 0 & 0 \\ \boldsymbol{I} & 0 \\ \boldsymbol{I} & 0 \\ 0 & \boldsymbol{I} \\ 0 & \boldsymbol{I} \end{bmatrix}, \quad \boldsymbol{J}_1^3 = \begin{bmatrix} \boldsymbol{I} & 0 \\ 0 & \boldsymbol{I} \\ 0 & 0 \\ 0 & 0 \\ 0 & 0 \\ 0 & 0 \\ 0 & 0 \\ 0 & 0 \end{bmatrix}, \quad \dots \quad \boldsymbol{J}_4^3 = \begin{bmatrix} 0 & 0 \\ 0 & 0 \\ 0 & 0 \\ 0 & 0 \\ 0 & 0 \\ 0 & 0 \\ \boldsymbol{I} & 0 \\ 0 & \boldsymbol{I} \end{bmatrix}. \tag{3.2.18}$$

We obtain the symmetrized gradient operator

$$\boldsymbol{D} = \begin{bmatrix} -c_{1,2}^1 \boldsymbol{B}(\boldsymbol{n}_1^1) & -c_{1,2}^2 \boldsymbol{B}(\boldsymbol{n}_1^2) & 0 & -c_{1,2}^3 \boldsymbol{B}(\boldsymbol{n}_1^3) & 0 & 0 & 0 \\ -c_{1,2}^1 \boldsymbol{B}(\boldsymbol{n}_1^1) & -c_{1,2}^2 \boldsymbol{B}(\boldsymbol{n}_1^2) & 0 & +c_{1,1}^3 \boldsymbol{B}(\boldsymbol{n}_1^3) & 0 & 0 & 0 \\ -c_{1,2}^1 \boldsymbol{B}(\boldsymbol{n}_1^1) & +c_{1,1}^2 \boldsymbol{B}(\boldsymbol{n}_1^2) & 0 & 0 & -c_{2,2}^3 \boldsymbol{B}(\boldsymbol{n}_2^3) & 0 & 0 \\ -c_{1,2}^1 \boldsymbol{B}(\boldsymbol{n}_1^1) & +c_{1,1}^2 \boldsymbol{B}(\boldsymbol{n}_1^2) & 0 & 0 & +c_{2,1}^3 \boldsymbol{B}(\boldsymbol{n}_2^3) & 0 & 0 \\ +c_{1,1}^1 \boldsymbol{B}(\boldsymbol{n}_1^1) & 0 & -c_{2,2}^2 \boldsymbol{B}(\boldsymbol{n}_2^2) & 0 & 0 & -c_{3,2}^3 \boldsymbol{B}(\boldsymbol{n}_3^3) & 0 \\ +c_{1,1}^1 \boldsymbol{B}(\boldsymbol{n}_1^1) & 0 & -c_{2,2}^2 \boldsymbol{B}(\boldsymbol{n}_2^2) & 0 & 0 & +c_{3,1}^3 \boldsymbol{B}(\boldsymbol{n}_3^3) & 0 \\ +c_{1,1}^1 \boldsymbol{B}(\boldsymbol{n}_1^1) & 0 & +c_{2,1}^2 \boldsymbol{B}(\boldsymbol{n}_2^2) & 0 & 0 & 0 & -c_{4,2}^3 \boldsymbol{B}(\boldsymbol{n}_4^3) \\ +c_{1,1}^1 \boldsymbol{B}(\boldsymbol{n}_1^1) & 0 & +c_{2,1}^2 \boldsymbol{B}(\boldsymbol{n}_2^2) & 0 & 0 & 0 & +c_{4,1}^3 \boldsymbol{B}(\boldsymbol{n}_4^3) \end{bmatrix} \in \mathbb{R}^{48 \times 21}. \tag{3.2.19}$$

Returning to the general case, we observe that the symmetrized gradient operator $\boldsymbol{D}$ is uniquely parameterized by the individual volume fractions $\boldsymbol{c}_j^k$ as well as the directions of lamination $\boldsymbol{n}_j^k$ of the collection of laminates. Thus, the vectors $\vec{\boldsymbol{n}}$ and $\vec{\boldsymbol{w}}$ of lamination directions and weights could serve to parametrize such a direct DMN.

In the implementation [69, 71], it is convenient to ensure non-negativity of the weights $\vec{\boldsymbol{w}} \in \mathbb{R}^{NK}$ by expressing them in terms of unconstrained weights $\vec{\boldsymbol{v}} \in \mathbb{R}^{NK}$ via applying the Macauley bracket (or ReLU activation function in machine learning)

$$\langle \cdot \rangle_+ : \mathbb{R} \to \mathbb{R}_{\geq 0}, \quad x \mapsto \max(0, x), \tag{3.2.20}$$

in a component-wise manner

$$\vec{\boldsymbol{w}} = \langle \vec{\boldsymbol{v}} \rangle_+. \tag{3.2.21}$$

Thus, the parameter vector which uniquely defines both the gradient operator $\boldsymbol{D}(\vec{\boldsymbol{p}})$ and the weight matrix $\boldsymbol{W}(\vec{\boldsymbol{p}})$ of a direct DMN is given by $\vec{\boldsymbol{p}} = (\vec{\boldsymbol{n}}, \vec{\boldsymbol{v}})$.

3.2.3 An inelastically-informed training strategy

Classically, DMNs are trained on objective functions of the form (3.2.6)

$$J(\vec{\boldsymbol{p}}) \equiv \sum_{s=1}^{n_{\text{obs}}} J_s(\vec{\boldsymbol{p}}) + \Psi(\vec{\boldsymbol{p}}) \longrightarrow \min_{\vec{\boldsymbol{p}}}, \tag{3.2.22}$$

where the functions $J_s(\vec{\boldsymbol{p}})$ measure the proximity of the current DMNs predictions to precomputed effective elastic properties. The term $\Psi(\vec{\boldsymbol{p}})$ serves as a regularizing term and is explicitly defined in Section 3.3.2.

Although DMNs, which are identified based on elastic data, show accurate predictions for large classes on nonlinear and inelastic constitutive laws for the microstructural phases, the developed theory [71] hints that such a close agreement may be lost if the constitutive laws show a high degree of nonlinearity. Therefore, it appears a good idea to add nonlinear constitutive laws to the training, encoded by an additional term $H(\vec{\boldsymbol{p}})$. Then, instead of the original problem (3.2.22), an augmented problem

$$J(\vec{\boldsymbol{p}}) + H(\vec{\boldsymbol{p}}) \longrightarrow \min_{\vec{\boldsymbol{p}}} \tag{3.2.23}$$

may be used to identify the parameters. Unfortunately, such an approach is restricted to rather simple inelastic material models [73], as the computational effort in evaluating complex constitutive laws, including computing the derivatives necessary for the gradient descent for a multitude of different loading conditions and time steps, quickly becomes prohibitive.

For this reason, we propose to use an alternative strategy which is similar in spirit to the commonly used *early stopping* [109, § 7.8] technique in machine learning. More precisely, in our strategy, the iterates $\vec{\boldsymbol{p}}_k$ of a conventional solver for the original problem (3.2.22) are stored in a set $\mathcal{P}$. Then, the additional term $H(\vec{\boldsymbol{p}})$, which encodes the performance of our model on the nonlinear inelastic constitutive laws is evaluated using the stored iterates $\vec{\boldsymbol{p}}_k$ during training. Finally, the best parameter vector

$$\vec{\boldsymbol{p}}_{\text{best}} = \operatorname{argmin}_{\vec{\boldsymbol{p}} \in \mathcal{P}} H(\vec{\boldsymbol{p}}) \tag{3.2.24}$$

is selected. It is common to store only each 50th or 100th iterate $\vec{\boldsymbol{p}}_k$ of the learning method, so that the runtime of such an early-stopping strategy will be reduced by one or two orders of magnitude compared to a coupled strategy (3.2.23) if the effort of evaluating the inelasticity-aware objective H is significantly larger than for the original objective (3.2.22).

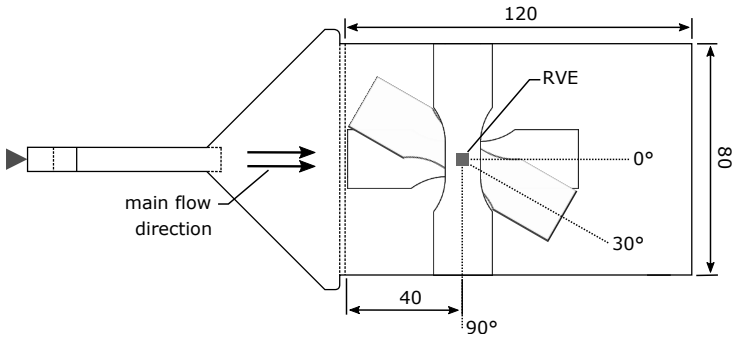

Figure 3.2: Prepared Becker [118] samples from composite plates with different directions adapted from Dey et al. [11, Fig. 2]

3.3 Computational investigations

3.3.1 Setup

We consider a polybutylene terephthalate (PBT), reinforced by 30% E-glass fibers (PBT-GF30). To characterize the matrix material, experiments were performed on a dog-bone shaped Becker sample [118], shown in Fig. 3.2, at the three load levels 23.5 MPa, 32.8 MPa and 37.5 MPa. The load was ramped up to the respective stress levels in 8.5 s, and held constant for different time intervals depending on the load level. The results are shown in Fig. 3.3(a). For all three load levels, we observe the typical three different creep phases [77]: primary, secondary, and tertiary creep. The creep-strain rate starts with a high value at the beginning of the primary creep stage and reaches an approximately constant value during the secondary creep stage. The tertiary state is characterized by an increase in the creep strain rate, leading to fracture of the specimen, eventually [78]. The first phase ends at roughly the same time for all three considered load levels. The onset of the third phase and the inclination of the strain at this onset, however, differ significantly for the three load levels.

For the matrix, we use a coupled plasticity-creep model, where the elastoplastic part accounts for short-term effects, whereas a viscoplastic augmentation accounts for long-term creep effects. We refer to Section 4.2.3 for details. To identify the free parameters, we used a two-step procedure. In a first step, the evolution of the creep strain was deactivated, and the elastic constants as well as the plasticity parameters were determined from uni-axial, monotone, tensile experiments up to 5% strain, performed for four different sam-

Matrix	Elastic	$E = 2399.3$ MPa	$\nu = 0.4$	
	Plastic	$h = 346.9$ MPa	$\omega = 384.9$	$y_0 = 20.9$ MPa
		$y_\infty = 51.9$ MPa		
	Creep	$A_1 = 0.014$ 1/MPa	$n_c = 32.4$	$A_2 = 1.5 \times 10^{-13}$ 1/MPa
		$C = 1870.1$	$k = 0.016$	$\dot{\varepsilon}_0 = 1.0$ s^{-1}
Fibers	Elastic	$E = 72\,000$ MPa	$\nu = 0.22$	

Table 3.1: Identified material parameters for PBT-GF30 adapted from Dey et al. [11, Tab. 1]

ples. For the parameter identification using OptiSlang [119], we set up a single-element unit-hexahedron model in Abaqus [120], and fixed the Poisson's ration to $\nu = 0.4$ and the viscosity to $\eta = 0.001$ MPa $\cdot$ s, emulating strain-rate independence.
Once the elasticity and plasticity coefficients were determined, the remaining creep parameters were identified from long-term creep tests carried out at different load levels, see Fig. 3.3(a), based on OptiSlang [119], wrapping an Abaqus [120] simulation. The model predictions with the identified parameters are compared to the experimental results in Fig. 3.3(a). The model captures the three creep phases rather well, and represents the three experimental results to a sufficient accuracy. The entire parameter identification workflow is explicitly defined in Section 4.2.4. The final list of identified parameters is given in Tab. 3.1. For the E-glass fibers, we use standard parameters [121].
It is well-known that the mechanical properties of fiber-reinforced composites strongly depend on the microstructure characteristics like fiber orientation and fiber length distribution [122, 123]. To quantify the microstructure characteristics, we rely upon micro-computed tomography [124–126]. More precisely, we determined the volume-average fiber length of 269 μm, a fiber diameter of 10 μm and the second-order fiber-orientation tensor

$$\mathbf{A} = \begin{bmatrix} 0.213 & 0.006 & 0.001 \\ & 0.770 & -0.004 \\ \texttt{sym} & & 0.017 \end{bmatrix} \tag{3.3.1}$$

by the method discussed in Hessman et al. [7] for a specimen milled out from a 120 mm $\times$ 80 mm $\times$ 2 mm injection-molded plate, see Fig. 3.2. We used this data to reconstruct a digital microstructure with the SAM algorithm [127], see Fig. 3.3(b). We generated a cubic unit cell with an edge length of 625 μm containing 2 056 cylindrical fibers with a

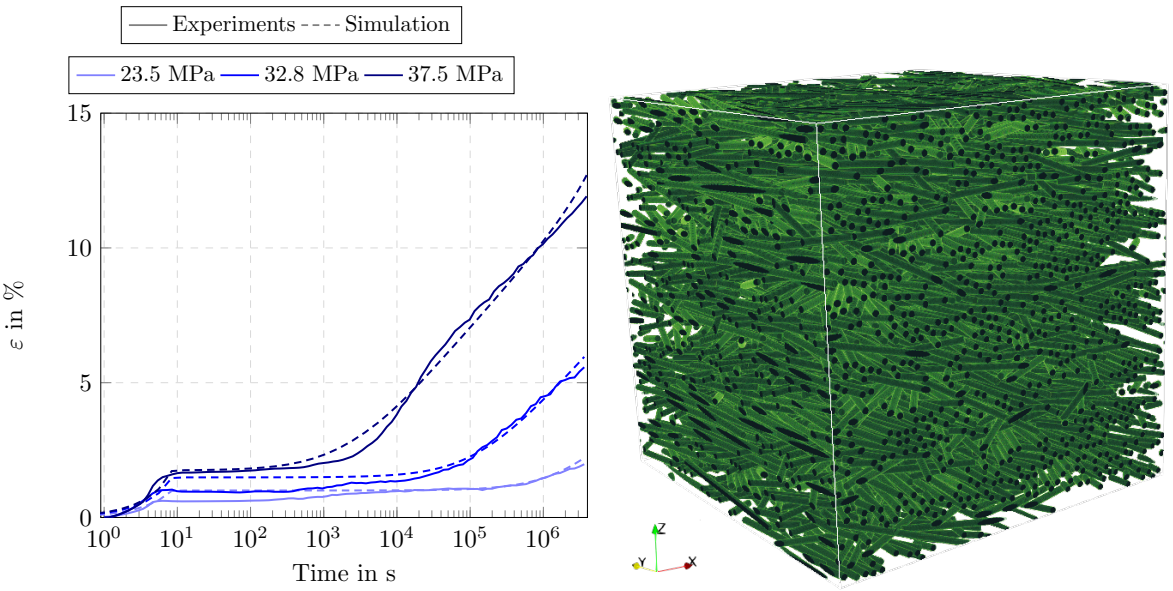

(a) Experiments and model for PBT (b) Generated microstructure

Figure 3.3: A comparison of experimental results and model predictions for the PBT matrix and generated periodic fiber-filled microstructure adapted from Dey et al. [11, Fig. 3]

length of 269 μm and a diameter of 10 μm with a minimum distance of 3 μm between the fibers. The second-order fiber-orientation tensor (3.3.1) was prescribed, combined with the exact closure approximation [128, 129].

The microstructure was discretized by 512^3 voxels. For the subsequent FFT computations, we used the composite-voxel technique [130–132] with a resampling factor of two. Thus, after resampling, the unit cell consists of 256^3 voxels. The computation time when performing a linear elastic FFT simulation using a phase contrast of 10 000 and a unit cell discretized by 512^3 voxels was 19.9 h. In comparison, the resampled microstructure with 256^3 voxels and composite voxels required just 2.38 h. The resampling error between the stiffness tensors is just 1.12% in the Frobenius norm in Mandel notation. As, in the case of a lower phase contrast, an even smaller error is expected, the composite-voxel method serves as a reasonable way to speed up the computations.

Last but not least, let us discuss the used soft- and hardware. The micromechanical computations were performed with the software FeelMath [133] on a HPC cluster with nodes that have 16 CPUs each and 4 GB of memory per CPU. FeelMath [133] implements FFT-based computational homogenization methods. More precisely, we used the

staggered grid discretization [47, 134] and linear as well as nonlinear conjugate gradient methods [135–137] for linear and nonlinear constitutive behavior, respectively.
The DMN was trained on a single CPU with 60 GB of memory. The DMN online phase code was run on a single computing node.
Both the material model and the DMN were implemented as user-defined material subroutines (UMATs) in Abaqus [120], which may also be used in FeelMath [133]. We use the LAPACK [138] libraries for the linear algebra operations.

3.3.2 Performance of classical sampling

We consider a microstructure with $N = 2$ phases, i.e., the PBT matrix and the E-glass fibers. We use the direct DMN described in Section 3.2.2, and initialize the parameters $(\vec{\boldsymbol{n}}, \vec{\boldsymbol{v}})$ as proposed in Gajek et al. [71].
For the training, we generated training and validation data based on full-field FFT-based computational homogenization. This data consists of triples $\left(\mathbb{C}_1^s, \mathbb{C}_2^s, \bar{\mathbb{C}}_{\mathtt{FFT}}^s\right)$, where $\mathbb{C}_1^s$ and $\mathbb{C}_2^s$ serve as the linear elasticity tensors of the two materials, and $\bar{\mathbb{C}}_{\mathtt{FFT}}^s$ refers to the effective elasticity tensor. The tuples $(\mathbb{C}_1^s, \mathbb{C}_2^s)$ were sampled by the method proposed by Liu and Wu [70] utilizing orthotropic elasticity tensors. The effective properties $\bar{\mathbb{C}}_{\mathtt{FFT}}^s$ were computed with FeelMath [133]. We generated 1 000 samples as mentioned, split into 800 training and 200 validation points.
For fixed DMN parameters $(\vec{\boldsymbol{n}}, \vec{\boldsymbol{v}})$, we denote by $\bar{\mathbb{C}}_{\mathtt{DMN}}^s(\vec{\boldsymbol{n}}, \vec{\boldsymbol{v}})$ the effective stiffness computed by the DMN with phase stiffnesses $\mathbb{C}_1^s$ and $\mathbb{C}_2^s$. We refer to Gajek et al. [71] for details how to evaluate the effective stiffness $\bar{\mathbb{C}}_{\mathtt{DMN}}^s(\vec{\boldsymbol{n}}, \vec{\boldsymbol{v}})$ efficiently.
For the offline training with linear elastic data, we minimize the objective function (3.2.6), i.e.,

$$J(\vec{\boldsymbol{n}}, \vec{\boldsymbol{v}}) \longrightarrow \min_{\vec{\boldsymbol{n}}, \vec{\boldsymbol{v}}} \quad \text{with} \quad J(\vec{\boldsymbol{n}}, \vec{\boldsymbol{v}}) = \sum_{s=1}^{n_{\mathtt{b}}} J_s(\vec{\boldsymbol{n}}, \vec{\boldsymbol{v}}) + \Psi(\vec{\boldsymbol{n}}, \vec{\boldsymbol{v}}), \tag{3.3.2}$$

with the batch size $n_{\mathtt{b}} = 40$, the contributions

$$J_s(\vec{\boldsymbol{n}}, \vec{\boldsymbol{v}}) = \frac{1}{n_{\mathtt{b}}} \frac{\left\| \bar{\mathbb{C}}_{\mathtt{FFT}}^s - \bar{\mathbb{C}}_{\mathtt{DMN}}^s(\vec{\boldsymbol{n}}, \vec{\boldsymbol{v}}) \right\|_1}{\left\| \bar{\mathbb{C}}_{\mathtt{FFT}}^s \right\|_1} \tag{3.3.3}$$

and

$$\Psi(\vec{\boldsymbol{n}}, \vec{\boldsymbol{v}}) = \lambda \left(\mathbf{b}_1^T \langle \vec{\boldsymbol{v}} \rangle_+ - c_1 \right) + \lambda \left(\mathbf{b}_2^T \langle \vec{\boldsymbol{v}} \rangle_+ - c_2 \right), \tag{3.3.4}$$

where $c_1 = 0.822$ and $c_2 = 0.178$ denote the volume fractions of the respective phases, $\mathbf{b}_1$ is a vector that has ones at all odd indices and is zero otherwise, $\mathbf{b}_2$ is a vector that has ones at all even indices and is zero otherwise, and λ refers to a penalty factor which we set to 100. The term Ψ enforces the respective volume fractions of both phases [139]. This approach differs from previous works [69–71], where the total volume fraction of the DMN is enforced to unity. Instead, we enforce the respective volume fractions of each of the phases. We found empirically that such a strategy increases the reliability of the offline training.

We use the ℓ^1-norm in eq. (3.3.3) since an independent study with ℓ^p-norms and variable exponents p revealed that the subsequently trained DMNs capture the inelastic creep response most closely for $p = 1$. For reasons of conciseness, we chose not to report this study here.

The training, i.e., the minimization of the objective function (3.3.2), proceeds as for (more general) neural networks, i.e., via a stochastic batch-gradient-descent-type algorithm based on automatic differentiation and a grouping into batches (we use batches of size 40). We implemented the procedure in PyTorch [140] and used the AMSGrad method [141] for training the network along with a learning-rate modulation using cosine annealing [142],

$$\beta(m) = \beta_{\texttt{min}} + \frac{1}{2}(\beta_{\texttt{max}} - \beta_{\texttt{min}}) \left(1 + \cos\left(\pi \frac{m}{M}\right)\right), \tag{3.3.5}$$

where β and m refer to the learning rate and epoch, respectively. We use a maximum learning rate $\beta_{\texttt{max}} = 0.0007$ and a minimum learning rate $\beta_{\texttt{min}} = 0$. The parameter M is set to 4000. The training of the DMN was performed up to 25 000 epochs. The typical progress during training is shown in Fig. 3.4(a). For the first 100 epochs, the objective function decreases monotonically. Thereafter, the loss function shows some fluctuations. These are triggered by the learning-rate modulation which enables escaping local minima of the objective function. Indeed, on a large scale, a further decrease of the objective function up to around epoch 20 000 is observed. For the considered example, the smallest loss occurred at epoch 19 962. The training ran for 18.8 h. After training, we used the DMN with the smallest *realized* loss for further use.

We investigated the effect of depth on the online evaluation of creep and found that the performance of the DMN in the online phase increases up to a depth of seven. For higher depth, no further improvement in accuracy for the evaluation of creep in the online phase was observed. We trained our seven-layer DMN on 800 training samples. To assess

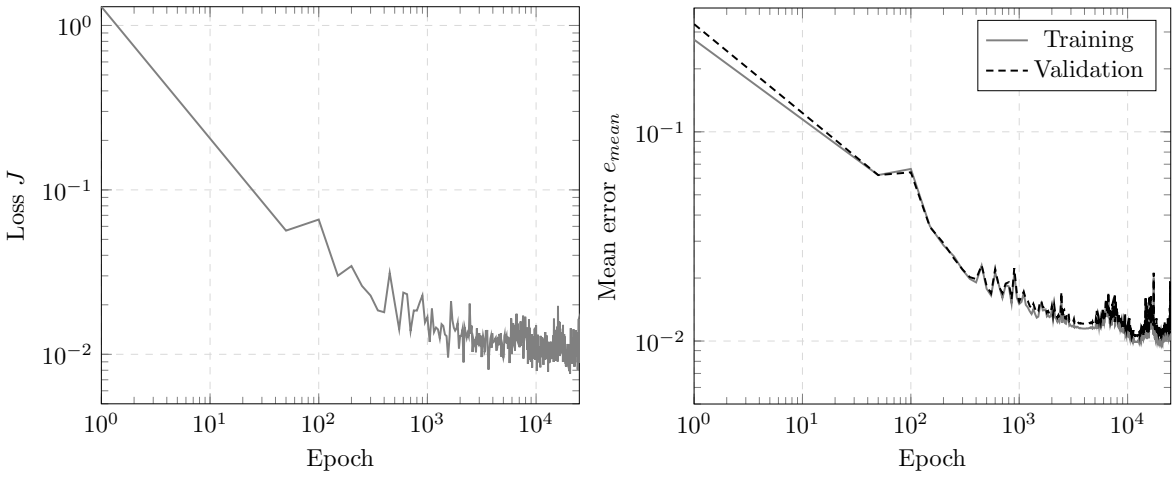

(a) Loss function

(b) Mean error

Figure 3.4: Offline training results and mean training and validation errors of DMN #1 from Tab. 3.2 adapted from Dey et al. [11, Fig. 1], adapted from Dey et al. [11, Fig. 6]

the reproducibility of the results, we trained multiple seven-layer DMNs with the same hyperparameters but with random starting values of the parameters $(\vec{\boldsymbol{n}}, \vec{\boldsymbol{v}})$.
To assess the generalization capabilities of the DMN, we introduce the sample-wise error

$$e_s = \frac{\left\| \bar{\mathbb{C}}^s_{\mathtt{FFT}} - \bar{\mathbb{C}}^s_{\mathtt{DMN}} \right\|_1}{\left\| \bar{\mathbb{C}}^s_{\mathtt{FFT}} \right\|_1}, \tag{3.3.6}$$

involving the the relative ℓ^1-difference of the actual stiffness tensor $\bar{\mathbb{C}}^s_{\mathtt{FFT}}$ and the predicted stiffness tensor $\bar{\mathbb{C}}^s_{\mathtt{DMN}}$ in Mandel's notation. Moreover, we define the maximum and the mean errors over all the samples

$$e_{\mathtt{max}} = \max_s e_s \quad \text{and} \quad e_{\mathtt{mean}} = \frac{1}{N_s} \sum_{s=1}^{N_s} e_s, \tag{3.3.7}$$

where N_s is the number of samples in the training or the validation set, respectively. After the training, we studied the generalization capabilities of the model with the help of linear elastic validation data comprising 200 data points. The results of the training and the validation errors are detailed in Tab. 3.2. We observe that the reached loss value is comparable for all six considered DMNs. Also, the mean training and validation error is rather close for all considered networks. We find that the mean training error is slightly smaller than the mean validation error for all the networks. The maximum training error for all the networks is around 13%. The maximum validation error ranges from slightly

DMN #	Smallest Loss	$e^{\mathtt{tr}}_{\mathtt{mean}}$	$e^{\mathtt{tr}}_{\mathtt{max}}$	$e^{\mathtt{val}}_{\mathtt{mean}}$	$e^{\mathtt{val}}_{\mathtt{max}}$
1	0.00591	0.97%	12.78%	1.08%	5.10%
2	0.00567	0.96%	12.90%	1.07%	6.36%
3	0.00612	1.01%	13.03%	1.11%	6.17%
4	0.00600	1.02%	13.41%	1.15%	5.90%
5	0.00592	0.98%	13.66%	1.07%	4.19%
6	0.00502	0.96%	13.09%	1.04%	4.76%

Table 3.2: Elastic training results of seven-layer DMNs adapted from Dey et al. [11, Tab. 2]

above 4% to almost 7%, i.e., we find a larger variation (roughly by a factor of two). Still, the elastic training and validation errors are on a reasonable level, in particular in view of the mean errors.

The mean training and validation errors for DMN #1 over the course of epochs is shown in Fig. 3.4(b). We observe that the mean training and validation errors follow a similar trend as the loss function. Moreover, the training and validation error decrease simultaneously during training indicating no overfitting occurs in the offline training phase with respect to the linear elastic training data.

We use our six trained DMNs to evaluate the online phase. We briefly comment on the elastoplastic response of the DMNs. The online phase of the DMN, implemented as an UMAT, is evaluated on a single four-node unit tetrahedron element in Abaqus [120]. We use the load increment control of Abaqus [120] for applying the load, and compare the output to full-field simulations obtained by an FFT-based solver [137]. We applied hysteretic, uniaxial strain loadings $\bar{\varepsilon}_{ij}$ for a period of 4 s with a strain amplitude of 2.5% for 40 load steps in all six loading directions. For each instance of time t, the relative error in each stress component

$$e^{p}_{ij,t} = \frac{\left|\bar{\sigma}^{\mathtt{DMN}}_{ij,t} - \bar{\sigma}^{\mathtt{FFT}}_{ij,t}\right|}{\max_{\tau}\left|\bar{\sigma}^{\mathtt{FFT}}_{ij,\tau}\right|} \tag{3.3.8}$$

is considered, together with the maximum relative error

$$e^{p}_{ij} = \max_{\tau} e^{p}_{ij,\tau} \tag{3.3.9}$$

over the entire simulation window.

In addition to the elastoplastic response, we also investigate the creep behavior. To

account for the anisotropy of the microstructure, we investigate the performance of the DMN in three loading directions with angles 0°, 30°, and 90°. Here, the 0° direction indicates the flow direction and the 90° direction is perpendicular to the flow direction during the manufacturing of the test plate. The experimental analysis of the creep loading was performed using the samples cut out from the injection molded plate in these specific angles as shown in Fig. 3.2. The creep response of the DMN was evaluated on a single voxel microstructure using an FFT-based solver [137]. The implemented DMN online phase UMAT can be flexibly integrated into the FFT-based solver FeelMath [133]. We consider 32 time steps, equally spaced in the logarithmic time scale. The DMN response was compared with the effective stresses computed by full-field simulations performed with the same FFT-based solver [137].

In the 0° direction, we applied a uni-axial tensile stress $\bar{\sigma}_{11}$ in the flow direction which is ramped up to 65.4 MPa in 8.5 s and subsequently held constant for 3.78×10^6 s. We evaluated the creep strain component $\bar{\varepsilon}_{11}$ in the flow direction over the entire simulation window. In the 0° direction, we refer to the evaluated strain by the name $\bar{\varepsilon}_{0^\circ}$. We apply a lower uni-axial stress $\bar{\sigma}_{22}$ of 35.7 MPa until 3.78×10^6 s for the creep response in the 90° direction. We evaluate the stress component $\bar{\varepsilon}_{22}$ during loading and assign the results to $\bar{\varepsilon}_{90^\circ}$.

For the 30° direction, we follow a similar strategy using mixed boundary conditions [143] for a uni-axial tensile stress of 69 MPa, held constant up to 4.45×10^5 s. During the entire simulation time, we evaluated the creep strain component $\bar{\varepsilon}_{11}$, and refer to it as $\bar{\varepsilon}_{30^\circ}$.

For the creep loading, we consider the relative strain errors

$$e^c_{\theta,t} = \frac{\left|\bar{\varepsilon}^{\mathtt{DMN}}_{\theta,t} - \bar{\varepsilon}^{\mathtt{FFT}}_{\theta,t}\right|}{\max_\tau \left|\bar{\varepsilon}^{\mathtt{FFT}}_{\theta,\tau}\right|} \quad \text{for} \quad \theta = 0^\circ, 30^\circ, 90^\circ \tag{3.3.10}$$

and the maximum errors

$$e^c_\theta = \max_\tau e^c_{\theta,\tau} \quad \text{as well as} \quad e^c = \max_\theta e^c_\theta. \tag{3.3.11}$$

The trained DMNs whose elastic validation results are shown in Tab. 3.2 are used for the online evaluation of plasticity and creep. Tab. 3.3 contains the results for the inelastic evaluation. For the maximum error during the elastoplastic loading, we observe a variation of the results by a factor of three. DMN #1 leads to a low relative error slightly below 3%. Three DMNs give rise to about 5% error, and two DMNs are characterized by a relative error slightly below 10%. Taking a glance at the elastic validation errors, see Tab. 3.2, we observe that the DMN with the best elastoplastic online error does not

DMN #	$\max_{ij} e^p_{ij}$	$e^c_{0°}$	$e^c_{30°}$	$e^c_{90°}$	e^c
1	2.97%	5.57%	5.67%	4.36%	5.67%
2	9.87%	17.40%	3.06%	3.62%	17.40%
3	8.41%	13.51%	23.03%	6.02%	23.03%
4	4.41%	1.52%	3.04%	1.91%	3.04%
5	5.55%	5.77%	4.80%	5.68%	5.77%
6	5.21%	5.35%	9.33%	3.56%	9.33%

Table 3.3: Maximum relative errors for elastoplastic (3.3.9) and creep loading (3.3.11) adapted from Dey et al. [11, Tab. 3]

correspond to the DMN with the best elastic validation error.
Even more striking are the variations in the creep response. Whereas DMNs #1, #4 and #5 provide a rather small creep error, two DMNs give rise to relative creep errors on the order of 20%, which is certainly not acceptable for engineering accuracy. Moreover, we notice that the maxima are realized in different directions. Indeed, for DMN #2, the 0°-direction is worst, but the 30°-direction is matched rather accurately. In contrast, for DMN #3, both the 0° and the 30°-direction are inaccurate. Thus, there appears to be no systematic cause for this phenomenon, e.g., related to the fiber orientation. We observe that the DMN #1, #4 and #5 can represent both the elastoplastic loading and creep accurately. In contrast, the DMNs #2 and #3 are incapable of representing the creep loading with sufficient fidelity.
To sum up, the results of Tab. 3.3 reveal that good results achieved during the elasticity-based training results do not necessarily lead to accurate predictions for the creep response. We will study this phenomenon more thoroughly in the next section.

3.3.3 Accurate creep predictions with early stopping and a surrogate material model

In the previous section, we observed that being a minimizer of the elasticity-based loss function (3.3.2)–(3.3.3) is not necessarily related to providing an accurate creep prediction for the DMN under consideration. To get a deeper insight into this phenomenon, we took a closer look at DMN #6 from Tab. 3.3. More precisely, we stored the DMN parameters

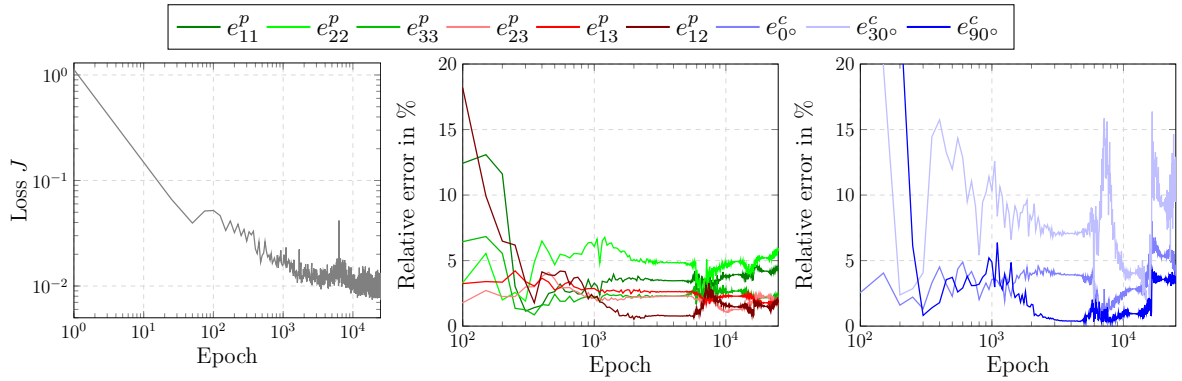

(a) Loss vs epochs (b) Relative error for plasticity (c) Relative error for creep

Figure 3.5: A closer look at DMN #6 from Tab. 3.3 in terms of the loss function and the plasticity (3.3.9) as well as creep errors (3.3.11) (every 50 epochs), evaluated in postprocessing adapted from Dey et al. [11, Fig. 5]

$(\vec{\boldsymbol{n}}_k, \vec{\boldsymbol{v}}_k)$ every 50 epochs during the training. As a postprocessing step, we evaluated the elastoplastic (3.3.9) and the creep errors (3.3.11) at these parameter states $(\vec{\boldsymbol{n}}_k, \vec{\boldsymbol{v}}_k)$. The results, alongside the loss function, are shown in Fig. 3.5. In Fig. 3.5(a), we observe that the loss function decreases in a similar way as for DMN #1, see Fig. 3.4(a). The decrease is monotonic on large epoch scales, but shows variations up to half an order of magnitude during training as a result of the learning-rate modulation. Taking a look at the plasticity errors (3.3.9) for the six considered loading directions, see Fig. 3.5(b), we observe that the errors decrease consistently up to epoch 300. Then, only the error of the 12-component decreases further, whereas the other five errors more or less remain on the same level. At epoch 6 000, the 12-error starts to increase significantly, whereas the 22-error - the largest up to this epoch - starts to decrease. For epochs exceeding 10 000, the maximum error $\max_{i,j} e^p_{ij}$ starts to increase again.

Similar observations may be made for the creep error (3.3.11), shown in Fig. 3.5(c). For the first 300 epochs, the error decreases. For higher epochs, the errors in the considered directions show a non-monotonic behavior. However, the creep error is much larger than the plasticity error, in a range up to 15%. Interestingly, there is a range of epochs, approximately at 10 000, where the creep error is low, below 5%. This smallness is neither reflected in the loss function nor the plasticity error.

In the terminology of deep learning, the observed phenomenon may be interpreted as "overfitting", i.e., producing parameters that correspond too closely to a specific set of

data, but fail to represent additional data or to predict future observations in a reliable way.

Classically, there are (at least) two ways to rectify this shortcoming. The first strategy consists of adding further data points to the considered set. In our case, we could augment the classical elasticity-based offline training by more cleverly chosen stiffness triples $\left(\mathbb{C}_1^s, \mathbb{C}_2^s, \bar{\mathbb{C}}_{\mathtt{FFT}}^s\right)$ or by including inelastic data into the loss function [73]. Unfortunately, such a strategy does not protect us from overfitting relative to *other cases* which were not considered before. In the case of inelastic training for reproducing creep loading, training on inelastic data for the 0° direction does not guarantee us a good fit in the 30° and 90° directions. Therefore, an alternative way to circumvent overfitting is to stop early [109, § 7.8], i.e., to stop at a stage where the fitting quality of the considered data in the linear elastic regime (3.2.6) *and* an additional independent nonlinear validation data set are both good. In the former case, the training and validation error can be monitored so that there is no overfitting during the offline elastic training. In the latter case, the performance of the DMN in the inelastic regime should be within engineering accuracy when compared with inelastic full-field simulations. Indeed, by monitoring the additional data, we may detect when overfitting happens in the inelastic regime.

The analysis at the beginning of this section, in particular given in Fig. 3.5(c), shows that early stopping based on the additional term (3.3.11)

$$H(\vec{\boldsymbol{n}}, \vec{\boldsymbol{v}}) = e^c(\vec{\boldsymbol{n}}, \vec{\boldsymbol{v}}) \equiv \max_{\theta} e_\theta^c(\vec{\boldsymbol{n}}, \vec{\boldsymbol{v}}) \tag{3.3.12}$$

does indeed work for DMN #6. The DMN #6 trained on linear elastic data can accurately predict the online inelastic response of highly non-linear material models, providing a maximum relative creep error below 5%.

Thus, the strategy proposed in Section 3.2.3 works and, in theory, we can perform the evaluation of the creep model during training for identification of the best parameter vector.

However, we are interested in a further improvement of the strategy. Due to the complexity of the considered creep model, the post-processing for evaluating the creep error $e^c(\vec{\boldsymbol{n}}, \vec{\boldsymbol{v}})$ ran for 24.4 h. In particular, the post-processing took 30% longer than the previous elasticity-based training! Hence, performing the evaluation of the creep model during the elasticity-based training will lead to a cumbersome and time-intensive training procedure. Clearly, the long-term creep behavior demands certain characteristics of the DMNs to be accurate, and isolating the proper elastic training data appears difficult. To

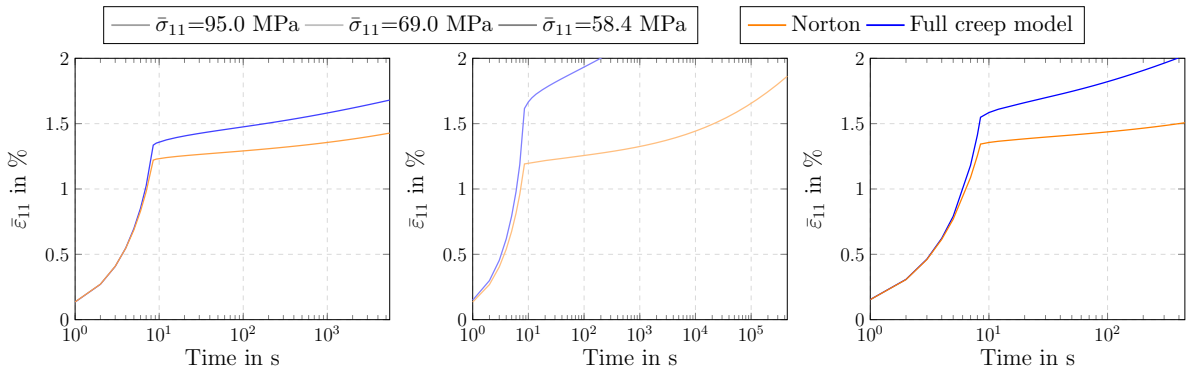

(a) 0°-direction (b) 30°-direction (c) 90°-direction

Figure 3.6: Full-field results for the creep strain over time, comparing the Norton-type model (3.3.13) for the matrix and the full creep model, see Section 4.2.3, adapted from Dey et al. [11, Fig. 6]

Matrix	Elastic	$E = 2399.3$ MPa	$\nu = 0.4$	
	Creep	$A_n = 0.014$ 1/MPa	$n_n = 26.96$	$\dot{\varepsilon}_0 = 1.0$ s^{-1}

Table 3.4: Identified material parameters for the Norton-type model (3.3.13) adapted from Dey et al. [11, Tab. 4]

reduce the computational effort of evaluating the full creep model, we came up with the following idea. Instead of the full creep model, it might be sufficient to consider another creep model, which is, on the one hand, less expensive to evaluate, but, on the other hand, identifies the same weaknesses in generalization to long-term loading as the full-field model. For this purpose, we consider Hooke's law in combination with a Norton-type creep law [78]

$$\begin{aligned} \boldsymbol{\sigma} &= \kappa \operatorname{tr}[\boldsymbol{\varepsilon}]\boldsymbol{1} + 2\mu \operatorname{dev}[\boldsymbol{\varepsilon} - \boldsymbol{\varepsilon}^{\mathrm{c}}] \\ \dot{\boldsymbol{\varepsilon}}^{c} &= \dot{\varepsilon}_0 (A_n \sqrt{3/2}\, \|\operatorname{dev} \boldsymbol{\sigma}\|)^{n_n} \frac{\operatorname{dev}[\boldsymbol{\sigma}]}{\|\operatorname{dev}[\boldsymbol{\sigma}]\|} \end{aligned} \tag{3.3.13}$$

with creep parameters A_n and n_n.

We chose the parameters as detailed in Tab. 3.4. The elastic parameters coincide with the full creep model, as does the parameter $A_n \equiv A_1$, see Tab. 3.1. The creep exponent n_n and the parameter A_n were identified with the help of the long-term creep experiments carried out at different load levels and an OptiSlang [119] procedure based on an Abaqus [120] simulation. We conducted full-field simulations on the considered microstructure, see

Fig. 3.3(b), with the Norton model (3.3.13) for the matrix material. For the three considered directions, see Fig. 3.6, we observe that both the elastic response and the first creep phase are captured rather accurately by the simplified model. Moreover, the onset of the secondary creep phase is also represented quite well. However, the effective strains are underestimated by the Norton-type model for the creep phase two and beyond.

In analogy to the true creep error (3.3.11), we define an error measure for the creep response of the Norton model

$$e^n_{\theta,t} = \frac{\left|\bar{\varepsilon}^{\mathtt{DMN,Norton}}_{\theta,t} - \bar{\varepsilon}^{\mathtt{FFT,Norton}}_{\theta,t}\right|}{\max_\tau \left|\bar{\varepsilon}^{\mathtt{FFT,Norton}}_{\theta,\tau}\right|} \quad \text{for} \quad \theta = 0°, 30°, 90° \tag{3.3.14}$$

and the maximum errors

$$e^n_\theta = \max_\tau e^n_{\theta,\tau} \quad \text{as well as} \quad e^n = \max_\theta e^n_\theta. \tag{3.3.15}$$

To assess the predictive quality of the Norton error e^n, we trained two additional DMNs with a maximum learning rate $\beta_{\mathtt{max}} = 0.0005$. During the offline training of the DMN based on the linear elastic data, we introduce an *inelastic validation data set* based on the Norton errors for $0°, 30°$ and $90°$ directions. We consider this validation data set *in addition* to the linear elastic validation data set which is monitored during the training to prevent the overfitting in the elastic regime, see Fig. 3.4(b).

The linear elasticity-based training proceeds as in Section 3.3.2, via a stochastic batch-gradient-descent-type algorithm. We evaluate the loss function $J(\vec{\boldsymbol{p}})$ 3.3.2 involving the parameters $\vec{\boldsymbol{p}} = (\vec{\boldsymbol{n}}, \vec{\boldsymbol{v}})$, determine the gradients $\partial J/\partial \vec{\boldsymbol{n}}$ and $\partial J/\partial \vec{\boldsymbol{v}}$ via automatic differentiation and finally update the fitting parameters. The parameter vector $\vec{\boldsymbol{p}}$ is stored every 50 epochs to evaluate the *inelastic validation data set*, wherein the Norton error $e^n(\vec{\boldsymbol{p}})$ (3.3.15) is calculated. This serves as the basis for identifying the best parameter vector $\vec{\boldsymbol{p}}_{\text{best}}$.

In a classical early-stopping approach, the validation data set error is monitored and the training is stopped when the error does not improve for a predefined number of states. A copy of the model parameters are stored every time the error on the validation set improves. The parameters with the best validation error rather than the most recent parameters are returned once the training algorithm is terminated [109, § 7.8].

In our case, the *inelastic validation error* does not show a monotonic decrease and has persistent fluctuations, see Figs. 3.5(b), 3.5(c), which is a consequence of the learning-rate modulation (3.3.5) used during training. Thus, terminating the training once the *inelastic validation error* has not improved for a predefined number of epochs (which results

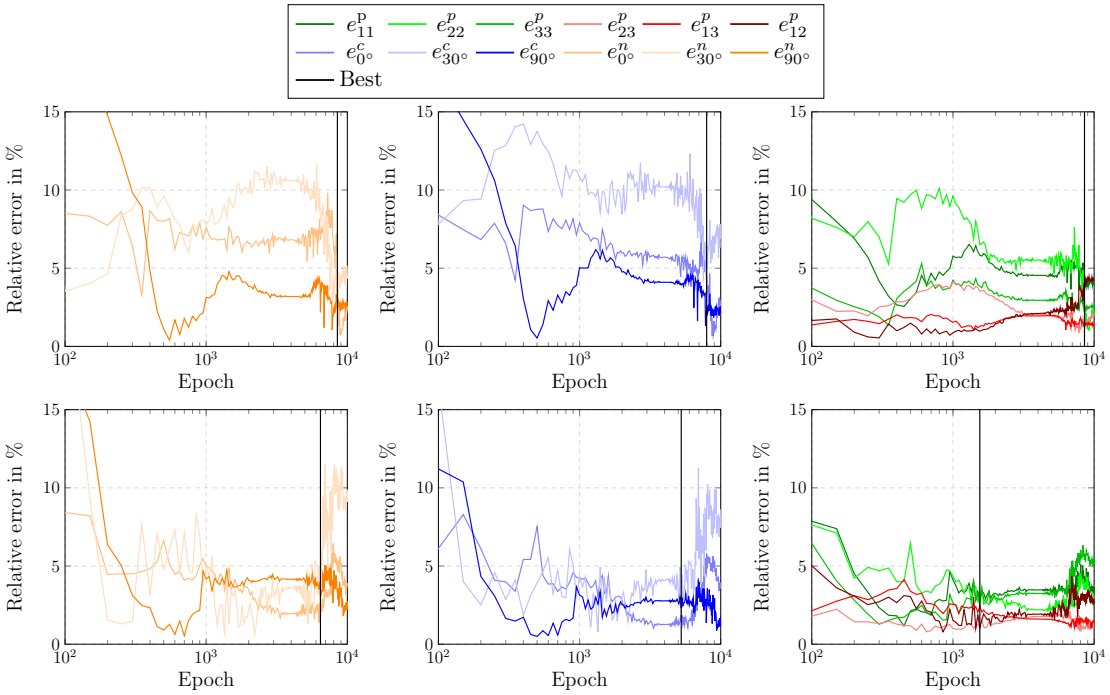

(a) Norton error (b) Creep error (c) Plasticity error

Figure 3.7: Comparison of the three inelastic error measures over epochs for DMN #1 (top) and DMN #2 (bottom) from Tab. 3.5, adapted from Dey et al. [11, Fig. 7]

in an additional hyperparameter introduced into the procedure) is not appropriate. As an alternative, we monitor the Norton error $e^n(\vec{\boldsymbol{p}})$ on-the-fly every 50 epochs and store the parameters each time the Norton error improves, for the complete training. More precisely, after the end of 10 000 epochs, we return the parameter vector $\vec{\boldsymbol{p}}_{\text{best}}$ from the state (evaluated every 50 epochs) having the best *inelastic validation error*, i.e., the least Norton error. This *quasi-early-stopping* approach for the inelastically-informed training methodology is outlined in Algorithm 1.

The results of the evaluation of the *inelastic validation data set* over the course of training is shown in Fig. 3.7(a). We also performed the creep and plasticity evaluation using the fully coupled plasticity-creep law as a post-processing step, see Fig. 3.7(b) and 3.7(c) respectively. The creep and plasticity errors are not used for identifying the best DMN and the plots are presented in Fig. 3.7 to highlight the correlation between evolution of the Norton error during training with the post-processed results.

Again we observe differences in the error measures between the considered DMNs. Indeed,

DMN #	Training time	e^p	e^c	e^n	Stored at epoch	Evaluation e^c time
1	12.07h	4.36%	5.32%	3.57%	8 500	8.7h
2	12.37h	3.19%	3.43%	3.33%	6 450	8.1h

Table 3.5: Results of online evaluation of DMN with the inelastically-informed offline training method - the training time includes evaluating the Norton model adapted from Dey et al. [11, Tab. 5]

Algorithm 1 Quasi-early-stopping training approach

$\vec{\boldsymbol{p}} \leftarrow (\vec{\boldsymbol{n}}, \vec{\boldsymbol{v}})$ ▷ Initialize parameter vector randomly

$e^n_{\text{best}} \leftarrow 1000000$ ▷ Inelastic validation error initialized with a high value before optimization start

for *epoch* $\leftarrow 1, 10000$ **do**

Calculate loss function

$\bar{\mathbb{C}}^s_{\texttt{DMN}}(\vec{\boldsymbol{p}}) \leftarrow \bar{\mathbb{C}}^s_{\texttt{DMN}}(\vec{\boldsymbol{n}}, \vec{\boldsymbol{v}})$

$J(\vec{\boldsymbol{p}}) \equiv \sum_{s=1}^{n_{\texttt{b}}} J_s(\vec{\boldsymbol{p}}) + \Psi(\vec{\boldsymbol{p}})$ ▷ Calculated for every batch $n_{\texttt{b}}$ (3.3.3)

Update parameter vector

$\vec{\boldsymbol{n}} \leftarrow \vec{\boldsymbol{n}} - \beta\, \partial J / \partial \vec{\boldsymbol{n}}(\vec{\boldsymbol{p}})$ ▷ β is the learning rate

$\vec{\boldsymbol{v}} \leftarrow \vec{\boldsymbol{v}} - \beta\, \partial J / \partial \vec{\boldsymbol{v}}(\vec{\boldsymbol{p}})$

$\vec{\boldsymbol{p}} \leftarrow (\vec{\boldsymbol{n}}, \vec{\boldsymbol{v}})$

if *epoch* mod $50 = 0$ **then**

Calculate error measure for Norton model (3.3.15) for on-the-fly inelastic validation

$e^n(\vec{\boldsymbol{p}}) \leftarrow \max_\theta e^n_\theta(\vec{\boldsymbol{p}})$

if $e^n(\vec{\boldsymbol{p}}) < e^n_{\text{best}}$ **then**

$e^n_{\text{best}} \leftarrow e^n(\vec{\boldsymbol{p}})$

Update best parameter vector to be returned at end of training with the current parameters

$\vec{\boldsymbol{p}}_{\text{best}} \leftarrow (\vec{\boldsymbol{n}}, \vec{\boldsymbol{v}})$

end if

end if

end for

taking a look at the plasticity error shown in Fig. 3.7(c), we observe e^p_{22} is largest for DMN #1 and e^p_{11} is largest for DMN #2 at the end of the training. We also observe differences between the plasticity error, see Fig. 3.7(c), and the creep error, see Fig. 3.7(b), for both DMNs. For instance, the large dip of $e^c_{90°}$ for DMN #1 is not reflected by particularly low values of the plasticity error in any component. Comparing the Norton and the creep error, see Figs. 3.7(a) and 3.7(b), respectively, leads to a better resemblance. Indeed, after epoch 1 000 there is a good agreement between the trends of the Norton errors and the creep errors for the individual loading directions. This correspondence is also underlined by the identified epochs where the respective error is lowest during training. For DMN #1, the best epoch is very similar for all three considered error measures. For DMN #2, the best plasticity error is reached a few thousand epochs before the best creep-error epoch, which is, in turn, closely matched by the best Norton-error epoch. For both DMNs, the errors are reported in Tab. 3.5. We observe that the DMNs identified by early stopping based on the Norton error e^n provide both a good creep and plasticity error, slightly above 3%. Actually, the minimum reached Norton error exceeds both other considered error measures.

The minimum creep error e^c for DMN #1 over 10 000 epochs is 4.49% captured at epoch 7 950. This is rather close to the creep error e^c of 5.32% captured using the Norton type model as shown in Tab. 3.5. Similarly, the minimum creep error e^c for DMN #2 using the plasticity-creep coupled model is 2.33%. Moreover, just the evaluation of the coupled plasticity-creep law lasts for more than eight hours as described in Tab. 3.5, whereas the training time along with the evaluation of the Norton model requires only slightly more than twelve hours. Thus, we save considerable computation time with only a slight loss of performance when using the Norton model.

To assess the generalization capabilities of the DMNs identified using the Norton error, we a-posteriori evaluate their performance on an inelastic *test* data set. The *test* data sets consist of the creep response evaluated using the fully coupled plasticity-creep law at three different directions of $15°, 45°$ and $60°$ with respect to the flow direction. Uniaxial stresses of 60.4 MPa, 60.0 MPa and 42.7 MPa were used for the $15°, 45°$ and $60°$ directions, respectively, for obtaining the creep strain response. The loading is performed in a similar manner as for the $30°$ direction outlined in Section 3.3.2. We extend the true creep error evaluated for $0°, 30°$ and $90°$ to these directions and the maximum relative errors for both DMNs are recorded in Tab. 3.6. The relative errors for all the test directions for DMN #1 are rather close with a maximum error of 3.79% in the $60°$ direction. The

DMN #	$e^c_{15^\circ}$	$e^c_{45^\circ}$	$e^c_{60^\circ}$
1	2.53%	3.74%	3.79%
2	3.84%	7.61%	3.08%

Table 3.6: Maximum relative errors for creep loading using *test* data with the DMNs identified using the inelastically informed offline training method adapted from Dey et al. [11, Tab. 6]

relative errors for DMN#2 vary by a factor of roughly two with a maximum of 7.61% in the 45° direction. It is interesting to note that a smaller inelastic Norton validation error does not necessarily lead to a smaller test creep error, as evident from Tab. 3.5 and Tab. 3.6. Although the errors in the test directions are not monitored during the inelastic validation, both DMNs are able to represent the a-posteriori creep loading in the test data with sufficient fidelity. Thus, we conclude that the novel early-stopping based training strategy serves as a low-cost methodology for reliably identifying the parameters of deep material networks suitable for creep loading.

Last but not least, we report on the performance of the DMNs, identified via the novel method, for predicting the creep response compared to high-fidelity simulations. For this purpose, we worked with DMN #2 from Tab. 3.5, and considered two different stress levels for each of the three directions from the *inelastic validation data set* and from the inelastic *test* data set. The results, shown in Fig. 3.8, reveal a close agreement between the DMN predictions and the full-field computations for the stress levels (shown in red) in the directions that the network was trained on. This comes as no surprise. By the way, it becomes apparent that for more than 10^4s, the 30° direction leads to inaccurate predictions. For the additional stress loading and the directions, which had not been monitored, the DMN closely matches the full-field predictions for strain levels below 1.5%. Actually, the agreement is quite remarkable. For higher effective strains, the agreement between DMN predictions and full-field simulation is worse. It remains to be studied whether this is caused by a lack of suitable training or results from insufficient material modeling. Indeed, for effective strains exceeding 1.5%, the local strains in the matrix exceed 5%. In particular, a material model at small strains appears questionable.

The runtimes of DMN and full-field simulations are compared in Tab. 3.7. The full-field simulations operate on a microstructure with 256^3 voxels. Moreover, the composite-voxel technique [131] is used. In contrast, the DMN is integrated on a single voxel. The

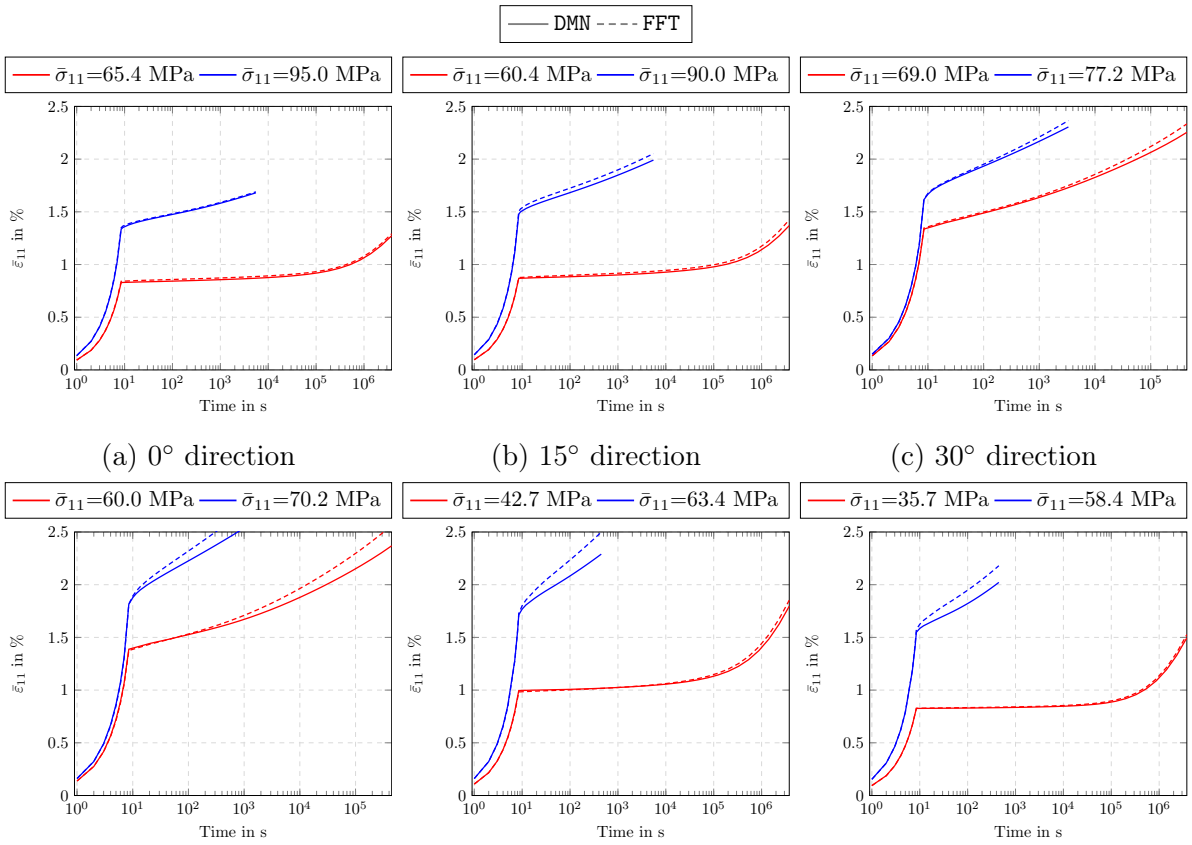

(a) 0° direction (b) 15° direction (c) 30° direction

(d) 45° direction (e) 60° direction (f) 90° direction

Figure 3.8: Comparison of FFT simulation results with DMN #2, adapted from Dey et al. [11, Fig. 8]

Direction	Stress level	FFT runtime	DMN runtime	Speed-up factor
0°	65.4 MPa	295 min	0.5 min	590
	95.0 MPa	348 min	0.5 min	696
15°	60.4 MPa	255 min	0.5 min	510
	90.0 MPa	425 min	0.5 min	850
30°	69.0 MPa	331 min	0.5 min	662
	77.0 MPa	310 min	0.5 min	620
45°	60.0 MPa	352 min	0.5 min	704
	70.2 MPa	343 min	0.5 min	686
60°	42.7 MPa	237 min	0.5 min	474
	63.4 MPa	290 min	0.5 min	580
90°	35.7 MPa	192 min	0.5 min	384
	58.4 MPa	236 min	0.5 min	472

Table 3.7: Runtime comparison between full-field results and deep material networks adapted from Dey et al. [11, Tab. 7]

full-field simulations take between 3.2 and 7.0 hours, whereas the DMN finishes after half a minute. Thus, we observe speed-up factors between slightly less than 400 up to almost 850. Thus, we confirm the startling speed-up factors reported by other authors [70, 72, 73].

3.4 Conclusion

Scientific progress consists of several phases. Initially, new territory gets explored and claimed. More often than not, these new islands of knowledge are established independently, lacking a proper connection to more established grounds. Moreover, the new territory needs to be charted and guarded.

We consider the introduction of deep material networks by Liu and coworkers [69, 70] as such a groundbreaking moment, which opened the eyes of the micromechanical community to the possibilities of the deep-learning technology. Indeed, finding accurate yet computationally tractable surrogate models of microstructures materials on component

scale for wide classes of industrially relevant materials has been an objective of micromechanics for a long time, and different strategies emerged, as discussed in the introduction. Several years have gone by, and the basic inner workings of DMNs were uncovered, and new variants of DMNs were proposed. The purpose of the work at hand was to critically review the concept of elasticity-based training of DMNs when a high degree of nonlinearity and rather larger time scales are involved. The available theory [71] is based on a perturbation argument around linear viscoelastic constitutive laws. In particular, it is conceivable that training based on linear elastic data alone might not be sufficient to prepare the DMN for the harsh conditions of creep loading. In this work, we provided (more or less explicit) examples of DMNs that fail to generalize from linear elasticity to creep. Due to a lack of a mathematical convergence theory for DMNs, it is not clear whether this is a defect of the linear elasticity-based training *per se* or a clever choice of sampled stiffnesses or appropriately designed loss functions may resolve this issue. Notwithstanding this lack of understanding from our side, we worked out a remedy for this shortcoming based on the early-stopping strategy which is classical in deep learning. We demonstrated that such an approach leads to reproducible and reliable training results for DMNs that may be used with confidence. The introduced technology serves as a low-cost alternative to inelastic training [73] and is expected to enter the standard toolbox of the deep material networker.

As already indicated, we consider the state of affairs surrounding the DMNs in the second, contemplating, phase following the initial exploration phase. The underpinnings of DMNs need to be understood more thoroughly, and guidelines for its use, including preferred tools, need to be identified.

4 Rapid inverse calibration of a multiscale model for the viscoplastic and creep behavior of short fiber-reinforced thermoplastics based on Deep Material Networks[1]

4.1 Introduction

We aim to characterize an industrially relevant semi-crystalline thermoplastic composite, reinforced with 30% by weight (17.8% by volume) E-glass fibers using a single set of experiments performed on the composite material. The characterization of the material response of such a complex SFRT involves the calibration of constitutive laws based on experimental results. Individual experiments need to be performed for both the constituents (pure matrix and fibers in our case) and the composite. To characterize the anisotropy of the mechanical response, experiments with samples cut from test plates with various orientations to the main flow direction need to be carried out as well. The resulting large

[1]This chapter is *based on* Sections 2, 4 and 5 of the publication A. P. Dey, F. Welschinger, M. Schneider, S. Gajek, and T. Böhlke, "Rapid inverse calibration of a multiscale model for the viscoplastic and creep behavior of short fiber-reinforced thermoplastics based on deep material networks," *International Journal of Plasticity*, vol. 160, p. 103484, 2023. The introduction has been condensed to eliminate redundancy with Chapter 1, and the notation has been standardized.

number of experiments is particularly costly for inelastic load cases like creep, where the experimental characterization may take months to be completed.

The classical *forward calibration* is based on identifying a suitable material model for the pure matrix and identifying the material parameters using experiments performed on the pure matrix while assuming a linear elastic constitutive law for the fibers. Subsequently, the model and the material parameters along with the spatially varying microstructure (obtained from μCT scans or process simulation) are used as an input for numerical homogenization techniques like efficient Fast Fourier Transform (FFT)-based approaches [44–47] or traditional finite element solvers for computational homogenization [144], for finding the material response of the composite. The inelastic composite response is compared to the composite experiments in different directions to account for the anisotropy. This current state of the art strategy, discussed in Section 4.2, often does not lead to favorable results since the process-induced changes in the matrix material such as fiber-induced [145] and flow-induced [146] crystallization is not accounted for.

To avoid setting up sophisticated physics-based models for the manufacturing process [147], an intuitive approach would be to identify the material parameters of the matrix from the composite experiments. This *inverse calibration* of the material model is hampered by the resource and time-intensive solution of the micromechanical problem, which consists of the constitutive law and the geometrical representation of the microstructure. The current state of the art homogenization techniques like the FFT-based approaches (although much faster than experimental calibration) may take several hours to run for complex material laws and microstructures. Thus, an *inverse calibration* using FFT-based approaches quickly becomes prohibitive, especially in the case of a large number of iterative runs.

The DMN framework introduced in Section 3.2, offers us an inexpensive yet reliable surrogate for solving the micromechanical problem. The trained DMN, in the online phase, predicts the material response for inelastic laws like elasto-plasticity [71] and creep [11] accurately, thus decoupling the geometric model from the constitutive response. The runtime of the DMN which is in the order of seconds enables us to perform the *inverse calibration* of complex constitutive material laws such as a fully coupled plasticity and creep law, see Section 4.2.3. Please note that once a DMN is trained, any constitutive law with an internal variable structure of GSM type can be assigned to the constituents, thus giving rise to a multiscale model for the effective composite response. This property makes the DMNs a convenient, general and flexible tool for the *inverse calibration* of a variety of materials used in composites when the microstructure is known and fixed.

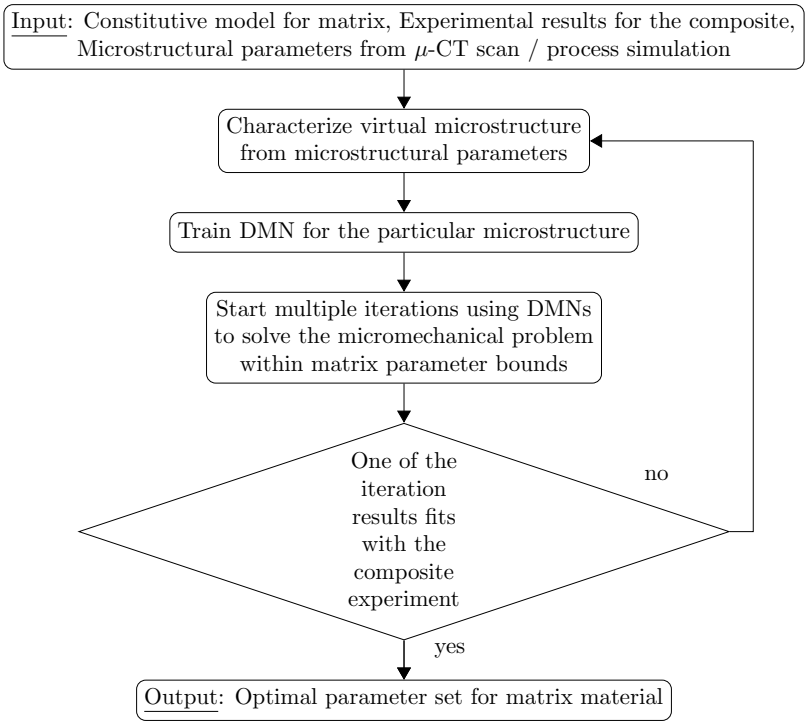

Figure 4.1: Flowchart for the *inverse calibration* of constitutive law for matrix adapted from Dey et al. [12, Fig. 1].

Since the DMN represents the spatially complex microstructure with remarkable accuracy [11, 71] a single set of composite experiments in a particular direction is sufficient for characterizing our constitutive law. Thus, the DMN framework not only makes the calibration of constitutive laws more accurate but also reduces the burden of performing a large number of experiments.

The *inverse calibration* workflow is depicted as a flowchart in Fig. 4.1. We wish to identify the material parameters for the constitutive model for the matrix. The constitutive model along with experiments performed on the composite and microstructural parameters for the spatially varying microstructure is taken as input. The first step is to identify a suitable virtual microstructure in the form of a representative volume element (RVE) from the microstructural parameters. Then we train a DMN to learn the spatial arrangement of the RVE. With the trained DMN at hand, we set up an optimization routine wherein the micromechanical problem is solved for a large number of iterations within the parameter bounds. The best fit of the DMN simulation with the composite experiments in a particular direction yields the optimal material parameters for the constitutive model of the

matrix. Furthermore, the optimal parameters can be used to generate virtual testing data of the composite in different directions using the DMN since the inherent anisotropy of the microstructure is encoded within the DMN framework. The *inverse calibration* workflow and the benefits of the proposed approach in comparison to the *forward calibration* workflow is investigated in Section 4.3.

4.2 Background for application to plasticity and creep of SFRTs

4.2.1 Microstructural investigations

In addition to the mechanical behavior of the individual phases which constitute the composite, a micromechanical investigation hinges on the spatial arrangement of these phases within the microstructure of the material. The composite behavior is strongly dependent on the fiber orientation and the fiber length distribution. As a result, micro-computed tomography (μCT) scans [148] are used to quantify the microstructure characteristics.
Micro-computed tomography is a non-destructive approach for acquiring 3D structural information of the microstructure in inhomogeneous materials. It is useful when the individual phases have strongly different absorption rates. We refer to Garcea et al. [126] for an in-depth discussion on the various features that can be derived by μCT analysis, its applicability for different loading circumstances, and the challenges that one might experience when completing the study.
We performed a high resolution μCT scan using a 30% by weight glass fiber reinforced semi-crystalline thermoplastic composite specimen milled out from a 120 mm $\times$ 80 mm $\times$ 2 mm injection molded plate. The μCT scan was performed on a region of interest (ROI) which encompasses a volume of 1.1 mm $\times$ 1.3 mm $\times$ 1.9 mm within the sample. We performed the μCT for one single region of interest. However, we followed the workflow laid down in a previous work by Hessman et al. [7], wherein multiple repeats of the μCT analysis were performed to characterize the microstructure of a fiber-reinforced polymer with sufficient accuracy. Therefore, we are confident that the μCT scan can accurately represent the spatial arrangement of the fibers in the microstructure. The results from the scan are shown in Fig. 1.1. In a further step we extracted the structural information

from the volume images. We adopted a voxel-based approach where calculations were performed per layer, with the fibers assigned to the layers. Then microstructure information for each layer is extracted from high-resolution volume photographs of the material [149]. The method of separating two or more materials from each other based on their gray values is known as segmentation. To segment 3D μCT image data, the commercial software ScanIP [150] is used. It takes image portions from the fiber mask that are too small to be considered fibers and subtracts them. The fibers in contact are also separated by identifying and removing the interface voxels. The second and fourth order fiber orientation tensor, length-weighted mean fiber length and volume fraction were computed using microstructure segmentation from ScanIP [150]. The length-weighted mean fiber length for our microstructure evaluated using the segmentation algorithm is 286.4 μm with a standard deviation of 131.9 μm. Since the accuracy of the segmentation-based evaluation of the fiber diameter is limited, the fiber diameter was estimated to be 10 μm. The average second order and fourth order fiber orientation tensors (FOT) in each of the five layers, having approximately equal height, over the thickness of the sample and the mean using a single layer over the thickness are given in Tab. 4.1 and 4.2, respectively.

Layer #	A_{11}	A_{22}	A_{33}	A_{23}	A_{13}	A_{12}
1	0.13	0.86	0.01	-0.01	0	-0.02
2	0.13	0.85	0.01	-0.01	0	0
3	0.53	0.44	0.02	0	0.01	0.06
4	0.14	0.84	0.02	0	0	0
5	0.12	0.87	0.01	0	0	-0.01
Mean	0.21	0.77	0.02	0	0	0.01

Table 4.1: Average second order fiber orientation tensor over thickness for the composite microstructure adapted from Dey et al. [12, Tab. 1].

Layer #	A_{1111}	A_{1122}	A_{1133}	A_{1123}	A_{1113}	A_{1112}	A_{2222}	A_{2233}	A_{2223}	A_{2213}	A_{2212}	A_{3333}	A_{3323}	A_{3313}	A_{3312}
1	0.07	0.06	0	0	0	-0.01	0.79	0.01	-0.01	0	-0.01	0	0	0	0
2	0.07	0.06	0.01	0	0	0	0.78	0.01	-0.01	0	0	0.01	0	0	0
3	0.41	0.10	0.01	0	0.01	0.04	0.34	0.01	0	0	0.02	0.01	0	0	0
4	0.08	0.06	0.01	0	0	0	0.77	0.01	0	0	0	0.01	0	0	0
5	0.06	0.06	0	0	0	0.00	0.81	0.01	0	0	-0.01	0	0	0	0
Mean	0.14	0.07	0.01	0	0	0.01	0.69	0.01	-0.01	0	0	0.01	0	0	0

Table 4.2: Average fourth order fiber orientation tensor over thickness for the composite microstructure adapted from Dey et al. [12, Tab. 2].

4.2.2 Experimental investigations

Pure matrix

Several experimental investigations were performed at Robert Bosch GmbH with the help of a dog-bone shaped Becker sample [118] as shown in Fig. 4.2. The experiments were done on the unreinforced matrix with the aim of identifying the parameters of the material model of the matrix and use them for the composite response in the classical *forward calibration* technique. In this work, we perform the *forward calibration* of the material model to compare the results with the novel *inverse calibration* using DMNs in Section 4.3.5.

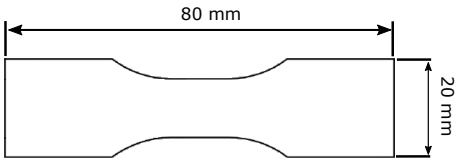

Figure 4.2: Becker sample [118] adapted from Dey et al. [12, Fig. 3].

The anisotropy in the unreinforced polymer matrix is small enough that using an isotropic material model is sufficient. Hence the direction in which the loads are applied does not play any role in the mechanical response. Firstly, we performed monotonic loading of the specimen up to 5% strain for four different samples to characterize the elasto-plastic behavior, see Fig. 4.3(a). We observe a steady increase of stress with increasing strain

up to the plasticity limit where we see a gradual saturation of the stress with a slight softening at the end.

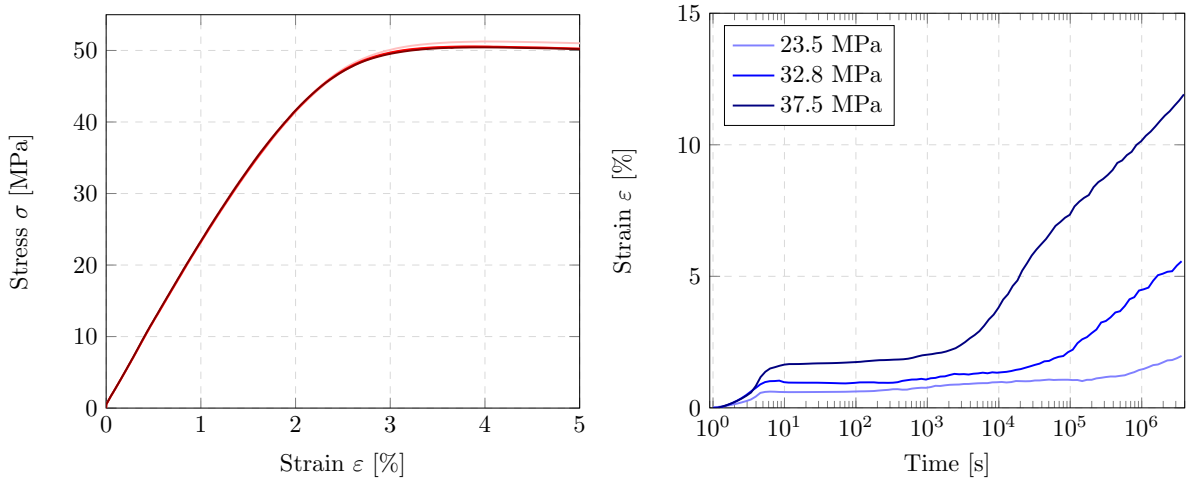

(a) Monotonic loading

(b) Creep at different stress levels

Figure 4.3: Experimental results for unreinforced matrix adapted from Dey et al. [12, Fig. 4].

Furthermore, to characterize the long-term creep loading behavior, we performed experiments on the unreinforced matrix at three load levels 23.5 MPa, 32.8 MPa, and 37.5 MPa. The experiments were load-controlled and the load was ramped up to the respective stress levels in 8.5 s and then held constant for different time intervals depending on the load level. The experimental results are shown in Fig. 4.3(b). Three creep phases are typically observed [77]. In the primary creep stage, the creep-strain rate begins with a high value and decreases to a nearly constant value in the secondary creep stage. The creep strain rate increases throughout the tertiary phase, eventually resulting in specimen breakage [78]. For all three load levels taken into consideration, the first stage concludes at about the same time. However, for the three load levels, the beginning of the third stage and the inclination of the strain at start are rather different.

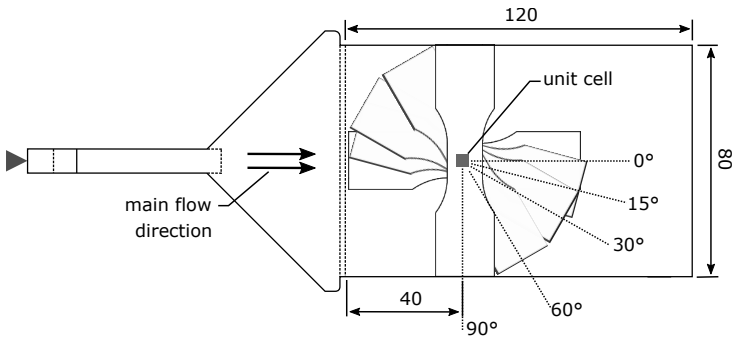

Figure 4.4: Prepared Becker [118] samples from composite plates with different directions adapted from Dey et al. [12, Fig. 5].

Composite

The fibers dispersed in the matrix material render the plasticity and creep response of the composite strongly anisotropic. Thus, to account for the anisotropy, the experimental analysis was performed using samples cut out from an injection molded plate in specific angles with respect to the main flow direction as shown in Fig. 4.4. The monotonic loading of the samples at different strain levels cut out from the injection molded plate at angles of 0°, 15°, 30°, 60° and 90° were performed, see Fig. 4.5. The elasto-plastic response of the composite is qualitatively similar to that of the pure matrix. The 0° direction shows the stiffest response as a result of maximum number of fibers oriented in the direction of loading. The material response becomes progressively softer as we move from 0° to 90° direction as illustrated in Fig. 4.5.

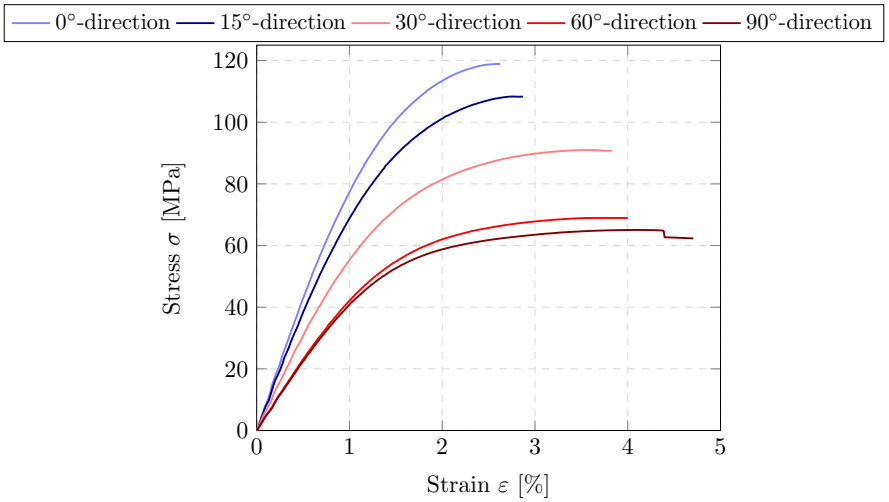

Figure 4.5: Experimental results under monotonic loading at different directions for the composite adapted from Dey et al. [12, Fig. 6].

The load-controlled experiments for evaluating the creep response of the composite were performed using samples milled from the injection molded plate at 0°, 30° and 90° directions only, since the creep experiments are time and resource consuming. Three different stress levels were applied in each direction for the evolution of creep in the material and for each stress level several samples were tested. The observed mean creep strain is plotted against the logarithmic time scale in Fig. 4.6 since, at higher load levels, the experimental time is significantly shorter.

In the 0° direction, most of the fibers are aligned in the direction of loading and hence the maximum load is carried by the fibers. So, the maximum loads are applied in this direction and consequently it has the highest resistance to creep compared to the 30° and 90° directions, see Fig. 4.6(a). In the 30° direction the load is partially carried by the fibers. This leads to higher creep strains at smaller loads as evident from Fig. 4.6(b). Finally, in the 90° direction the majority of the load is carried by the matrix material. Hence the highest creep strains were observed at the lowest loads, see Fig. 4.6(c).

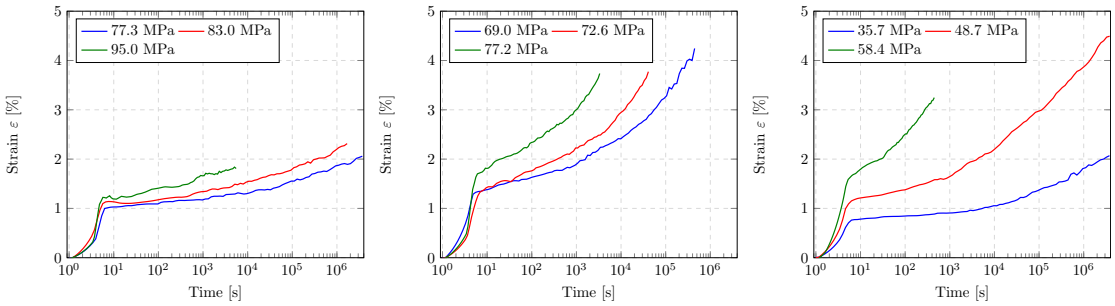

(a) 0°-direction (b) 30°-direction (c) 90°-direction

Figure 4.6: Experimental results under creep loading at different directions for the composite adapted from Dey et al. [12, Fig. 7].

4.2.3 Coupled plasticity and creep law

Motivation

For the material modeling of plasticity and creep in SFRTs, the fibers and the matrix are assigned separate constitutive material models. The glass fibers are modeled as linear elastic and the material parameters are obtained from Doghri et al. [121] and defined in Table 4.3. On the other hand, the matrix undergoes both plastic deformation on a short time scale and creep deformations on a long time scale. Consequently, a fully coupled plasticity and creep law is required for modeling the mechanical behavior. The plasticity model accounts for inelastic strains during the load ramp-up for the first 8.5 s. The creep model captures the inelastic strain during long-term loading. Since we observe maximum creep strains of slightly above 4% in Fig. 4.6 for the composite, we consider a constitutive law for the matrix material in the small strain, i.e., geometrically linear framework.
The model is formulated in the generalized standard material (GSM) [101] setting where the thermodynamic consistency is a consequence of the convexity of the potentials. The GSM framework is also convenient for concurrent multiscale modeling, e.g., in the context of DMNs [72].

Basic kinematics and state variables

Aiming at a continuum mechanical description of creep processes in unreinforced thermoplastic materials, a combined J_2 plasticity with isotropic exponential linear hardening [151] and a creep model with stress power and strain hardening exponential law [152] is envisaged. The creep part in the model accounts for both the primary and the secondary stage of creep. The primary creep stage is modeled by an exponential strain hardening term whereas the secondary creep stage is captured with a combined power law and linear term [153]. Within a small deformation setting, in addition to the macroscopic displacement field $\boldsymbol{u}$, a variable α is introduced to describe the isotropic hardening process on a phenomenological level. The macroscopic strain tensor, defined as the symmetric part of the displacement gradient, $\boldsymbol{\varepsilon} = \nabla_s \boldsymbol{u}$ is decomposed

$$\boldsymbol{\varepsilon} = \boldsymbol{\varepsilon}^{\mathrm{e}} + \boldsymbol{\varepsilon}^{\mathrm{p}} + \boldsymbol{\varepsilon}^{\mathrm{c}} \tag{4.2.1}$$

into an elastic part $\boldsymbol{\varepsilon}^{\mathrm{e}}$ which quantifies reversible deformations and inelastic parts $\boldsymbol{\varepsilon}^{\mathrm{p}}$ (plastic strain) and $\boldsymbol{\varepsilon}^{\mathrm{c}}$ (creep strain) which describe the permanent deformation of the material that remains upon unloading.

Energy storage mechanisms, stresses, and driving forces

The free energy density ψ for the plasticity and creep model

$$\begin{aligned} \psi(\boldsymbol{\varepsilon}, \alpha, \boldsymbol{\varepsilon}^{\mathrm{p}}, \boldsymbol{\varepsilon}^{\mathrm{c}}) \quad &= \frac{1}{2}\kappa \operatorname{tr}^2[\boldsymbol{\varepsilon}] + \mu \left\| \mathtt{dev}[\boldsymbol{\varepsilon} - \boldsymbol{\varepsilon}^{\mathrm{p}} - \boldsymbol{\varepsilon}^{\mathrm{c}}] \right\|^2 \\ &\quad + \frac{1}{2} h \alpha^2 + (y_\infty - y_0) \left[\alpha + \frac{1}{\omega} (\mathtt{exp}[-\omega\alpha] - 1) \right] \end{aligned} \tag{4.2.2}$$

is defined in terms of the bulk modulus κ, the shear modulus μ, the linear hardening modulus h, the initial yield stress y_0, the saturation yield stress y_∞ and the hardening parameter ω. The elastic constants are related to the Young's modulus E and Poisson's ratio ν via

$$\kappa = \frac{E}{3\,(1-2\nu)} \quad \text{and} \quad \mu = \frac{E}{2\,(1+\nu)}. \tag{4.2.3}$$

The stresses and driving forces compute as

$$\begin{aligned}
\boldsymbol{\sigma} &= \partial_{\boldsymbol{\varepsilon}}\psi &&= \kappa\,\mathrm{tr}[\boldsymbol{\varepsilon}]\boldsymbol{1} + 2\mu\,\mathtt{dev}[\boldsymbol{\varepsilon} - \boldsymbol{\varepsilon}^{\mathrm{p}} - \boldsymbol{\varepsilon}^{\mathrm{c}}],\\
\beta^{\mathrm{p}} &= \partial_{\alpha}\psi &&= -h\alpha - (y_{\infty} - y_0)(1 - \mathtt{exp}[-\omega\alpha]),\\
\boldsymbol{B}^{\mathrm{p}} &= \partial_{\boldsymbol{\varepsilon}^{\mathrm{p}}}\psi &&= 2\mu\,\mathtt{dev}[\boldsymbol{\varepsilon} - \boldsymbol{\varepsilon}^{\mathrm{p}} - \boldsymbol{\varepsilon}^{\mathrm{c}}],\\
\boldsymbol{B}^{\mathrm{c}} &= \partial_{\boldsymbol{\varepsilon}^{\mathrm{c}}}\psi &&= 2\mu\,\mathtt{dev}[\boldsymbol{\varepsilon} - \boldsymbol{\varepsilon}^{\mathrm{p}} - \boldsymbol{\varepsilon}^{\mathrm{c}}].
\end{aligned} \tag{4.2.4}$$

Dissipation potential

Following the GSM framework, it remains to specify the dissipation potential ϕ. For the coupled plasticity and creep model the dissipation potential is split into plastic and creep parts via

$$\phi(\dot{\alpha}, \dot{\boldsymbol{\varepsilon}}^{\mathrm{p}}, \dot{\boldsymbol{\varepsilon}}^{\mathrm{c}}; \alpha, \boldsymbol{\varepsilon}^{\mathrm{p}}, \boldsymbol{\varepsilon}^{\mathrm{c}}) = \phi^{\mathrm{p}}(\dot{\alpha}, \dot{\boldsymbol{\varepsilon}}^{\mathrm{p}}; \alpha, \boldsymbol{\varepsilon}^{\mathrm{p}}) + \phi^{\mathrm{c}}(\dot{\boldsymbol{\varepsilon}}^{\mathrm{c}}; \boldsymbol{\varepsilon}^{\mathrm{c}}). \tag{4.2.5}$$

In a rate-dependent setting with a viscosity of η, the dissipation function for viscoplasticity [151] is defined by

$$\phi^{\mathrm{p}}(\dot{\alpha}, \dot{\boldsymbol{\varepsilon}}^{\mathrm{p}}; \alpha, \boldsymbol{\varepsilon}^{\mathrm{p}}) = \sup_{\boldsymbol{B}^{\mathrm{p}}, \beta^{\mathrm{p}}} \left[\boldsymbol{B}^{\mathrm{p}} : \dot{\boldsymbol{\varepsilon}}^{\mathrm{p}} + \beta^{\mathrm{p}}\dot{\alpha} - \frac{1}{2\eta}\langle \varphi(\boldsymbol{B}^{\mathrm{p}}, \beta^{\mathrm{p}})\rangle_{+}^{2} \right]. \tag{4.2.6}$$

Regarding plasticity, the elastic domain is bounded by the yield function which combines a linear hardening with a Voce-type hardening (4.2.4)

$$\varphi(\boldsymbol{B}^{\mathrm{p}}, \beta^{\mathrm{p}}) = \|\mathtt{dev}[\boldsymbol{B}^{\mathrm{p}}]\| - \sqrt{2/3}(y_0 - \beta^{\mathrm{p}}). \tag{4.2.7}$$

The necessary condition for the variational principle (4.2.6) gives the evolution equation for the plastic strain

$$\dot{\boldsymbol{\varepsilon}}^{\mathrm{p}} = \frac{1}{\eta}\langle \varphi(\boldsymbol{B}^{\mathrm{p}}, \beta^{\mathrm{p}})\rangle_{+}\vec{\boldsymbol{n}} \tag{4.2.8}$$

and for the hardening variable

$$\dot{\alpha} = \frac{1}{\eta}\langle \varphi(\boldsymbol{B}^{\mathrm{p}}, \beta^{\mathrm{p}})\rangle_{+}\sqrt{2/3}, \tag{4.2.9}$$

where we used the expressions (4.2.4) for the driving forces. For the inelastic strains, the flow direction is given by

$$\vec{\boldsymbol{n}} := \frac{\mathtt{dev}[\boldsymbol{\sigma}]}{\|\mathtt{dev}[\boldsymbol{\sigma}]\|}, \tag{4.2.10}$$

which accounts for the plastic strain and creep strain evolution both in deviatoric direction.

Regarding creep the dissipation potential reads

$$\phi^{\mathrm{c}}(\dot{\boldsymbol{\varepsilon}}^{\mathrm{c}};\boldsymbol{\varepsilon}^{\mathrm{c}}) = \sup_{\boldsymbol{B}^{\mathrm{c}}} \Bigg[\boldsymbol{B}^{\mathrm{c}} : \dot{\boldsymbol{\varepsilon}}^{\mathrm{c}} - \dot{\varepsilon}_0 (1 + C \exp[-\varepsilon^{\mathrm{c}}/k]) \cdot \left(\frac{(A_1\sqrt{3/2}\|\mathtt{dev}[\boldsymbol{B}^{\mathrm{c}}]\|)^{n_c+1}}{(n_c+1)A_1\sqrt{3/2}} + \frac{(A_2\sqrt{3/2}\|\mathtt{dev}[\boldsymbol{B}^{\mathrm{c}}]\|)^2}{2A_2\sqrt{3/2}} \right) \Bigg] \tag{4.2.11}$$

in terms of the creep constants C and k, the pre-factors A_1 and A_2, a reference creep rate $\dot{\varepsilon}_0$ and the creep exponent n_c. In the dissipation potential (4.2.11), in addition to the classical power law term, we also included a linear term to better represent the creep behavior at lower loads, see Gorash et al. [153]. The necessary condition for the variational principle (4.2.11) and using the driving force from (4.2.4) gives the evolution equation for the creep strain

$$\dot{\boldsymbol{\varepsilon}}^{\mathrm{c}} = \dot{\varepsilon}_0 \left[1 + C \exp[-\varepsilon^{\mathrm{c}}/k]\right] \left[(A_1\sqrt{3/2}\|\mathtt{dev}[\boldsymbol{B}^{\mathrm{c}}]\|)^{n_c} + (A_2\sqrt{3/2}\|\mathtt{dev}[\boldsymbol{B}^{\mathrm{c}}]\|) \right] \vec{\boldsymbol{n}}. \tag{4.2.12}$$

On the algorithmic side the constitutive equations (4.2.8), (4.2.9) and (4.2.12) are solved in an implicit, time-discrete setting using a classical return-mapping algorithm based on a creep-plastic predictor and a plastic corrector step. The model is implemented as a user-defined material subroutine (UMAT) in Abaqus [120]. It can be used without any modification in the FFT-based solver FeelMath [133] and in the DMN framework.

4.2.4 Forward calibration of the constitutive law

Framework

With the material model described in Section 4.2.3 at hand, we need to identify the material parameters using the experimental results described in Section 4.2.2. Following the discussion in Section 4.1, due to the complexity of solving the full micromechanical problem for the composite, both in terms of runtime and resources, the forward approach identifies the material parameters of the matrix from experiments performed on the pure polymer matrix as shown in Fig. 4.3.

Since the two inelastic processes under focus take place at different time scales, i.e.,

plasticity at a short and creep at a long time scale, an incremental two-step parameter identification workflow is applied for the polymer matrix. In a first step, with deactivated evolution of the creep strains, all elastic constants and all plasticity parameters are determined from uni-axial tensile experiments. In a second step of this incremental parameter identification workflow, with frozen elasticity and plasticity coefficients, the remaining creep parameters are identified from long-term creep tests carried out at different load levels.

Identification of elasticity and plasticity coefficients

First, the identification of the elasticity and plasticity parameters is done based on experimental results, see Fig. 4.3(a). For the optimization workflow, a single element unit cube simulation model is set up in Abaqus [120] which is iteratively called in an OptiSlang [119] procedure. To identify the material parameters, a minimization problem is set up which minimizes the sum over the load steps of the root mean square deviation between each of the experimental curves and the simulation results. During the optimization, we fix the Poisson's ration to $\nu = 0.4$ and the viscosity to $\eta = 0.001$ MPa $\cdot$ s, emulating strain-rate independence.
The algorithm used is the Adaptive Metamodel of Optimal Prognosis (AMOP) [154]. 300 samples of parameters were generated using the Latin Hypercube Sampling (LHS) method [155] and the best fitting parameters with respect to the experimental results, obtained after the optimization using AMOP algorithm, are recorded in Table 4.3. The total sum of the root mean square deviation between each of the experimental curves and the simulation results with the best fitting parameters is 1.98. The plot comparing the experimental results and the unit cube simulation with the best fitting parameters is shown in Fig. 4.7(a). The plasticity and creep coupled law accurately represents the plastic deformation at smaller time scales before the onset of creep.

Identification of creep coefficients

A similar approach is adopted for the identification of the remaining creep parameters. The optimization for the creep parameters was also performed in OptiSLang [119] while

keeping the already identified elasticity and plasticity parameters fixed. The creep experiments on the unreinforced matrix were performed at three different load levels, see Section 4.2.2. We aim to find a set of creep parameters which describes the deformation behavior at all three stress levels. Therefore, we consider an objective function that accounts for all load levels. The global objective function f_{global} is defined as

$$f_{global} = \min_{s\in\{1,..,300\}} \left(\sum_{i=1}^{n_{\text{Stresses}}} f^{s}_{local,i} \right), \tag{4.2.13}$$

where i represents one of the load levels, s denotes the 300 samples of parameters generated using LHS [155], $n_{\text{Stresses}} = 3$ denotes the number of load levels and

$$f_{local,i} = \left[\frac{\text{abs}(\text{area}(\varepsilon_i^{exp} - \varepsilon_i^{sim}))}{\max_{n_p}(\varepsilon_{i,n_p}^{exp}) \times \max_{n_p}(t_{i,n_p}^{exp})} \right]. \tag{4.2.14}$$

To remove the scaling effects, the local objective function $f_{local,i}$ is normalized by the maximum strain and maximum time within the entire experimental procedure containing n_p recorded data points at every load level. The parameter reference creep rate $\dot{\varepsilon}_0$ is added to the model to preserve the consistency of units and is fixed to 1.0 s^{-1} during the optimization.

Similar to the plasticity case, we utilize AMOP [154] with a previously set up Abaqus-based [120] unit-cube simulation. 300 samples of parameters were generated, and the parameter set with the minimum value of the global objective function is given in Table 4.3. The experimental creep curves at the different load levels are plotted against the simulation using the best parameters, shown in Figure 4.7(b) in the log time scale. A high fitting quality is observed for the considered range of stresses. More precisely the relative deviation between the experimental values and the simulation using best fitting parameters of all the stress levels is below 3%.

With the material parameters identified using the *forward calibration* workflow at hand, we can directly use it as an input for finding the composite response using homogenization techniques such as FFT simulations. However, we still require a representative virtual microstructure of the composite material which outlines the spatial arrangement of the fibers in the matrix. In the following sections, we discuss the DMN framework and identify a representative microstructure for training the DMN. The DMN framework is then integrated in the *inverse calibration* workflow to identify the material parameters of the matrix. Finally, in Section 4.3.5, we use the representative microstructure to compare

the performance of the *forward calibration* using FFT simulations with respect to the DMN-based *inverse calibration*.

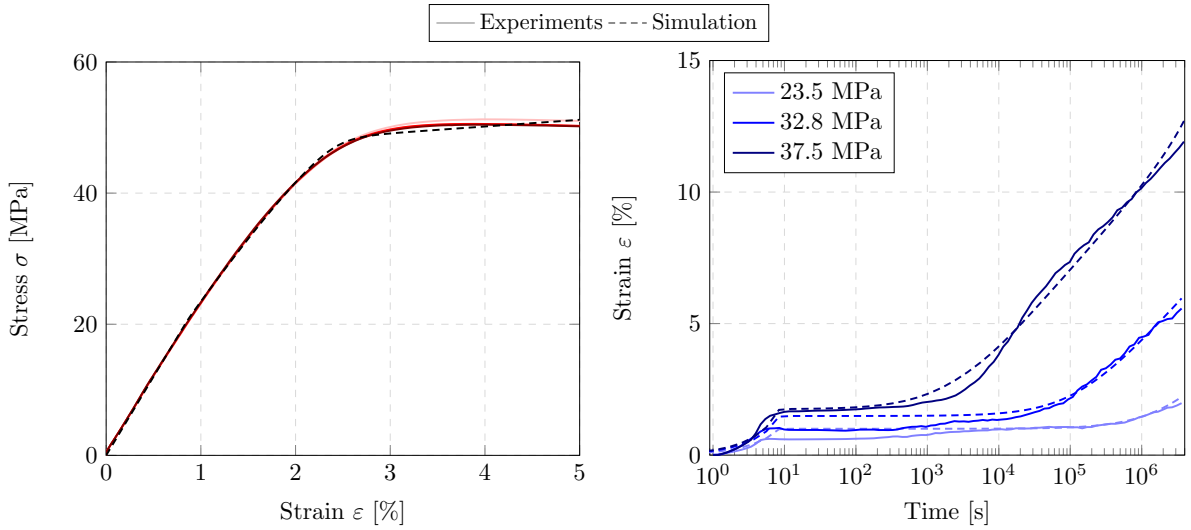

(a) Elasto-plastic parameters

(b) Creep parameters

Figure 4.7: Experimental results compared to simulation results using best parameter set adapted from Dey et al. [12, Fig. 8].

Matrix	Elastic	$E = 2399.3$ MPa	$\nu = 0.4$	
	Plastic	$h = 346.9$ MPa	$\omega = 384.9$	$y_0 = 20.9$ MPa
		$y_\infty = 51.9$ MPa		
	Creep	$A_1 = 0.014$ 1/MPa	$n_c = 32.4$	$A_2 = 1.5 \times 10^{-13}$ 1/MPa
		$C = 1870.1$	$k = 0.016$	$\dot{\varepsilon}_0 = 1.0$ s^{-1}
Fibers	Elastic	$E = 72\,000$ MPa	$\nu = 0.22$	

Table 4.3: Material parameters for composite material - Matrix parameters obtained from *forward calibration* of constitutive law adapted from Dey et al. [12, Tab. 3].

4.3 Towards reducing the experimental effort

4.3.1 On the influence of the microstructure

Framework

As stated in Section 4.1, the micromechanical problem involves the constitutive laws of the constituents (fiber and matrix) as well as the spatial arrangement of the fibers in the matrix material. To this effect, the material response of the composite hinges on the representative microstructure of the material involved. There are several factors such as the fiber orientation and fiber length which heavily influence the material response. In this section, we take a look at the influence of some of these factors on the linear elastic response of the composite. Although the microstructural arrangement influences the inelastic composite response, we investigate the involved factors using the elastic response since the inelastic response for a wide variety of microstructures would be extremely time-consuming to compute using state of the art homogenization techniques like FFT simulations. Furthermore, we would also require fixed inelastic material parameters that can emulate the experimental results with a high fidelity, which is not yet available. We used the microstructural parameters reported in Section 4.2.1 to reconstruct digital microstructures using the SAM algorithm [127]. We generated several cubic unit cells with an edge length of 625 μm containing cylindrical fibers having a length of 286.4 μm and a diameter of 10 μm with a minimum distance of 3 μm between the fibers.

We investigate the elastic response of the virtual microstructures with the help of the FFT-based computational homogenization software FeelMath [133]. We use the staggered grid discretization [47, 134] and the linear conjugate gradient method [135–137] to compute the anisotropic linear elastic stiffness matrix of the composite. We take as our input the Young's modulus $E = 2292$ MPa and a Poisson's ratio $\nu = 0.4$ for the pure matrix material obtained from experimental analysis performed at Robert Bosch GmbH. Standard parameters [121] defined in Table 4.3 are used for the E-glass fibers. The microstructures are discretized with 512^3 voxels, each voxel having an edge length of 1.22 μm. Each microstructure is further resampled with a factor of two to 256^3 voxels using the composite voxel technique [130–132] to accelerate the FFT computation with high fidelity, see Dey et al. [11, § 3.1].

Furthermore, the experimental analysis of the Young's modulus E in different directions

were available at Robert Bosch GmbH, performed using a Becker sample [118] shown in Fig. 4.2, cut out from an injection molded plate at angles 0°, 30°, 60° and 90° with respect to the flow direction, see Fig. 4.4. The Becker samples were subjected to monotonic loading up to strains of 0.05% and 0.25%. The stress response at these strains is then used to calculate the Young's modulus. Five samples are tested for each direction and the mean Young's modulus for each direction is listed in Table 4.4.

Loading angle	0°	30°	60°	90°
Young's modulus E	8664.77 MPa	6181.28 MPa	4713.02 MPa	4603.03 MPa

Table 4.4: Experimentally determined mean Young's moduli at different loading angles for the composite adapted from Dey et al. [12, Tab. 4].

The elastic moduli at the different loading angles are also extracted from the anisotropic stiffness matrix obtained from the FFT-simulation and compared with the experimental analysis. For each loading angle we define the relative error

$$e_\theta^E = \frac{|E_\theta^{\mathtt{exp}} - E_\theta^{\mathtt{FFT}}|}{|E_\theta^{\mathtt{exp}}|} \quad \text{for} \quad \theta = 0^\circ, 30^\circ, 60^\circ, 90^\circ, \tag{4.3.1}$$

to compare the deviation of the elastic response of the virtual microstructure with respect to the experimental analysis. For visualization, we rely upon the method introduced by Böhlke and Brüggemann [156].

On the influence of the closure approximation

The reconstruction of the digital microstructure using the SAM algorithm [127] requires the fourth-order fiber orientation tensor to be prescribed. It is possible to use the fourth-order tensor for generating the virtual microstructure, given in Table 4.2, directly. Nevertheless, we aim for a complete virtual characterization of the composite starting from the simulation of the injection molding process to find the microstructural parameters and to use them for further evaluation of the material response. The current existing macroscopic models for predicting the fiber orientation tensor generate only the second-order fiber orientation tensor as an output. For a review of existing macroscopic fiber orientation models, we refer to Kugler et al. [157].
Therefore, as an alternative we use closure approximations to estimate the fourth-order

tensor from the second order-tensor. We generated three virtual microstructures, the first one prescribed with the average fourth-order tensor obtained from the segmentation algorithm using a single layer over the thickness, see Table 4.2. The second and third microstructures were prescribed with the second-order mean fiber orientation tensor given in Table 4.1, combined with the maximum entropy closure [158] and the exact closure approximation [128, 129] respectively. The numerical results obtained for the three microstructures from the FFT-based computational homogenization are visualized in Fig. 4.8 using the method described in Böhlke-Brüggemann [156]. The experimental results in the 0°, 30°, 60° and 90° directions with respect to the flow direction are also plotted in Fig. 4.8. The relative errors at these directions and the number of fibers required to represent the respective FOTs are given in Table 4.5.

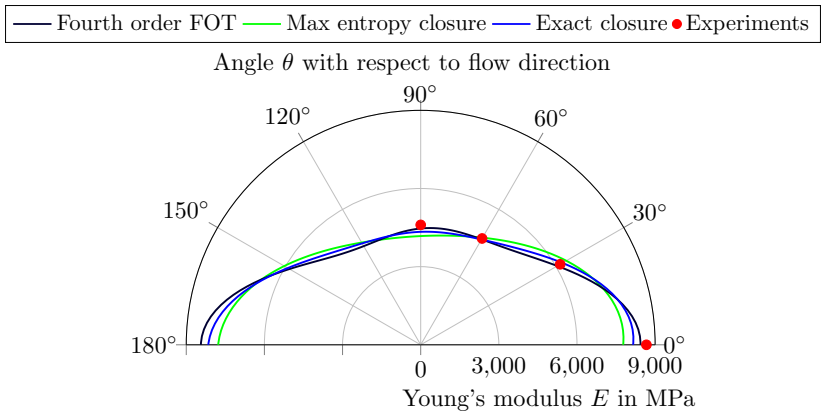

Figure 4.8: Effective Young's modulus for the microstructures with fourth-order and second-order FOT compared to experimental results adapted from Dey et al. [12, Fig. 10].

We observe that the fourth order fiber orientation tensor conveys a stiffer response and shows a better relative error when compared to the experimental stiffnesses, especially in the 0° and 90° directions. The exact closure approximation shows a slightly softer response when compared to experimental results, whereas the maximum entropy closure shows the highest deviation from experimental results in the 0°, 30° and 90° directions. Therefore, it is apparent that the use of closure approximations results in the loss of information about the spatial arrangement of the fibers in the matrix material. Note that the microstructure generation algorithm uses the same number of fibers to represent the

different FOTs in the unit cells, as the fiber count is fixed by the fiber-volume content, the fiber aspect ratio and the volume of the considered cell.

Closure approximation	Fiber count	$e^E_{0^\circ}$	$e^E_{30^\circ}$	$e^E_{60^\circ}$	$e^E_{90^\circ}$
No closure	1932	2.78%	2.06%	0.73%	2.63%
Max entropy	1932	10.27%	4.42%	0.75%	9.31%
Exact closure	1932	5.87%	1.68%	0.96%	5.77%

Table 4.5: Relative error of Young's modulus of microstructures with varying FOT compared to experimental Young's modulus adapted from Dey et al. [12, Tab. 5].

On the influence of the fiber length

In addition to investigating the effect of the spatial distribution of the fibers, we also investigate the effect of the fiber length on the elastic stiffness of the composite. The segmentation algorithm yields the length-weighted mean fiber length of 286.4 μm with a standard deviation (SD) of 131.9 μm. We prescribed the fourth-order fiber orientation tensor to generate virtual microstructures with similar parameters as in Section 4.3.1 but with varying fiber lengths.

We generated five microstructures starting with the fiber lengths outlined in Table 4.6. After the linear elastic FFT computations and post-processing the data as in Section 4.3.1, the results are visualized in Fig. 4.9. The number of fibers in each unit cell and the relative error compared to experimental results is given in Table 4.6.

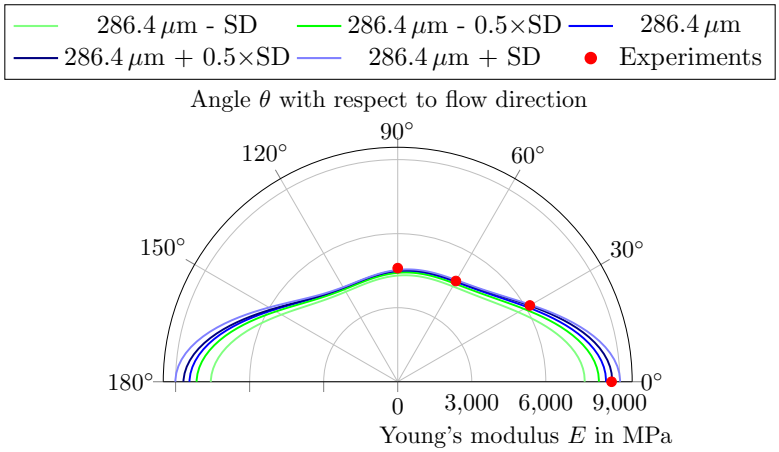

Figure 4.9: Effective Young's modulus for the microstructures with varying fiber lengths compared to experimental results adapted from Dey et al. [12, Fig. 11].

Fiber length	Fiber count	$e^E_{0°}$	$e^E_{30°}$	$e^E_{60°}$	$e^E_{90°}$
286.4 μm - SD	3581	12.56%	8.77%	5.29%	6.53%
286.4 μm - 0.5×SD	2510	5.92%	4.45%	2.44%	4.14%
286.4 μm	1932	2.78%	2.06%	0.73%	2.63%
286.4 μm + 0.5×SD	1570	0.23%	0.14%	0.21%	2.18%
286.4 μm + SD	1323	3.99%	0.76%	0.85%	1.56%

Table 4.6: Relative error of Young's modulus of microstructures with varying fiber lengths compared to experimental Young's modulus adapted from Dey et al. [12, Tab. 6].

The composite exhibits a gradually stiffer response with increasing fiber length. This stiffer response is more pronounced in the 0° direction since most fibers are oriented in this direction, see Fig. 4.9. The relative error of the elastic stiffness decreases as we increase the fiber length from 286.4 μm - SD and gives us the best relative error in all directions at a fiber length of 286.4 μm + 0.5×SD, see Table 4.6. Thereafter, the errors start to increase with increasing fiber length. The relative error in the 0° direction varies roughly by a factor of three. The fiber length also influences the number of fibers included in the unit cell. More precisely, we observe a decreasing fiber count with increase in fiber length, see Table 4.6.

On the influence of the layer-wise FOT

The segmentation algorithm applied on the μCT scan image generates not only the layer-wise second-order FOT (outlined in Table 4.1) but also the layer-wise fourth-order FOT (outlined in Table 4.2). The FOT varies across the thickness due to varying flow fields in the shell and core region during the injection molding process. Therefore, the mean FOT over the thickness might not be sufficient to represent the complete information of the spatial arrangement of the fibers. We evaluate the efficiency of the layer-wise FOT by generating two additional microstructures with the same parameters outlined in Section 4.3.1 but prescribing the layer-wise FOT on five layers having equal height over the thickness of the virtual microstructure. One of the microstructures is prescribed with the full fourth-order FOT in each of the five layers from Table 4.2 and the other with the second order FOT described in Table 4.1 using exact closure approximations [128, 129] in each of the five layers. Furthermore, we compare it with the microstructure generated using the mean fourth-order FOT applied on a single layer, see Section 4.3.1. The results are visualized in Fig. 4.10 and the relative error with respect to the experimental results along with the number of fibers included in each unit cell is given in Table 4.7.

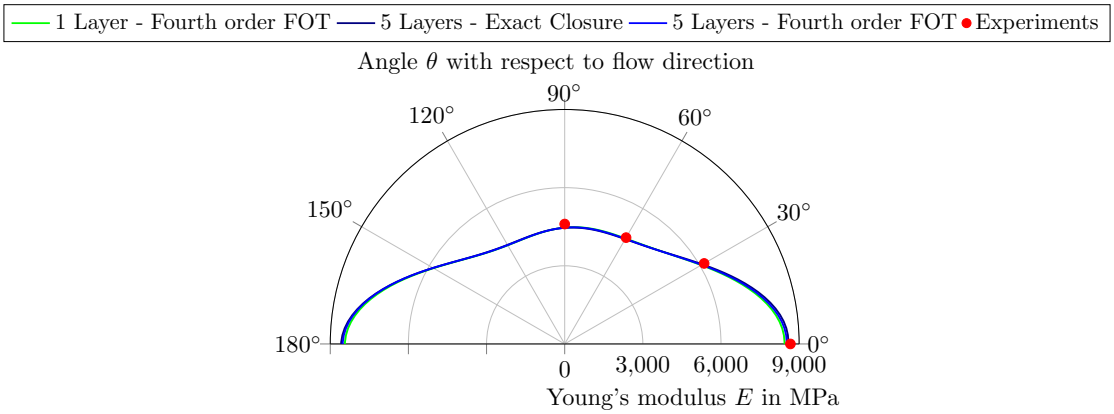

Figure 4.10: Effective Young's modulus for the microstructures with varying FOT over layers compared to experimental results adapted from Dey et al. [12, Fig. 12].

We observe that the five layer microstructures convey a similar elastic response compared to the microstructure prescribed with the fourth-order single layer FOT, see Fig. 4.10. The

FOT	Fiber count	$e^E_{0^\circ}$	$e^E_{30^\circ}$	$e^E_{60^\circ}$	$e^E_{90^\circ}$
1 Layer - Fourth order FOT	1932	2.78%	2.06%	0.73%	2.63%
5 Layers - Exact closure	1930	0.92%	1.19%	1.39%	3.14%
5 Layers - Fourth order FOT	1930	1.62%	1.76%	1.11%	3.06%

Table 4.7: Relative error of Young's modulus of microstructures with varying FOT over layers compared to experimental Young's modulus adapted from Dey et al. [12, Tab. 7].

results outlined in Table 4.7 indicate that the relative errors of the five layer microstructures are lower than the mean fourth-order FOT microstructure, roughly by an order of two in the flow direction, i.e, the 0° direction. However, for the five layer microstructure, the error in the 90° direction increases slightly but the overall error values are very small and below 1.4%. Nevertheless, the elastic responses of the five-layer microstructures using the fourth-order FOT and the second-order FOT with the exact closure approximations [128, 129] are very close. We also observe that the number of layers does not cause a significant difference in the number of fibers present in the unit cell.
Thus, we conclude that a five layer microstructure generated using the microstructure descriptors given in Section 4.3.1 and prescribed with the second-order FOT outlined in Table 4.1 along with the exact closure approximations [128, 129] characterizes the elastic response in different directions with sufficient fidelity. However, we focus solely on the in-plane deformation since all the experimental investigations were performed in the in-plane direction. It may be possible that the microstructure needs to be characterized with more than five layers for the out-of-plane deformation. In the further steps we use this RVE for generating the training data for the DMN which is then used for the *inverse calibration* of the material model.

4.3.2 Training of the DMN model

In our use case, the pure matrix and the E-glass fibers make up the phases of the microstructure identified in Section 4.3.1. Utilizing the direct DMN outlined in Section 3.2.2, we initialized the parameters $\vec{\boldsymbol{p}}$ in accordance with Gajek et al. [71]. We produced training and validation data using full-field FFT-based computational homogenization. The

two linear elasticity tensors $\mathbb{C}_1^s$, $\mathbb{C}_2^s$ and the effective elasticity tensor $\bar{\mathbb{C}}_{\mathtt{FFT}}^s$ form the triples $\left(\mathbb{C}_1^s, \mathbb{C}_2^s, \bar{\mathbb{C}}_{\mathtt{FFT}}^s\right)$ for training and validation. The tuples $(\mathbb{C}_1^s, \mathbb{C}_2^s)$ were sampled using the method outlined in Liu and Wu [70] that makes use of orthotropic elasticity tensors. The FFT-based computational homogenization software FeelMath [133] was used to compute the effective properties $\bar{\mathbb{C}}_{\mathtt{FFT}}^s$. We generated 1000 samples, divided into 800 training samples and 200 validation samples. The effective stiffness computed by the DMN is denoted as $\bar{\mathbb{C}}_{\mathtt{DMN}}^s(\vec{\boldsymbol{p}})$ with phase stiffnesses $\mathbb{C}_1^s$ and $\mathbb{C}_2^s$ as an input and for a fixed parameter set $\vec{\boldsymbol{p}}$. The evaluation of the effective stiffness $\bar{\mathbb{C}}_{\mathtt{DMN}}^s(\vec{\boldsymbol{p}})$ proceeds in the same manner as in Gajek et al. [71].

We choose a layer depth of seven and the training proceeds in a similar manner as outlined in Dey et al. [11] by minimizing the objective function,

$$J(\vec{\boldsymbol{p}}) \longrightarrow \min_{\vec{\boldsymbol{p}}} \quad \text{with} \quad J(\vec{\boldsymbol{p}}) = \sum_{s=1}^{n_{\mathtt{b}}} J_s(\vec{\boldsymbol{p}}) + \Psi(\vec{\boldsymbol{p}}) \tag{4.3.2}$$

and the batch size $n_{\mathtt{b}} = 40$, the contributions

$$J_s(\vec{\boldsymbol{p}}) = \frac{1}{n_{\mathtt{b}}} \frac{\left\|\bar{\mathbb{C}}_{\mathtt{FFT}}^s - \bar{\mathbb{C}}_{\mathtt{DMN}}^s(\vec{\boldsymbol{p}})\right\|_1}{\left\|\bar{\mathbb{C}}_{\mathtt{FFT}}^s\right\|_1} \tag{4.3.3}$$

and the penalty term

$$\Psi(\vec{\boldsymbol{p}}) = \lambda \left(\mathbf{b}_1^T \langle \vec{\boldsymbol{v}} \rangle_+ - c_1\right) + \lambda \left(\mathbf{b}_2^T \langle \vec{\boldsymbol{v}} \rangle_+ - c_2\right), \tag{4.3.4}$$

where $c_1 = 0.822$ and $c_2 = 0.178$ represent the volume fractions of the corresponding phases and $\vec{\boldsymbol{v}}$ represents the vector of unconstrained weights as defined in Dey et al. [11, eq. (2.21)]. Here, $\mathbf{b}_1$ is a vector with ones at all odd indices and zero otherwise, and $\mathbf{b}_2$ is a vector with ones at all even indices and zero otherwise. We set the penalty factor λ to be 100. For the training, a minimum of the objective function (4.3.2) is sought with a stochastic batch-gradient-descent approach that is based on automatic differentiation and batches of size 40. We implemented the process in PyTorch [140], trained the network using the AMSGrad method [141] and modulated the learning rate using cosine annealing [142],

$$\beta(m) = \beta_{\mathtt{min}} + \frac{1}{2}(\beta_{\mathtt{max}} - \beta_{\mathtt{min}}) \left(1 + \cos\left(\pi \frac{m}{M}\right)\right), \tag{4.3.5}$$

where β and m denote the learning rate and epoch, respectively. The maximum learning rate is set to $\beta_{\mathtt{max}} = 0.0007$, whereas the minimum learning rate is set to $\beta_{\mathtt{min}} = 0$.

The parameter M has a value of 4000 and the DMN is trained up to 10 000 epochs. Fig. 4.11(a) describes the training progression. The objective function decreases monotonically throughout the first 100 epochs. The loss function then exhibits some oscillations. These are effects of the learning-rate modulation, which allows the loss function to escape local minima. The smallest loss of 0.00637 was recorded at epoch 9 942.
We introduce the sample-wise error

$$e_s = \frac{\left\| \bar{\mathbb{C}}^s_{\mathtt{FFT}} - \bar{\mathbb{C}}^s_{\mathtt{DMN}} \right\|_1}{\left\| \bar{\mathbb{C}}^s_{\mathtt{FFT}} \right\|_1}, \tag{4.3.6}$$

to assess the generalization capacities of the DMN. Additionally, we define the maximum and mean errors across all samples,

$$e_{\mathtt{max}} = \max_s e_s \quad \text{and} \quad e_{\mathtt{mean}} = \frac{1}{N_s} \sum_{s=1}^{N_s} e_s, \tag{4.3.7}$$

where N_s gives the number of samples in the training or the validation set, respectively. Fig. 4.11(b) displays the mean training and validation errors for the DMN during the course of epochs. We note that the trend of the loss function matches that of the mean training and validation errors. A further indication that there is no overfitting in the offline training phase is the simultaneous decrease in the training and validation error during training. The mean and maximum validation errors at the end of training are 1.25% and 9.6%, respectively.
Moreover, we found that the purely elastic training can be insensitive to long-term effects of creep loading. We refer to Dey et al. [11, § 3.3] for a detailed discussion. An alternative would be inelastic training. However, this method is only applicable to relatively simple inelastic material models [73] because it quickly becomes unaffordable to evaluate complex constitutive laws computationally. Therefore, we adopt an alternative early-stopping procedure using a surrogate model which shares the characteristics of long-term loading but is computationally cheap. This markedly improves the extrapolation to other complex models for creep loading. We use Hooke's law in combination with a Norton-type creep law [78]

$$\begin{aligned} \boldsymbol{\sigma} &= \kappa \operatorname{tr}[\boldsymbol{\varepsilon}] \boldsymbol{1} + 2\mu \operatorname{dev}[\boldsymbol{\varepsilon} - \boldsymbol{\varepsilon}^{\mathrm{c}}], \\ \dot{\boldsymbol{\varepsilon}}^c &= \dot{\varepsilon}_0 (A_n \sqrt{3/2} \, \|\operatorname{dev} \boldsymbol{\sigma}\|)^{n_n} \frac{\operatorname{dev}[\boldsymbol{\sigma}]}{\|\operatorname{dev}[\boldsymbol{\sigma}]\|}, \end{aligned} \tag{4.3.8}$$

with creep parameters A_n and n_n, as a surrogate model and we monitor the performance of the DMN every 50 epochs during training using this model. We evaluate the Norton

Matrix	Elastic	$E = 2399.3$ MPa	$\nu = 0.4$	
	Creep	$A_n = 0.014$ 1/MPa	$n_n = 26.96$	$\dot{\varepsilon}_0 = 1.0$ s^{-1}

Table 4.8: Identified material parameters for the Norton-type model (4.3.8) adapted from Dey et al. [12, Tab. 8].

law using the material parameters outlined in Table 4.8 for the pure matrix and identified in Dey et al. [11, § 3.3]. These material parameters are identified using the forward calibration workflow based on experiments on the pure matrix and are kept fixed for the inelastically-informed offline training. Although these parameters do not describe the creep behavior of the matrix with sufficient accuracy, they provide a cheap and easy-to-evaluate inelastic input to the linear training process. Furthermore, we introduce an error measure to evaluate the performance of the creep response of the DMN compared to FFT full-field simulations using the Norton model for the pure matrix in three different loading directions 0°, 30° and 90° with respect to the flow direction,

$$e^n_{\theta,t} = \frac{\left|\bar{\varepsilon}^{\texttt{DMN,Norton}}_{\theta,t} - \bar{\varepsilon}^{\texttt{FFT,Norton}}_{\theta,t}\right|}{\max_\tau \left|\bar{\varepsilon}^{\texttt{FFT,Norton}}_{\theta,\tau}\right|} \quad \text{for} \quad \theta = 0°, 30°, 90° \tag{4.3.9}$$

and the maximum errors

$$e^n_\theta = \max_\tau e^n_{\theta,\tau} \quad \text{as well as} \quad e^n = \max_\theta e^n_\theta. \tag{4.3.10}$$

The creep response of the DMN using the Norton model was evaluated on a single voxel microstructure by an FFT-based solver [137]. We prescribed 32 time steps, equally spaced on the logarithmic time scale. The full-field simulations were performed with the FFT-based solver [137] using the full microstructure defined in Section 4.3.1.

In the 0° direction, we apply a uni-axial tensile stress $\bar{\sigma}_{11}$ in the flow direction which is ramped up to 95 MPa in 8.5 s and subsequently held constant for 5.52×10^3 s. We evaluated the creep strain component $\bar{\varepsilon}_{11}$ in the flow direction over the entire simulation window. In the 0° direction, we denote the evaluated strain by the symbol $\bar{\varepsilon}_{0°}$. We apply a lower uni-axial stress $\bar{\sigma}_{22}$ of 58.4 MPa until 4.48×10^2 s for the creep response in the 90° direction. We evaluate the strain component $\bar{\varepsilon}_{22}$ during loading and refer to the results as $\bar{\varepsilon}_{90°}$.

For the 30° direction, we use a similar strategy incorporating mixed boundary conditions [143] for a uni-axial tensile stress of 69 MPa, held constant up to 4.45×10^5 s.

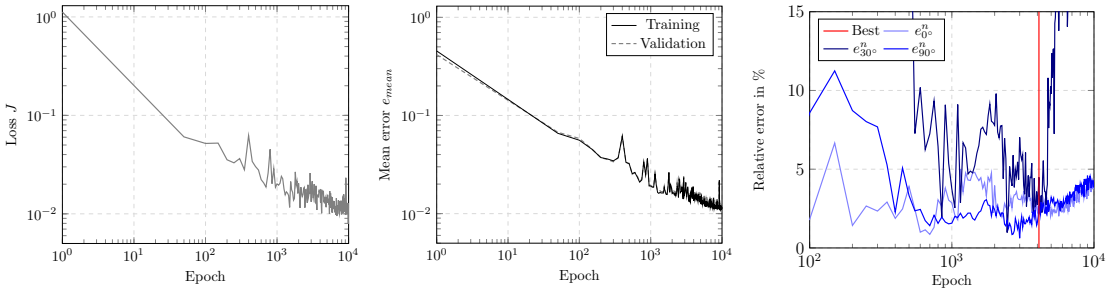

(a) Loss function (b) Mean error (c) Norton error

Figure 4.11: Offline training results and evaluated inelastic error during training adapted from Dey et al. [12, Fig. 13].

e^n	Stored at epoch	e^p	e^c
2.35%	4150	4.34%	2.44%

Table 4.9: Results of online evaluation of DMN with the inelastically-informed offline training method adapted from Dey et al. [12, Tab. 9].

During the entire simulation time, we evaluated the creep strain component $\bar{\varepsilon}_{11}$, and refer to it as $\bar{\varepsilon}_{30°}$.

The best DMN state is identified with the help of the best Norton error e^n in the entire training window, see Table 4.9. We refer to Dey et al. [11, Alg. 1] for a more comprehensive overview of the training procedure. The evolution of the Norton error over the epochs during the training is shown in Fig. 4.11(c). We observe a rather high Norton error at the start of the training, especially in the 90° direction, which oscillates and reaches a minimum at around epoch 4 000 before rising again.

We validate the performance of the DMN in the online phase by using the best trained DMN state to evaluate both the elasto-plastic and creep response using the fully coupled plasticity-creep law introduced in Section 4.2.3 for the matrix material. We follow Dey et al. [11] and introduce the maximum relative elasto-plastic error e^p [11, eq.(3.9)] and the maximum relative creep error e^c [11, eq.(3.11)] to evaluate the elasto-plastic and full creep response, respectively. The best elasto-plastic and creep error evaluated using the best identified DMN state are given in Table 4.9. The comparison of the DMN and full-field results for the elasto-plastic and creep case is shown in Fig. 4.12 (for the directions having the maximum errors). The trained DMN yields relatively low errors for elasto-plasticity

and creep below 5%. Therefore, we conclude that the trained DMN represents the inelastic response of the identified microstructure with a high fidelity when compared to full-field FFT simulations. It is to be noted that the runtime of the DMN online phase is below 30 s for both elasto-plasticity and creep when run on a single CPU on a computing node, whereas the FFT simulation run on a computing node with 24 CPUs and 4GB of memory per CPU in a HPC cluster lasts on an average more than four hours for the identified microstructure. The comparison of the runtimes leads to an average speed-up factor of 600 [11], which enables us to use the trained DMN for the *inverse calibration* workflow.

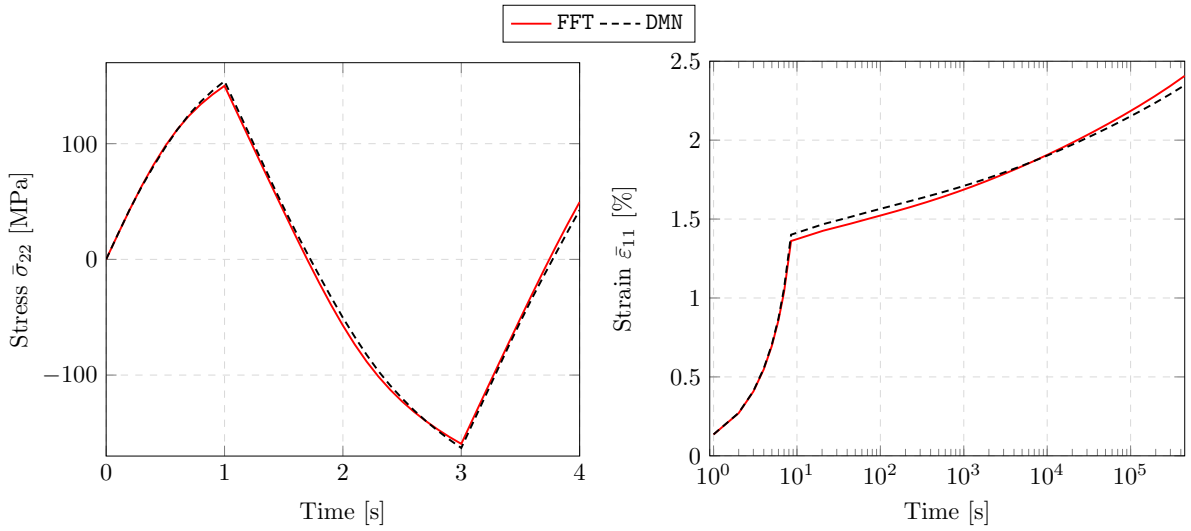

(a) Uniaxial extension in y-direction.

(b) Creep strain in 30° direction.

Figure 4.12: Comparison of DMN and full-field simulation for elasto-plasticity and creep adapted from Dey et al. [12, Fig. 14].

4.3.3 Inverse calibration of the constitutive law

Framework

In the previous sections we identified the best microstructure realization based on elastic computations and used it to train a DMN which represents the inelastic behavior of the composite with a high fidelity. Thus, the first two essential ingredients for the *inverse calibration* of the constitutive model of the matrix are available, see Fig. 4.1. In this

section we use the trained DMN for a cheap evaluation of the complete micromechanical problem and attempt to isolate the material parameters of our constitutive law outlined in Section 4.2.3 based on a single set of experiments performed on the composite, see Section 4.2.2, thereby circumventing the resource and time-intensive *forward calibration* workflow. Since we use the composite experiments, the process history during the manufacturing of the composite material is considered.
An incremental two-step procedure similar to the forward calibration (Section 4.2.4) is applied for identifying the material parameters of the matrix material. All elasticity and plasticity parameters are initially identified based on a uni-axial tensile experiment performed on the composite with deactivated progression of the creep strains. The remaining creep parameters are determined using long-term creep experiments conducted at various load levels in a particular direction using the composite, in the second step of this incremental parameter identification method, with frozen elasticity and plasticity coefficients.

Identification of elasticity and plasticity coefficients

The elasticity and plasticity parameters are identified using the experiment performed on the composite in the 0° loading direction, see Fig. 4.5. The optimization workflow is set up using the online phase of the DMN, implemented as a UMAT and evaluated on a single four-node unit tetrahedron element in Abaqus [120]. The Abaqus [120] simulation is iteratively called in an OptiSlang procedure [119] similar to the *forward calibration* procedure, see Section 4.2.4. The difference in the *inverse calibration* procedure is that instead of just evaluating the constitutive law of the matrix at the Gauss point, we evaluate the complete micromechanical problem using the DMN and find the effective response of the composite with the help of the trained DMN. The minimization problem consists of an objective function which minimizes the area under the curve between the composite experiment and the one obtained from the DMN simulation. The optimization is run with the two fixed matrix parameters, Poisson's ratio $\nu = 0.4$ and the viscosity $\eta = 0.001$ MPa $\cdot$ s, emulating strain-rate independence. The fiber parameters outlined in Table 4.3 are also kept fixed.

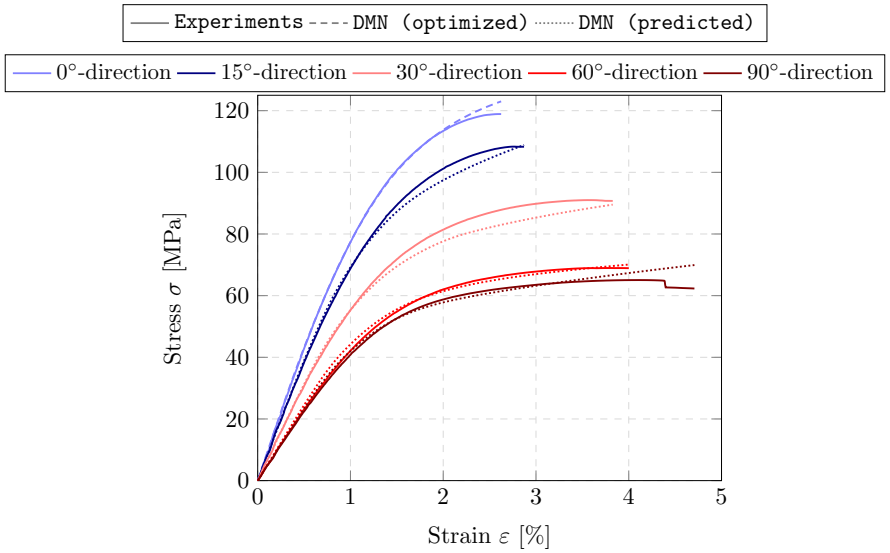

Figure 4.13: Experimental and simulation results with best fitting parameters using *inverse calibration* adapted from Dey et al. [12, Fig. 15].

The optimization procedure used is the same as in Section 4.2.4 using 300 samples and the best fitting parameters with respect to the composite experiment in the 0° direction is recorded in Table. 4.11 and the deviation in area between the experiment and simulation is 1.56%. These parameters are subsequently used to simulate the composite experiments in the 15°, 30°, 60° and 90° directions using the unit tetrahedron element, incorporating mixed boundary conditions [143] and solving the DMN online phase at the Gauss point. The plots comparing the composite experiments and the simulations with the best fitting parameters is shown in Fig. 4.13.

There is a remarkable agreement between the experiment and the simulations in the optimized 0°-direction up to 2% strain. This comes as no surprise. The saturation of the experimental results above 2% strain is not well represented. This is expected, as the used material model does not account for softening effects. The predicted directions also show a good fit at lower strain ranges. The fit is worse after the saturation yield stress point. The overall fit of the predicted directions up to around 1.3% strain is rather good considering that the parameters were optimized using only the 0°-direction composite experiments. The response is slightly underestimated above 1.3% strain level.

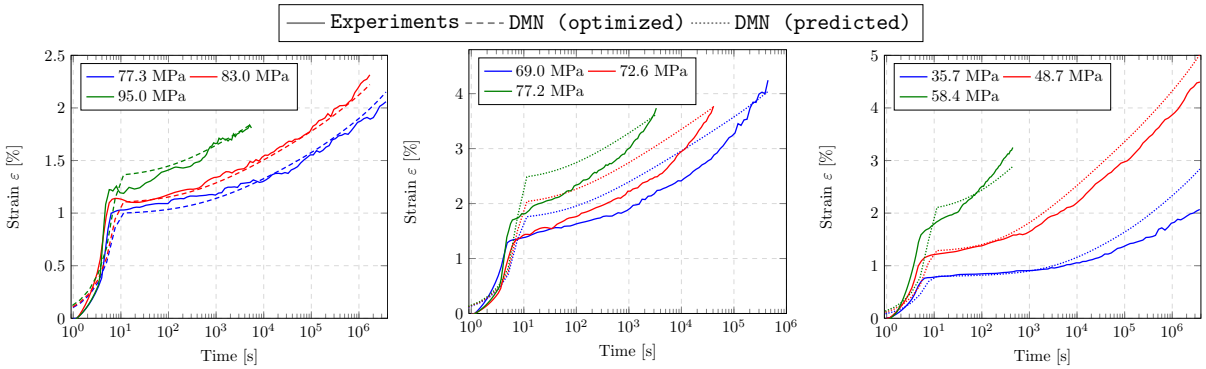

(a) 0° direction - DMN Optimized

(b) 30° direction - DMN Predicted

(c) 90° direction - DMN Predicted

Figure 4.14: Experimental and simulation results with best fitting parameters using 0° direction experiments for *inverse calibration* adapted from Dey et al. [12, Fig. 16].

Identification of creep coefficients

The identification of the creep parameters is also performed in OptiSlang [119], wrapping a unit-tetrahedron Abaqus [120] simulation following the same workflow as in Section 4.3.3. The Abaqus [120] simulation is furnished with the DMN at the Gauss point level, thus cheaply solving the micromechanical problem. The simulation is compared to the creep experiments performed on the composite in the 0°-direction at various stress levels, see Fig. 4.6(a). The objective function used is defined in eq. (4.2.13) with $n_{\text{Stresses}} = 3$ and the approach used is similar to Section 4.2.4. During the optimization run, the previously identified elasticity and plasticity parameters, the fiber parameters outlined in Table 4.3 and the reference creep rate $\dot{\varepsilon}_0 = 1.0\ \text{s}^{-1}$ are kept fixed.

The minimization problem using 300 samples is set up following Section 4.2.4. The best fitting parameters obtained using the least value of the global objective function (4.2.13) are given in Table 4.11. The local objective function 4.2.14 at each stress level is shown in Table 4.10 for the best fitting parameters not only for the optimized 0° direction but also for the predicted 30° and 90° directions. The experimental creep curves at different stress levels are plotted against the best fitting simulation in the log time scale in Fig. 4.14(a). Furthermore, the best fitting parameters are used to simulate the composite experiments at different load levels in the 30° and 90° directions, see Figs. 4.14(b),4.14(c).

In the 0° direction the parameters identified using *inverse calibration* capture the three

creep phases rather well, and represent the three experimental results to a sufficient fidelity which is also evident from the values of the local objective function recorded in Table 4.10. The load application phase and the creep strains in the primary and secondary creep stages are slightly over-estimated in the 30° direction leading to higher values of f_{local}, see Table 4.10. However, the final creep strain is remarkably well represented in all three stress levels. This may be due to the experimental procedure wherein the load level in the samples is first ramped up and then held constant. During the ramp-up, since most of the fibers are loaded at an angle of 30°, the sample tends to move sideways and slightly erroneous strains are recorded. Finally, in the 90° direction, the load application and primary creep stages are captured with high fidelity. However, the creep strains are over-estimated after the secondary creep stage for lower stress levels, especially for the stress level of 35.7 MPa, see Table 4.10. Nonetheless, the prediction in the 30° and 90° directions is quite good considering the anisotropy and time-scales involved. The improvement in the prediction of the composite response using the *inverse calibration* workflow compared to the *forward calibration* is outlined in Section 4.3.5.

Direction	0°			30°			90°		
Stress	77.3 MPa	83.0 MPa	95.0 MPa	69.0 MPa	72.6 MPa	77.0 MPa	35.7 MPa	48.7 MPa	58.4 MPa
f_{local}	3.4%	2.5%	1.3%	4.0%	7.3%	12.9%	14.7%	9.7%	6.6%

Table 4.10: f_{local} for different stress levels in all three directions for best fit creep parameters of matrix using composite experiments in 0° direction for *inverse calibration* adapted from Dey et al. [12, Tab. 10].

Matrix	Elastic	$E = 2475.0$ MPa	$\nu = 0.4$	
	Plastic	$h = 4.0$ MPa	$\omega = 399.2$	$y_0 = 24.9$ MPa
		$y_\infty = 37.9$ MPa		
	Creep	$A_1 = 0.005$ 1/MPa	$n_c = 10.15$	$A_2 = 2.4 \times 10^{-13}$ 1/MPa
		$C = 2583.45$	$k = 0.018$	$\dot{\varepsilon}_0 = 1.0$ s^{-1}

Table 4.11: Material parameters for pure matrix obtained using *inverse calibration* of constitutive law adapted from Dey et al. [12, Tab. 11].

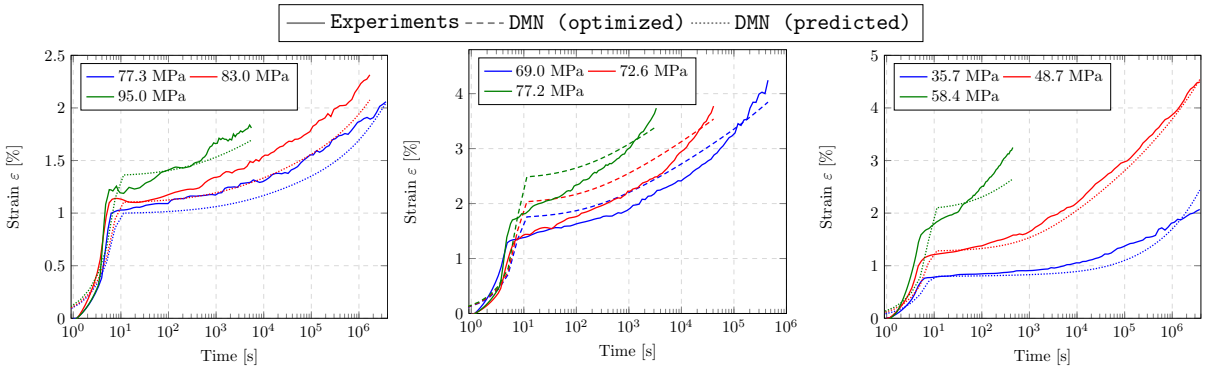

(a) 0° direction - DMN Predicted (b) 30° direction - DMN Optimized (c) 90° direction - DMN Predicted

Figure 4.15: Experimental and simulation results with best fitting parameters using 30° direction experiments for *inverse calibration* adapted from Dey et al. [12, Fig. 17].

4.3.4 On the influence of loading directions

In the previous section, we used the 0° loading direction for the *inverse calibration* of the constitutive model both for plasticity and for creep. Since the creep loading in every direction is performed over different stress levels within a wide range of time scales, we also investigate the influence of the loading directions on the inverse calibration framework. Another possibility would be to perform the *inverse calibration* using experiments from every direction. However, that would require the manufacturing of test plates in each direction and performing experiments on it, thereby increasing the experimental burden. Overall, the goal would be to reduce the number of direction-dependent experiments performed on the composite. To this effect, we seek to isolate the best set of experiments in a particular direction that we can use for inversely identifying the material parameters of the matrix. We use a similar approach as outlined in Section 4.3.3. However, we set up two separate minimization problems where we optimize the simulation using the global objection function (4.2.13) with the experiments performed in the 30° and 90° directions, respectively. The best fitting parameters obtained from each optimization is used to simulate the experiments in the remaining loading directions. The results of the simulation with the best fitting parameters obtained from the respective minimization problems for 30° and 90° directions are visualized in Figs. 4.15 and 4.16, respectively.

Direction	0°			30°			90°		
Stress	77.3 MPa	83.0 MPa	95.0 MPa	69.0 MPa	72.6 MPa	77.0 MPa	35.7 MPa	48.7 MPa	58.4 MPa
f_{local}	4.8%	10.6%	7.1%	4.4%	4.1%	3.9%	8.4%	1.8%	11.6%

Table 4.12: f_{local} for different stress levels in all three directions for best fit creep parameters of matrix using composite experiments in 30° direction for *inverse calibration* adapted from Dey et al. [12, Tab. 12].

The results are also quantitatively illustrated in Tables 4.12 and 4.13, where the f_{local} is recorded for the optimized and predicted directions using the best fitting parameters obtained from the optimization using the 30° and 90° directions, respectively.
We observe that the strain during the load application and primary stage of creep is overestimated for the *inverse calibration* using the 30° experiments, see Fig. 4.15(b), similar to the simulations using the 0° experiments, see Fig. 4.14(b). However, the value of f_{local} in the 30° direction is below 5%, see Table 4.12. As indicated in Section 4.3.3 this effect may be caused by the experimental procedure, wherein we cannot find a good fit for our constitutive law with the 30° experiments. Furthermore, the same parameters when used to simulate the 0° experiments, underestimates the creep strain at the end of creep, see Fig. 4.15(a). The creep strain in the primary and secondary creep stages at lower stress levels in the 90° directions are well represented, see Fig. 4.15(c). However, the highest stress level could not be well extrapolated which is reflected in the value of f_{local} for the stress level of 58.4 MPa, see Table 4.12.
The best fitting parameters obtained using the 90° experiments can represent all stress levels to a sufficient fidelity both in the 90° as well as in the 0° directions, see Figs. 4.16(c) and 4.16(a), respectively. The creep strains at end of the secondary creep stage for the lower stress levels are underestimated in the 0° direction, see Fig. 4.16(a). Nevertheless, we have a better fidelity compared to the simulations using best fitting parameters obtained from the optimization using the 30° experiments especially in the 0° and 90° directions, see Tables 4.12 and 4.13. Therefore, we conclude that the *inverse calibration* of the constitutive model may be performed with the experimental results having the highest confidence when we have multiple experiments available. In our case, we choose the experiments performed in the 0° direction for identifying the matrix parameters which are listed in Table 4.11 since it gives an overall good fit for other directions too. Moreover, the calibration using the experiments in a particular direction gives us the best results

in different load levels in the same direction. This comes as no surprise. Nevertheless, the best fitting parameters can predict the simulative results at a range of stress levels in different directions with good accuracy.

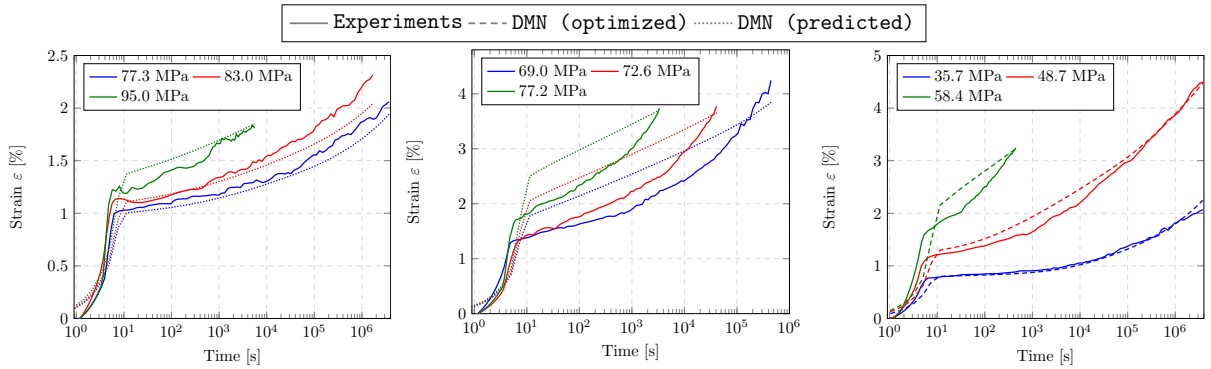

(a) 0° direction - DMN Predicted (b) 30° direction - DMN Predicted (c) 90° direction - DMN Optimized

Figure 4.16: Experimental and simulation results with best fitting parameters using 90° direction experiments for *inverse calibration* adapted from Dey et al. [12, Fig. 18].

Direction	0°			30°			90°		
Stress	77.3 MPa	83.0 MPa	95.0 MPa	69.0 MPa	72.6 MPa	77.0 MPa	35.7 MPa	48.7 MPa	58.4 MPa
f_{local}	6.0%	9.5%	2.4%	5.1%	6.8%	8.2%	3.7%	1.0%	5.2%

Table 4.13: f_{local} for different stress levels in all three directions for best fit creep parameters of matrix using composite experiments in 90° direction for *inverse calibration* adapted from Dey et al. [12, Tab. 13].

4.3.5 Comparison between forward and inverse calibration of constitutive model

Last but not least, we compare the performance of the *inverse calibration* of our fully coupled plasticity-creep model (Section 4.2.3) with the current state of the art *forward calibration* technique for an industrial-scale microstructure realization identified in Section 4.3.1. We perform full-field FFT simulations for plasticity and creep using the soft-

ware FeelMath [133] and assign the elasticity, plasticity and creep parameters identified using the pure matrix experiments outlined in Table 4.3 to the matrix material for the *forward calibration*. Instead of performing FFT simulations, the DMN online phase is used for the *inverse calibration* where we use the material parameters outlined in Table 4.11 for the matrix material. The fibers are assigned a linear elastic material law in both cases, using the parameters from Table 4.3. We also perform DMN simulations using the reduced geometrical representation of the microstructure for the *forward calibration* and compare all simulated results with the experiments performed on the complex composite (Section 4.2.2). The elasto-plastic response using both sets of material parameters is shown in Fig. 4.17. There is a strong difference in the composite response using the parameters from the *forward calibration* workflow and the experimental results. The DMN simulation in Fig 4.17(a) closely matches the FFT results. In the elastic phase we observe that there is a good agreement. Thereafter, the stresses in the plastic region are severely overestimated. It is to be noted that the model fitted the monotonic testing results of the pure matrix material quite well, see Fig. 4.7(a). If we take a look at the identified parameters in Tables 4.3 and 4.11 we see that the hardening parameter h shows a large difference. Moreover, the saturation yield stress y_∞ identified using the *inverse calibration* is almost 1.5 times smaller than the forward calibrated model. On the other hand, the elasto-plastic response matches the experimental results to a sufficient fidelity for the inversely calibrated model, see Fig. 4.17(b). If the *inverse calibration* framework were not available the next probable course of action would be to perform more time and resource consuming loading and unloading experiments for the pure matrix (instead of monotonic testing) for better characterizing the elasto-plastic response, especially the saturation yield stress y_∞.

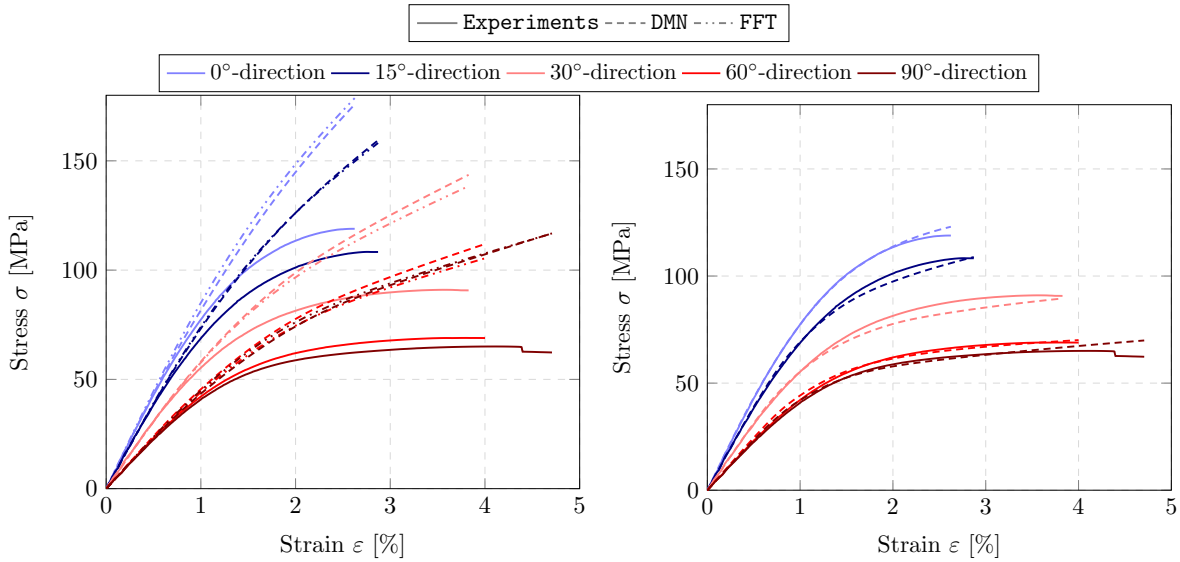

(a) Parameters using *forward calibration.* (b) Parameters using *inverse calibration.*

Figure 4.17: Experimental and simulation results with best fitting parameters for elasto-plastic loading adapted from Dey et al. [12, Fig. 19].

A similar comparison is performed for the creep loading in a range of load levels in three different directions depicted in Fig. 4.18. In addition to the experimental mean values of creep strains plotted in Section 4.2.2, we plot the range of strains obtained from all the samples at every stress level in each direction (highlighted in addition to the mean values in Fig. 4.18). This indicates the deviation in the experimental procedure for the different samples loaded under the same conditions and allows us to better compare the simulative results with the experimental results. We observe that the forward calibrated matrix model represents the load application and the primary creep stage with sufficient fidelity, especially for the lower load levels. We have a worse agreement for the onset of the secondary creep stage and beyond. It is worthwhile to note that the constitutive model can represent the entire creep range for the pure matrix with a good accuracy, see Fig. 4.7(b). The DMN and FFT results also match closely for smaller strains and show slight deviation at higher strains. The inversely calibrated model models the entire creep behavior with better accuracy. The primary stage in the 30° direction and the final creep strains in the 90° direction is slightly overestimated when considering the entire band of creep strain measurements, see Figs. 4.18(d) and 4.18(f). Nevertheless, the overall creep response is well represented considering the range of stresses and time scales involved.

In the absence of the *inverse calibration* workflow, a possible remedy to better model the creep response in the secondary stage would be to introduce an additional damage parameter during modeling the matrix material to speed-up the creep strain evolution. We would need additional experiments on the pure matrix to characterize the damage and then compare the composite response. This extra effort is elegantly side-stepped with the help of the inverse calibration workflow using DMNs. Thus, it is clear that the multi-scale simulations using material parameters from the pure matrix experiments does not fully capture the final composite behavior due to the change in the matrix properties during the manufacturing process. The DMN simulation unlocks the potential for identification of material parameters directly from the composite experiments.
The different steps involved in both the *forward* and *inverse* calibration along with the computations performed, hardware used and the computation times were summarized in Table 4.14. All the simulations were performed on a HPC cluster. Please note that although the data generation and training time for the DMN constitutes a large fraction of the total computation time in the *inverse* calibration workflow, they represent a one-time procedure. Once the DMN is trained, we can, in principle, use the trained DMN for the *inverse calibration* of any constitutive law of GSM-type attached to its constituents. The parameter optimization process can also be repeated any number of times for further refinement. This is certainly not the case in the *forward calibration* workflow where all the steps need to be repeated for further refinement or for a different constitutive law.

4.4 Conclusion

The deep material network framework introduced by Liu and coworkers [69, 70] opened up a vast array of opportunities to model the inelastic response of the composite for different design tasks by providing a fast yet remarkably accurate surrogate model of the microstructure, thereby effectively decoupling the material response of the constituents from the microstructural arrangement. The DMN framework has evolved into different variants tailored to solve the forward problem, i.e., find the overall composite response while having, at hand, the constitutive model for the individual phases of the composite, for different industrially-relevant material classes. Thereafter, the overall material response is validated with the help of experiments performed on the composite.

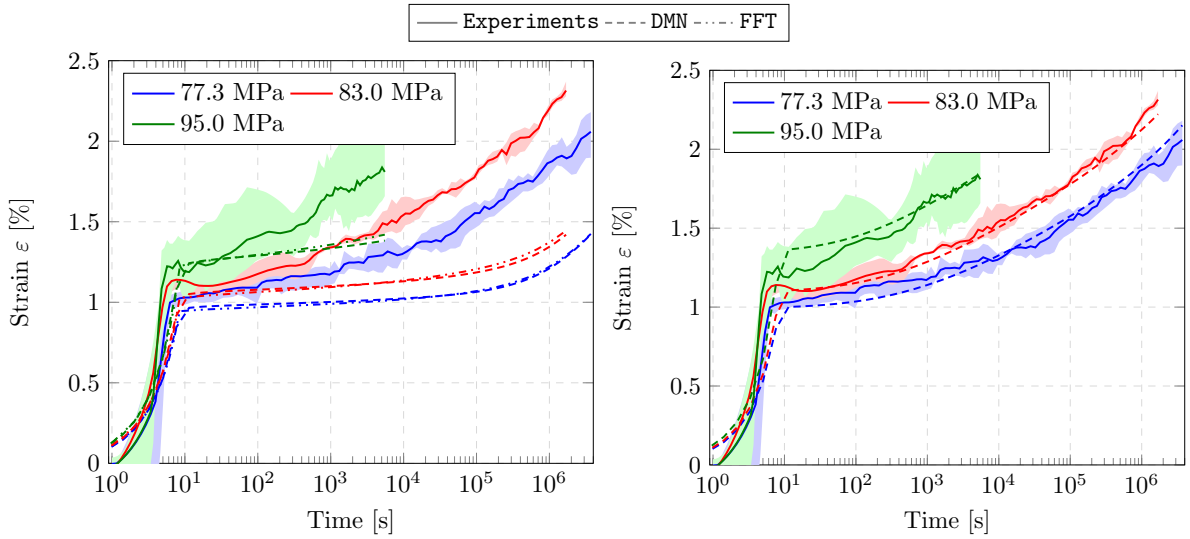

(a) Parameters using *forward calibration* - 0° direction.

(b) Parameters using *inverse calibration* - 0° direction.

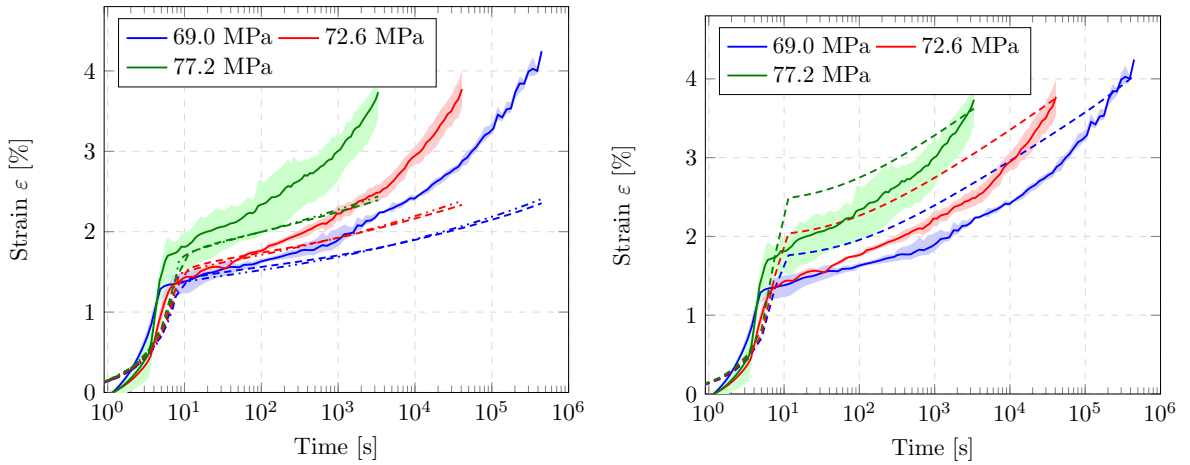

(c) Parameters using *forward calibration* - 30° direction.

(d) Parameters using *inverse calibration* - 30° direction.

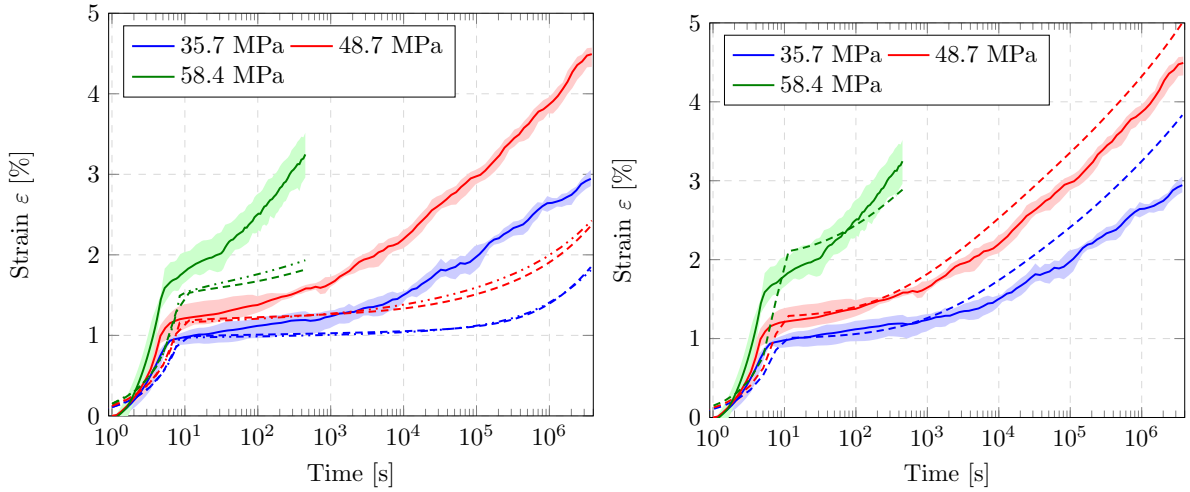

(e) Parameters using *forward calibration* - 90° direction.

(f) Parameters using *inverse calibration* - 90° direction.

Figure 4.18: Experimental and simulation results with best fitting parameters for creep loading adapted from Dey et al. [12, Fig. 20].

Calibration	Steps	Computations	Hardware	Runtime
Forward	**Optimization**: Elasticity and plasticity parameters	300 Abaqus unit cube simulations	Single node with 2 CPUs, 1 GB memory per CPU	1.8 hours
	Optimization: Creep parameters for 3 load levels	3 × 300 Abaqus unit cube simulations	3 nodes in parallel with 2 CPUs each, 4 GB memory per CPU	5.3 hours
	Validation: Elasto-plastic loading, 5 directions	5 FFT simulations	Single node with 24 CPUs, 4 GB memory per CPU	22.8 hours
	Validation: Creep loading, 3 directions, 3 load levels each	3 × 3 FFT simulations	Single node with 24 CPUs, 4 GB memory per CPU	60.8 hours
Inverse	**Data generation** for DMN	1000 elastic FFT simulations	14 nodes in parallel with 24 CPUs each, 4 GB memory per CPU	62.1 hours
	Training the DMN	PyTorch [140]	Single node with single CPU, 60 GB memory per CPU	11.3 hours
	Optimization: Elasticity and plasticity parameters	300 Abaqus unit tetrahedron simulations	Single node with 2 CPUs, 1 GB memory per CPU	6.1 hours
	Optimization: Creep parameters for 3 load levels	3 × 300 Abaqus unit tetrahedron simulations	3 nodes in parallel with 2 CPUs each, 1 GB memory per CPU	7.6 hours

Table 4.14: Summary of the steps involved in the *forward* and *inverse* calibration including the hardware used and the computation times adapted from Dey et al. [12, Tab. 14].

In this work, we used the DMN framework for solving the inverse problem, wherein we identified the parameters for the constitutive model (in our case, a fully coupled plasticity-creep law) of the polymer matrix by experiments performed on the composite.

We showed that such an approach is able to accurately identify the material parameters from the composite experiments and to represent the anisotropic response of the composite with sufficient fidelity. Such an approach using traditional FFT computations would be a formidable task due to the high runtime of full-filed simulations when compared to DMN simulations. We also critically discuss the essential ingredients necessary for the *inverse calibration* of any two-phase composite, which includes an accurate virtual representation of the microstructure involved and a set of reliable experiments performed using the composite. In the absence of these essential ingredients the *inverse calibration* may lead to less accurate results. Therefore, as a further step the DMN framework may be extended to capture the uncertainties in the microstructure [159, 160], as well. Moreover, considering failure [161–163] or fatigue [9, 93, 96] prediction and inversely calibrating these constitutive laws may be worth the effort.

Nevertheless, the *inverse calibration* workflow using DMNs provides an accurate and low-cost alternative to experimental characterization of the constitutive model of the constituents of an industrially relevant SFRT. Apart from reducing the experimental effort, this workflow enables the rapid development of a variety of inelastic constitutive laws for materials used for running concurrent multiscale simulations on an industrial scale.

5 On the effectiveness of Deep Material Networks for the multi-scale virtual characterization of short fiber-reinforced thermoplastics under highly non-linear load cases[1]

5.1 Introduction

In this chapter, we use an industrially relevant semi-crystalline thermoplastic PBT, reinforced with 30% by weight (17.8% by volume) E-glass fibers to characterize simultaneously the stiffness degradation under high-cycle fatigue and the material response under quasi-static and creep loadings. As a starting point, we build upon the work of Magino et al. [93] wherein a convex, rate-independent damage model based on the work of Görthofer et al. [94] was formulated in the logarithmic cycle space for the PBT matrix at the micro-scale. The constitutive model is concisely described in Section 5.2. However, with a view to upscale the model to the macro-scale, we integrate the model in the

[1]This chapter is *based on* Sections 2, 3, 4 and 5 of the publication A. P. Dey, F. Welschinger, M. Schneider, J. Köbler and T. Böhlke, "On the effectiveness of Deep Material Networks for the multi-scale virtual characterization of short fiber-reinforced thermoplastics under highly non-linear load cases," *Archive of Applied Mechanics*, vol. 94, p. 1177-1202, 2024. The introduction has been condensed to eliminate redundancy with Chapter 1, and the notation has been standardized.

direct DMN framework [71] which offers us a reliable and reasonably accurate surrogate model to solve the micromechanics. DMNs have already been used to simulate long-term load cases like creep [11]. The intrinsic convexity and the non-localized character of the fatigue-damage model enables a direct integration into the DMN framework. The DMN methodology is discussed briefly in Section 5.2. However, one of the drawbacks of the DMN is that it is restricted to a specific microstructural arrangement. To account for the spatially varying microstructure, an interpolation over the fiber orientation tensor is necessary. However, previous a priori approaches [72,74,76] for the FOT interpolation appear prohibitive for the harsh conditions of long-term loading. Furthermore, the representation of highly non-linear creep using DMNs require an additional inelastic input during training [11]. Therefore, aiming at a holistic approach for the simulation of quasi-static as well as long-term loading, we formulate an a posteriori approach where multiple DMNs are trained and the fiber orientation interpolation concept proposed by Köbler et al. [92] is used, see Section 5.2. The coupled plasticity-creep model, introduced in Section 4.2.3, is incorporated in the DMN framework for further validation.

We outline the results of the fiber orientation interpolation using the DMN framework in Section 5.3 not only for the fatigue-damage model introduced in Magino et al. [93] but also for the coupled plasticity-creep model introduced in Dey et al. [12]. We assess the predictive capabilities of the interpolation procedure by comparing the DMN-based interpolation with full-field FFT simulations. Furthermore, the relative error and the computation time of the DMN-based upscaling is also compared with the MOR-based upscaling.

Finally, in Section 5.4, we leverage the power of the DMNs to inversely characterize [12] the stiffness degradation under high cycle fatigue using macro-scale experiments performed on the composite. Since the DMNs model the spatial geometry of the microstructure, any material model may be used for the constituents of the composite. This contrasts with the full-field FFT micro-scale and MOR macro-scale approach adopted in Magino et al. [93,96], where the material model for the matrix is fixed in the micro-scale and cannot be further modified based on the results of the FOT-interpolated macro-scale. We exploit this *model-free* nature of the DMN to modify the existing fatigue damage model [93]. We extend the linear damage evolution with the help of a non-linear power-law term. Finally, we plug this model into the DMN-based interpolation concept for the inverse characterization [12] of the matrix material using a 9-layer macroscopic sample and compare them to experimental results.

5.2 Generalized DMN-based database for variable fiber orientation

5.2.1 Fatigue-damage model for matrix

The fatigue-damage model proposed in Magino et al. [93] for the stiffness degradation at small strains is formulated in the generalized standard material (GSM) framework [101]. GSMs are preserved under a scale transition in the context of multiscale modeling, e.g., in the case of DMNs [72]. The model is formulated in logarithmic cycle space denoted by a continuous variable $\bar{N} \geq 0$, as a replacement of the commonly used time scale. The rescaling using $\bar{N} = \log_{10} N$, where N represents the current cycle, allows us to perform efficient fatigue computations using large steps $\Delta\bar{N}$ in the logarithmic cycle space.
The free energy density of the model [93] is defined, with the help of the macroscopic strain tensor $\boldsymbol{\varepsilon}$, the initial fourth-order stiffness tensor $\mathbb{C}$ and a scalar damage variable d, which is an internal variable, as

$$\psi(\boldsymbol{\varepsilon}, d) = \frac{1}{2(1+d)} \boldsymbol{\varepsilon} : \mathbb{C} : \boldsymbol{\varepsilon}, \tag{5.2.1}$$

where $d \geq 0$. The stress is computed as

$$\boldsymbol{\sigma} \equiv \partial_{\boldsymbol{\varepsilon}} \psi = \frac{1}{(1+d)} \mathbb{C} : \boldsymbol{\varepsilon}. \tag{5.2.2}$$

The dissipation potential is defined in the GSM framework

$$\phi(d') = \frac{1}{2\alpha} (d')^2, \tag{5.2.3}$$

where α is a positive variable determining the speed of damage evolution and $d' = \mathrm{d}d/\mathrm{d}\bar{N}$. Finally, the evolution of the internal variable d, in an explicit form, is defined as

$$d' = \frac{\alpha}{2(1+d)^2} \boldsymbol{\varepsilon} : \mathbb{C} : \boldsymbol{\varepsilon}, \tag{5.2.4}$$

where the damage variable d develops linearly in the logarithmic cycle space $\bar{N}$. The evolution equation (5.2.4) is discretized with an implicit Euler method in the logarithmic cycle space. The parameters of the fatigue-damage model are sourced from Magino et al. [93, § 2.3], identified using experiments performed with PBT matrix and the reinforced composite. The parameters are given in Table 5.1.

Matrix [93, § 2.3]	Elastic	$E = 2690$ MPa	$\nu = 0.4$
	Damage	$\alpha = 0.015$ 1/MPa	
Fibers [121]	Elastic	$E = 72000$ MPa	$\nu = 0.22$

Table 5.1: Material parameters under fatigue loading - matrix parameters identified from experiments adapted from Dey et al. [13, Tab. 1].

5.2.2 Deep Material Networks

Framework

Liu et al. [69, 70] first proposed DMNs as a data-driven surrogate model for full-field micro-scale simulations in concurrent multiscale approaches. We build upon the direct DMN framework introduced in Gajek et al. [71] and report on a further extension of the framework by an early stopping strategy proposed in Dey et al. [11] for modeling of long-term creep deformation. DMNs act as a high-level surrogate for a finite element discretization of an N-phase microstructure as outlined in Section 3.2. In this section, we introduce the DMN framework in a different flavor, designed for upscaling using FOT interpolation by dividing it in two distinct phases: offline training and online evaluation. We supplement the offline training phase using an inelastically-informed training strategy as outlined in Dey et al. [11].

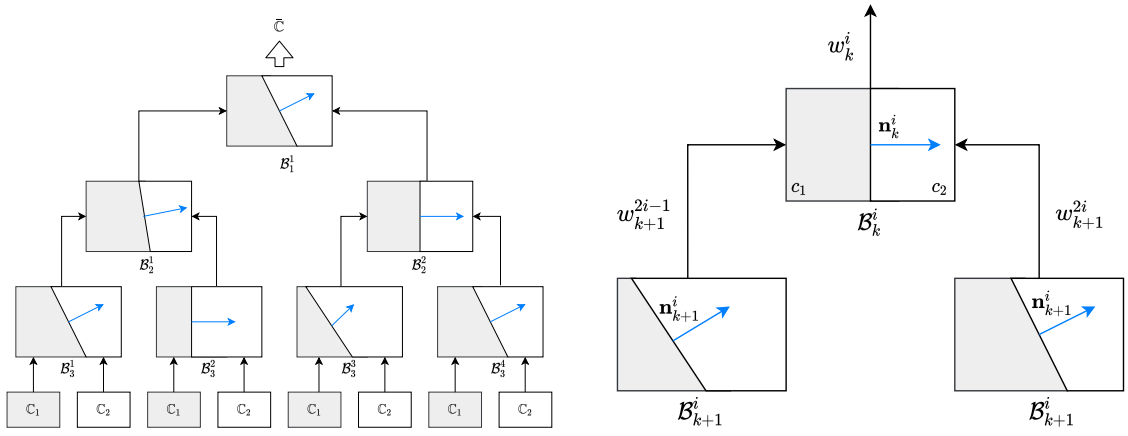

(a) A three-layer binary tree of laminates (b) Building block of DMN

Figure 5.1: A two-phase deep material network adapted from Dey et al. [12, Fig. 9].

Offline training

In computational micromechanics, the DMNs aim to replace computationally expensive full-field simulations. Direct deep material networks [71] use a hierarchical binary tree of rotation-free laminates as shown in Fig. 5.1(a) to represent a two-phase microstructure. In the linear elastic scenario, evaluating the effective stiffness of a two phase laminate with a normal $\boldsymbol{n}$, which stands for the direction of lamination, and the volume fraction of its constituents, indicated by c_1 and c_2, is computationally inexpensive.
The binary tree of laminates aims to find an effective model of a complex microstructure Y and enables the fast evaluation of the homogenization function $\mathcal{DMN}_Y$. The two-phase laminate $\mathcal{B}_k^i$, shown in Fig. 5.1(b), forms each building block of the DMN. A DMN with K layers utilizing a running index $k = 1, \dots, K$ (from top to bottom layer K) is considered. The total number of nodes in the DMN is $2^K - 1$ where $i = 1, \dots, 2^K - 1$. We evaluate the homogenized effective stiffness of the DMN using the stiffness tensors $\mathbb{C}_1$ and $\mathbb{C}_2$ of the input materials,

$$\bar{\mathbb{C}} = \mathcal{DMN}_Y(\mathbb{C}_1, \mathbb{C}_2) \tag{5.2.5}$$

by traversing the binary tree from the bottom to the top and by computing the effective laminate stiffness at every node

$$\mathbb{C}_k^i = \mathcal{B}_k^i(\mathbb{C}_{k+1}^{2i-1}, \mathbb{C}_{k+1}^{2i}), \quad k = 1, \dots, K, \quad i = 1, \dots, 2^{k-1}. \tag{5.2.6}$$

The effective stiffness of a laminate can be analytically computed [164, § 9.5], independent of the anisotropy of the input stiffnesses and the geometrical parameters of the laminate. For more details about the homogenization at every building block please refer to Gajek et al. [71, § 3.2].

The input materials are assigned to the bottom layer of the DMN in an alternate fashion,

$$\mathbb{C}_{K+1}^i = \begin{cases} \mathbb{C}_1, & i \text{ odd}, \\ \mathbb{C}_2, & i \text{ even}. \end{cases} \tag{5.2.7}$$

Liu et al. [69] proposed to parameterize the laminates' volume fractions using weights w_{K+1}^{2i-1} and w_{K+1}^{2i} which are attached to each laminate at the input layer $K + 1$. All allowable weights are non-negative and add up to one. As we progress up the layers, these weights are additively propagated

$$w_k^i = w_{k+1}^{2i-1} + w_{k+1}^{2i}. \tag{5.2.8}$$

The volume fractions of each building block can be retrieved by normalizing the weights

$$c_1 = \frac{w_{k+1}^{2i-1}}{w_{k+1}^{2i-1} + w_{k+1}^{2i}} \quad \text{and} \quad c_2 = 1 - c_1. \tag{5.2.9}$$

A direct DMN is uniquely parameterized by the lamination direction of each laminate $\boldsymbol{n}$ and the weights attached to the input layer w_{K+1}^i, which can be organized into a parameter vector $\vec{\boldsymbol{p}}$. The vector $\vec{\boldsymbol{p}}$ of the DMN can then be identified based on linear elastic material sampling and optimization in terms of a cost function which will be discussed in later sections. Once the DMN is identified, it may be used to compute nonlinear and inelastic constitutive behavior, as outlined in Section 5.2.2.

However, the proposed theory [71] behind DMNs suggests the results tends to be inaccurate if the constitutive laws exhibit a significant degree of nonlinearity. This has been also been shown when predicting the material response under long-term creep loading, see Dey et al. [11, § 3.2]. To circumvent this limitation, we follow an early-stopping strategy [109, § 7.8] and evaluate the inelastic material law every 50th or 100th iterate during training. Thus, the DMN parameters $\vec{\boldsymbol{p}}$ are identified every epoch with the help of the elastic loss, but the best state of the DMN is identified using the best inelastic error. This inelastically informed training methodology was further accelerated using a simple Norton-type creep law [78] in Dey et al. [11, § 3.3] to accurately predict the quasi-static and long-term creep response using DMNs.

Online evaluation

In the online phase, the inelastic response of the DMN is determined while keeping the parameter vector $\vec{\boldsymbol{p}}$ constant. We follow the approach introduced by Gajek et al. [71] to solve the online phase of the DMN, where a flattened representation of the DMN is used. In the online phase, our DMN resembles a traditional laminate with numerous phases. A nonlinear material behavior of GSM type is assigned to each phase of the flattened DMN. Each phase of the flattened DMN contains the internal variables of the nonlinear constitutive law.

For a prescribed macroscopic strain $\bar{\boldsymbol{\varepsilon}} = \nabla_s \bar{\boldsymbol{u}}$, a variational problem is set up for the online phase of the DMN,

$$\bar{\psi}(\bar{\boldsymbol{\varepsilon}}) = \inf_{\boldsymbol{a}} \left[\sum_{I=1}^{2^K} w_K^I \; \psi_K^I(\boldsymbol{\varepsilon}_K^I(\bar{\boldsymbol{\varepsilon}}, \boldsymbol{a}_k^i)) \right] \tag{5.2.10}$$

where $k = 1, \ldots, K$ and $i = 1, \ldots, 2^{k-1}$ and defined in terms of the displacement jump vectors $\boldsymbol{a}$, strains in the bottom layer $\boldsymbol{\varepsilon}_K^I$, and the free energies

$$\psi_K^I(\boldsymbol{\varepsilon}_K^I) = \begin{cases} \psi^1(\boldsymbol{\varepsilon}_K^I), & I \text{ odd}, \\ \psi^2(\boldsymbol{\varepsilon}_K^I), & I \text{ even}. \end{cases} \tag{5.2.11}$$

The index $I = 1, \ldots, 2^K$ represents the phases in the bottom layer of the deep material network. The strains in each phase of the bottom layer of the DMN can be evaluated based on the approach followed in Gajek et al. [72, eq. (3.16)]. The displacement jump vectors are attached to each node of the DMN online phase and are explicitly reported in Dey et al. [12, § 3.3]. The stresses on the macroscopic level are computed from eq. (5.2.10) via

$$\bar{\boldsymbol{\sigma}}(\bar{\boldsymbol{\varepsilon}}) \equiv \frac{\partial \bar{\psi}}{\partial \bar{\boldsymbol{\varepsilon}}} = \inf_{\boldsymbol{a}} \left[\sum_{I=1}^{2^K} w_K^I \, \boldsymbol{\sigma}_K^I \right], \tag{5.2.12}$$

where $\boldsymbol{\sigma}_K^I$ is the stress in each individual phase of the bottom layer given as

$$\boldsymbol{\sigma}_K^I = \partial_{\boldsymbol{\varepsilon}_K^I} \psi_K^I \tag{5.2.13}$$

and can be obtained from the respective constitutive law attached to each phase, see eqs. (5.2.2) and (4.2.4).

The unknown jump vectors $\boldsymbol{a}$ associated with each node of the DMN are solved via Newton's method, where we use a backtracking algorithm to ensure a stable convergence behavior. Please refer to Dey et al. [12, § 3.3] for more details. A DMN with K layers contains $2^K - 1$ nodes, and each Newton step updates all $3 \cdot 2^K - 1$ components of the jump vector $\boldsymbol{a}$ concurrently. To boost computational performance, we also use the last converged displacement jumps from the previous time step to initialize the displacement jumps $\boldsymbol{a}$ at the start of the Newton iteration. This decrease in runtime is offset by an increase in memory demand to store the vector at the conclusion of each time step. In the case inelastic models are used, the internal variables attached to every phase of the bottom layer are stored. A DMN of depth K with 2^{K-1} laminates in the bottom layer consists of

$$Z_1 \cdot 2^{K-1} + Z_2 \cdot 2^{K-1} \tag{5.2.14}$$

internal variables, where Z_1 and Z_2 represent the number of internal variables for each phase. The internal variables (5.2.14) are updated after the convergence of Newton iteration. The online phase is implemented as a user-defined material subroutine (UMAT) in

Fortran, which makes use of the LAPACK [138] libraries for an efficient computation of the linear algebra operations and can be easily integrated into commercial software, like Abaqus [120] or the commercial FFT solver FeelMath [133].

5.2.3 Fiber orientation interpolation

Advani and Tucker [165] introduced the second order fiber orientation tensor (FOT)

$$\mathbf{A}_2 = \int \boldsymbol{p} \otimes \boldsymbol{p}\, \rho(\boldsymbol{p})\, \mathrm{d}A(\boldsymbol{p}) \tag{5.2.15}$$

in terms of a fiber orientation distribution function ρ, which defines the probability of finding fibers in a particular direction $\boldsymbol{p}$. The FOT carries a limited amount of information with only five independent degrees of freedom. Despite its restricted information richness, the efficient form of the FOT makes it a popular choice for commercial injection molding simulations. The second-order FOT can be extended to higher moments using closure approximations [128, 129].

The FOT is a symmetric positive semidefinite tensor with unit trace. The eigenvalue decomposition of $\mathbf{A}_2$ leads to

$$\mathbf{A}_2 = \mathcal{Q}\, \mathrm{diag}(\lambda_1, \lambda_2, \lambda_3)\, \mathcal{Q}^T, \tag{5.2.16}$$

where $\mathcal{Q}$ is an orthogonal matrix and with eigenvalues $\lambda_1 \geq \lambda_2 \geq \lambda_3$ sorted in descending order. Therefore, up to a rotation, the fiber orientation tensor $\mathbf{A}_2$, can be uniquely defined by two positive real numbers λ_1 and λ_2 satisfying

$$\frac{1}{3} \leq \lambda_1 \leq 1 \quad \text{and} \quad 1 - 2\lambda_1 \leq \lambda_2 \leq \lambda_1, \tag{5.2.17}$$

the two inequalities. These inequalities can be represented geometrically in the form of a planar triangle, see Fig. 5.2. We call this triangle the FOT triangle and use the CMYK color scheme proposed by Köbler et al. [92], see Fig. 5.2.

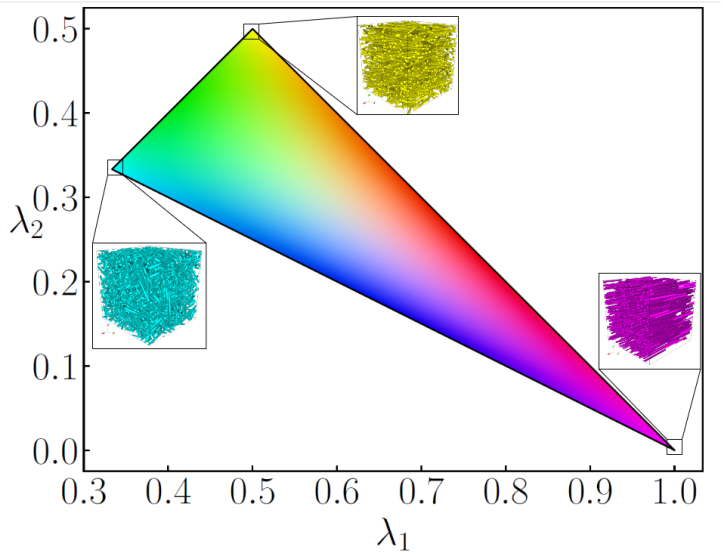

Figure 5.2: Fiber orientation triangle depicting the two highest eigenvalues of the fiber orientation tensor. The three extreme cases, i.e., the vertices of the triangle, unidirectional (magenta), isotropic (cyan) and planar isotropic (yellow) fiber orientation are shown and is adapted from Gajek et al. [72, Fig. 3].

The manufacturing of SFRT components using injection molding introduces a spatially varying microstructure throughout the component. Therefore, the total anisotropic nature of the composite must be considered when modeling the material in the micro-scale. DMNs offer us an effective surrogate to model the complete anisotropic picture at the micro-scale. However, the DMNs are intrinsically limited to a particular microstructural state and there emerges a natural need to model spatially varying microstructural states using DMNs. Liu et al. [76] used a transfer learning paradigm to train a single DMN progressively over various microstructure states to create a unified database that encompasses a range of geometric descriptors. On the other hand, Gajek et al. [72] used the FOT triangle in association with a DMN to jointly identify parameters of the DMN. This approach yields a single DMN surrogate model that covers all fiber orientations. Both the aforementioned approaches were performed for heterogeneous microstructure having elasto-plastic constituents.

However, as part of this work we aim to introduce a multiscale model simultaneously for the stiffness degradation under high cycle fatigue with strong non-linearity and deformation under creep loading for large time scales. Dey et al. [11] showed that identifying an accurate surrogate model for long-term creep loading requires additional inelastic in-

puts during the elastic offline training phase. Hence, identifying a single DMN surrogate model for all FOT states appears prohibitive for high cycle fatigue and long term creep. Therefore, we use the idea proposed in Köbler et al. [92], where a fiber orientation interpolation is performed using effective stresses, with the stresses originating from individually trained DMNs.

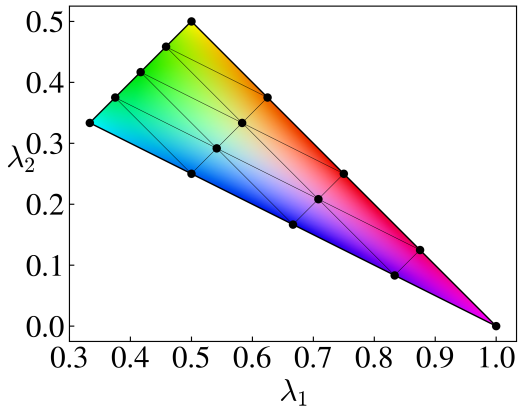

Figure 5.3: A discretization of the fiber orientation triangle with 15 nodes adapted from Dey et al. [13, Fig. 3].

To this effect on the micro-scale, we first triangulate the FOT triangle using 15 fiber-orientation nodes, resulting in 16 sub-triangles, see Fig. 5.3. Each triangulation node represents a microstructural state and is furnished with a microstructural image Y_i, where $i = 1, \ldots, 15$, generated using the sequential addition and migration (SAM) algorithm [127] and the FOT computed using the λ_1 and λ_2 values of the particular node. Thereafter, we generate training and validation data for the DMNs at each node using elastic full-field FFT-based computational homogenization. These serve as the input for training the DMNs at every node. The trained DMN parameters $\vec{\boldsymbol{p}}_i$ are stored in a database for use in the macro-scale computations.

On the macro-scale, the inputs consist of the DMN parameters of the 15 trained DMNs at each node and the material models of the constituents of the composite. Each element is connected with the DMN parameters of the three nearest pretrained orientations based on its assigned orientation, see Köbler et al. [92]. Therefore, any fiber orientation state Λ can be represented uniquely in terms of a convex combination

$$\Lambda = s_1\Lambda_1 + s_2\Lambda_2 + s_3\Lambda_3 \tag{5.2.18}$$

of the fiber-orientation states Λ_1, Λ_2 and Λ_3 contained in the FOT triangle and a triple of positive numbers (s_1, s_2, s_3) which sum to unity. Thus, for a macroscopic strain E the macroscopic stress Σ is calculated

$$\Sigma = \sum_{i=1}^{3} s_i \bar{\boldsymbol{\sigma}}_i(E, \vec{\boldsymbol{p}}_i, \boldsymbol{\sigma}_K^I), \tag{5.2.19}$$

where $\bar{\boldsymbol{\sigma}}_i$ denotes the DMN online phase stress (5.2.12) calculated at each node of the containing triangle dependent on the DMN parameters $\vec{\boldsymbol{p}}_i$ and the stresses $\boldsymbol{\sigma}_K^I$ defined in eq. (5.2.13), which emerge from the respective material models. As a result, the stresses at the node are interpolated, and the nodal internal variables (5.2.14) of the DMN develop independently and reside on the nodes Λ_1, Λ_2 and Λ_3. The entire FOT interpolation workflow has been summarized as an algorithm similar to Magino et al. [93, Fig. 6] in Fig. 5.4. An essential difference to the MOR based workflow introduced in Magino et al. [93] is the decoupling of the macro-scale simulation from the material model of the constituents, leveraging the power of the DMN which serves as an efficient surrogate of only the geometric state.

The FOT interpolation framework in the macro-scale is implemented as an Abaqus [120] UMAT following Köbler et al. [92] which calls upon the DMN online phase UMAT at every node of the triangle, which further integrates the UMAT for the constitutive laws of each constituent of the composite. The trained DMN parameters are stored as an XML file and integrated using the UEXTERNALDB routine of Abaqus [120].

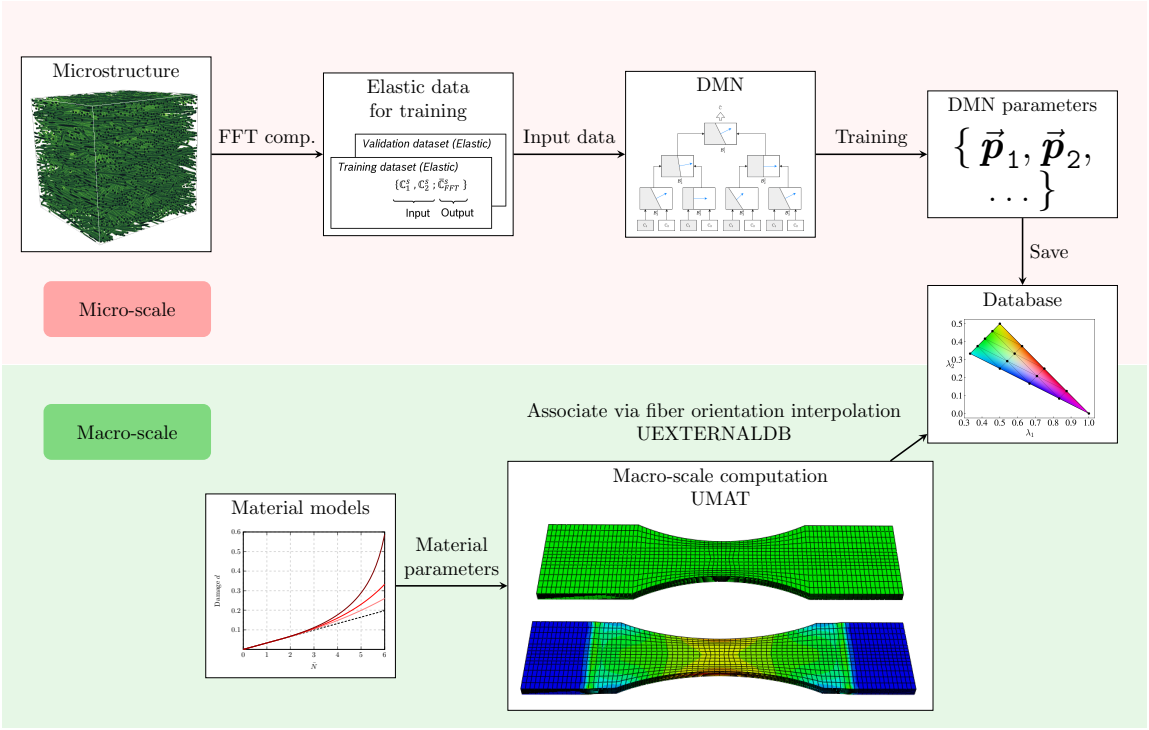

Figure 5.4: Multiscale FOT interpolation framework using DMNs adapted from Dey et al. [13, Fig. 4].

5.3 Identification of a DMN-based database for variable fiber orientations

5.3.1 Microstructural investigations

The constitutive laws of the constituents (fiber and matrix) as well as the spatial arrangement of the fibers in the matrix material influence the micromechanical problem. As such, the overall response of the composite is dependent on the material's representative microstructure. Several studies were conducted on the various important parameters of the microstructure (such as fiber length) and their influence on the material response in Dey et al. [12, § 4.1] for a polybutylene terephthalate (PBT) matrix, reinforced with 30% by weight E-glass fibers. The studies were conducted by comparing the experimental elastic response of the composite with the material response obtained using the FFT-based computational homogenization software FeelMath [133] with the help of virtual

microstructures generated using the SAM [127] algorithm. For more details, refer to Dey et al. [12, § 4.1].

In this work, we use the same composite as used in Dey et al. [12] to characterize the matrix material under high-cycle fatigue. Since the geometric descriptors are not affected by the loading conditions, we use the best calibrated microstructural parameters from Dey et al. [12] for generating training and validation data for the DMNs as well as for full-field FFT simulations for validations. Therefore, we generated cubic unit cells with an edge length of 625 μm, which includes cylindrical fibers having a length of 285 μm and diameter of 10 μm separated by a minimum distance of 3 μm. Each microstructure is discretized using 512^3 voxels, further resampled by a factor of two to 256^3 voxels using the composite voxel approach, see [130–132]. This strategy serves to accelerate the FFT computations with high fidelity, see Dey et al. [11, § 3.1]. All the microstructures are generated using the second order FOT along with the exact closure approximation [128, 129] which serves as an input for the SAM [127] algorithm. The second order FOT is calculated with the help of the eigenvalues λ_1 and λ_2 at each node of the triangle as shown in Fig. 5.3. It is also reported in Dey et al. [12] that a multi-layered microstructure over the thickness gives us better accuracy when compared to a single layer over the thickness. However, in this work, we circumvent the need to use a layered microstructure with the help of the FOT interpolation, where the layers are resolved in the macro-scale sample, see Section 5.4.1.

5.3.2 On the runtime of linear elastic full-field simulations

After the identification of the geometric descriptors, we are interested in the generation of training and validation data for the 15 DMNs populating the FOT triangle, see Fig. 5.3. This results in a large number of full-field FFT computations and thus reducing the runtime of the linear elastic full-field simulations is of paramount importance. We follow Dey et al. [11] and generate linear elastic training and validation data via the FFT-based computational homogenization software FeelMath [133] using the linear conjugate gradient method [135–137] and the staggered grid discretization [47, 134]. A detailed discussion on the different gradient-based methods for FFT computations and the respective convergence criterion can be found in Schneider et al [166].

The phase contrast of the constituents plays an important role in determining the runtime

of the full-field simulations. However, for the DMNs, we sample over a range of phase contrasts, which is a pre-requisite for good training of the DMN [70]. In this work, we design several numerical experiments using an extremely high phase contrast of 10,000 to evaluate the fidelity and computation time for the extreme case. We primarily check the accuracy and runtime of full-field FFT simulations dependent on the strain equivalence based and energy equivalence based residuals and their respective tolerances. The errors are evaluated using the Frobenius norm in Mandel notation with the help of a high-fidelity FFT computation which incorporates the energy equivalence based residual with a tolerance of 10^{-8}. In an automated process, all micromechanical computations were performed in parallel on a high performance computing cluster, where each full-field FFT computation uses 8 CPUs and 4 GB of memory per CPU.

Tolerance for residual	Unidirectional	Isotropic	Planar isotropic
10^{-5}	0.015%	6.2e-5%	9.9e-5%
10^{-4}	0.018%	8.9e-4%	1e-3%
10^{-3}	10.9%	12%	12.7%

Table 5.2: Relative error dependent on tolerance criterion using energy equivalence adapted from Dey et al. [13, Tab. 3].

Tolerance for residual	Unidirectional	Isotropic	Planar isotropic
10^{-5}	0.03%	1.3e-5%	2e-4%
10^{-4}	0.02%	1.7e-3%	1.5e-3%
10^{-3}	12.1%	12.8%	13.5%

Table 5.3: Relative error dependent on tolerance criterion using strain equivalence adapted from Dey et al. [13, Tab. 4].

We consider the three extreme fiber orientations separately, i.e., unidirectional, isotropic and planar isotropic fiber orientation as depicted in Fig. 5.2, and vary the tolerance for both energy equivalence and strain equivalence based residuals from 10^{-5} to 10^{-3}. The relative errors for all the three extreme fiber orientations compared to the respective high-fidelity solution are depicted in Tables 5.2 and 5.3 for the energy and strain equivalence

based residuals, respectively. The error increases as the tolerance increases for all microstructure realizations. However, the increase in error from a tolerance of 10^{-4} to 10^{-3} is rather large. The unidirectional orientation state has the highest errors. Moreover, the overall errors using the energy equivalence based residual appears to be lower than the strain equivalence based residual. This is consistent with the findings reported in Schneider et al. [167]. Therefore, for the linear elastic FFT computations we use the energy equivalence based residual with a tolerance of 10^{-4} which gives reasonable errors for all microstructure realizations with reduced runtime when compared to a tolerance of 10^{-5}. The computation times w.r.t. the tolerance for the extreme fiber orientation states are depicted in Fig. 5.5 which indicates that an increase in tolerance leads to a reduction in the computation time. We observe that the energy equivalence based residual with a tolerance of 10^{-4} reduces the computation time by a factor of two when compared to a tolerance of 10^{-5}, further justifying its use.

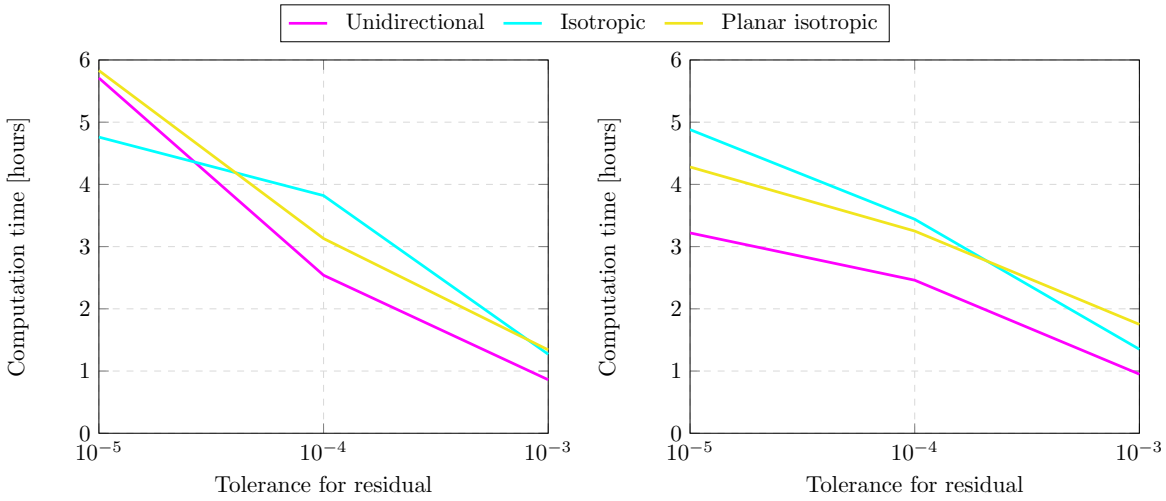

(a) Energy equivalence.

(b) Strain equivalence.

Figure 5.5: Computation times using different equivalence criteria and tolerances adapted from Dey et al. [13, Fig. 5].

5.3.3 Training the DMN database

In this work, we follow the approach outlined in Dey et al. [12, § 4.2] for training each of the 15 DMNs attached to the 15 nodes of the FOT triangle (see Fig. 5.3) based on the direct DMN framework [71] outlined in Section 5.2.2. For each DMN, the tuples $(\mathbb{C}_1^s, \mathbb{C}_2^s)$

were sampled using orthotropic elasticity tensors as outlined in Liu and Wu [70]. The effective elasticity tensor $\bar{\mathbb{C}}^s_{\mathtt{FFT}}$, computed using the workflow outlined in Section 5.3.2, completes the triples $\left(\mathbb{C}^s_1, \mathbb{C}^s_2, \bar{\mathbb{C}}^s_{\mathtt{FFT}}\right)$ used for training and validation. As a point of departure from previous works involving the direct DMN framework, we train each of the DMN on 400 training data points and further use 100 validation data points. Even for this comparatively low number of data points per DMN, already, a total of $500 \times 15 = 7500$ linear elastic FFT computations have to be performed for generating training and validation data.

A depth of seven was chosen for each DMN, i.e., each DMN consists of a binary tree of rotation-free laminates with seven levels. The increase in depth of the DMN increases the accuracy of the DMN in the online phase. However, the increase in accuracy is offset by the computation time in the online phase of the DMN. As the number of unknowns increases exponentially with the depth, the runtime increases exponentially with increase in depth, as well. Although the online phase computation of a shallower DMN is less time-consuming, a minimum depth of seven is required to evaluate highly non-linear load cases with sufficient fidelity.

The training proceeds to evaluate each of the DMN parameter sets $\vec{\boldsymbol{p}}_i$, where $i = 1, \ldots, 15$, for the 15 microstructural realizations denoted by the 15 nodes in the FOT triangle, see Fig. 5.3, by minimizing the objective function,

$$J(\vec{\boldsymbol{p}}_i) \longrightarrow \min_{\vec{\boldsymbol{p}}_i} \quad \text{with} \quad J(\vec{\boldsymbol{p}}_i) = \sum_{s=1}^{n_{\mathtt{b}}} J_s(\vec{\boldsymbol{p}}_i) + \Psi(\vec{\boldsymbol{p}}_i) \tag{5.3.1}$$

and the batch size $n_{\mathtt{b}} = 40$, where $\bar{\mathbb{C}}^s_{\mathtt{DMN}}(\vec{\boldsymbol{p}}_i)$ is evaluated as in Gajek et al. [71] and

$$J_s(\vec{\boldsymbol{p}}_i) = \frac{1}{n_{\mathtt{b}}} \frac{\left\| \bar{\mathbb{C}}^s_{\mathtt{FFT}} - \bar{\mathbb{C}}^s_{\mathtt{DMN}}(\vec{\boldsymbol{p}}_i) \right\|_1}{\left\| \bar{\mathbb{C}}^s_{\mathtt{FFT}} \right\|_1}. \tag{5.3.2}$$

The penalty term is defined as

$$\Psi(\vec{\boldsymbol{p}}_i) = \lambda \left(\mathbf{b}_1^T \langle \vec{\boldsymbol{v}}_i \rangle_+ - c_1 \right) + \lambda \left(\mathbf{b}_2^T \langle \vec{\boldsymbol{v}}_i \rangle_+ - c_2 \right), \tag{5.3.3}$$

where $c_1 = 0.822$ and $c_2 = 0.178$ are the volume fractions of the respective phases and $\vec{\boldsymbol{v}}_i$ are the vectors of unconstrained weights for each DMN as outlined in Dey et al. [11, eq. (2.21)]. In this case, $\mathbf{b}_1$ is a vector having ones at all odd indices and zero otherwise, and $\mathbf{b}_2$ is a vector having ones at all even indices and zero otherwise. The penalty factor λ is set to 100. The minimum of the objective function (5.3.1) is sought for training each DMN with a stochastic batch-gradient-descent approach based on automatic differentiation and

a batch size of 40. The entire database generation was automated using Python, the DMN framework was implemented using PyTorch [140] and trained with the help of the AMSGrad method [141]. The learning rate was modulated using cosine annealing [142],

$$\beta(m) = \beta_{\texttt{min}} + \frac{1}{2}(\beta_{\texttt{max}} - \beta_{\texttt{min}}) \left(1 + \cos\left(\pi \frac{m}{M}\right)\right), \tag{5.3.4}$$

where β and m denote the learning rate and epoch, respectively. The maximum learning rate is slightly increased to $\beta_{\texttt{max}} = 0.000725$ to compensate for training on a sparse dataset, when compared to the maximum learning rate of 0.0007 in Dey et al. [12]. The minimum learning rate is set to $\beta_{\texttt{min}} = 0$. The parameter M is set to 4000 and all the DMNs are trained up to 10 000 epochs.

Aiming for an extrapolation of the DMN online phase to long-term loading scenarios we augment the training approach with an inelastic input via an early-stopping procedure [11]. We follow the workflow laid down in Dey et al. [11] and use Hooke's law combined with a Norton-type creep law [78]

$$\begin{aligned} \boldsymbol{\sigma} &= \kappa \, \mathrm{tr}[\boldsymbol{\varepsilon}] \boldsymbol{1} + 2\mu \, \mathtt{dev}[\boldsymbol{\varepsilon} - \boldsymbol{\varepsilon}^{\mathrm{c}}], \\ \dot{\boldsymbol{\varepsilon}}^{c} &= \dot{\varepsilon}_0 (A_n \sqrt{3/2} \, \|\mathtt{dev}\, \boldsymbol{\sigma}\|)^{n_n} \frac{\mathtt{dev}[\boldsymbol{\sigma}]}{\|\mathtt{dev}[\boldsymbol{\sigma}]\|}, \end{aligned} \tag{5.3.5}$$

with creep parameters A_n and n_n, as a surrogate model to monitor the DMN performance every 50 epochs during training. For each microstructure realization, the full-field FFT computations using the Norton law and material parameters identified using the workflow specified in Dey et al. [11, § 3.3] and outlined in Table 5.4, are used as the ground truth.

Matrix	Elastic	$E = 2475.0$ MPa	$\nu = 0.4$	
	Creep	$A_n = 0.014$ 1/MPa	$n_n = 26.96$	$\dot{\varepsilon}_0 = 1.0$ s^{-1}

Table 5.4: Identified material parameters for the Norton-type model (5.3.5) adapted from Dey et al. [13, Tab. 5].

The DMN response is evaluated with the help of a single voxel microstructure by an FFT-based solver [133]. On the other hand, full-field simulations are performed using the microstructure realization attached to every node of the FOT triangle. In both cases, a uni-axial tensile stress of 60 MPa is applied, which is ramped up in 8.5 s and subsequently held constant for 8.64×10^4 s in the three principal directions denoted by $\bar{\sigma}_{ii}$ for $i = 1, 2, 3$. The creep strain component $\bar{\varepsilon}_{ii}$ in each loading direction is computed and the following

error measure is introduced to evaluate the performance of the DMN w.r.t the ground truth FFT computations

$$e^n_{ii,t} = \frac{\left|\bar{\varepsilon}^{\texttt{DMN,Norton}}_{ii,t} - \bar{\varepsilon}^{\texttt{FFT,Norton}}_{ii,t}\right|}{\max_\tau \left|\bar{\varepsilon}^{\texttt{FFT,Norton}}_{ii,\tau}\right|} \quad \text{for} \quad i = 1, 2, 3, \tag{5.3.6}$$

together the maximum errors

$$e^n_{ii} = \max_\tau e^n_{ii,\tau} \quad \text{as well as} \quad e^n = \max_{ii} e^n_{ii}, \tag{5.3.7}$$

where τ denotes the time steps.

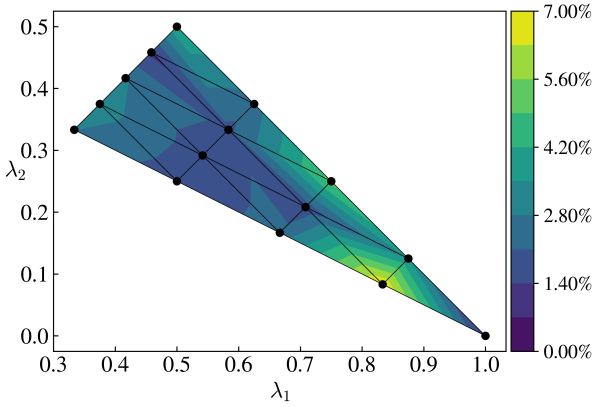

Figure 5.6: Maximum Norton error for a fiber orientation triangle with 15 nodes adapted from Dey et al. [13, Fig. 6].

The best DMN state $\vec{\boldsymbol{p}}_i$ for each microstructure realization is identified over the course of the training with the help of the best Norton error e^n. For a more detailed description of the training technique, we refer to Dey et al. [11, Alg. 1]. The best Norton error e^n for all the orientation states is shown in Fig 5.6. We observe the overall maximum errors throughout the FOT triangle remains fairly consistent around 4 %. The maximum value of the maximum Norton error is 6.9 % at a node near the unidirectional fiber orientation state. We also report on the loss value and the generalization capacity of this specific node having the maximum value of Norton error, shown in Fig 5.7. We observe a monotonic decrease of the loss for the first 100 epochs followed by oscillations, see Fig. 5.7(a).
The generalization capabilities of the DMN in the linear elastic offline phase are assessed with the help of a mean error

$$e_{\texttt{mean}} = \frac{1}{N_s} \sum_{s=1}^{N_s} e_s, \tag{5.3.8}$$

where

$$e_s = \frac{\left\| \bar{\mathbb{C}}^s_{\texttt{FFT}} - \bar{\mathbb{C}}^s_{\texttt{DMN}} \right\|_1}{\left\| \bar{\mathbb{C}}^s_{\texttt{FFT}} \right\|_1}, \tag{5.3.9}$$

and N_s is the number of samples in the training or the validation set, respectively. We see that the trend of the loss function corresponds to the mean training and validation errors, see Fig. 5.7(b). The simultaneous decrease in training and validation error during training is an indicator that there is no overfitting in the offline training phase.

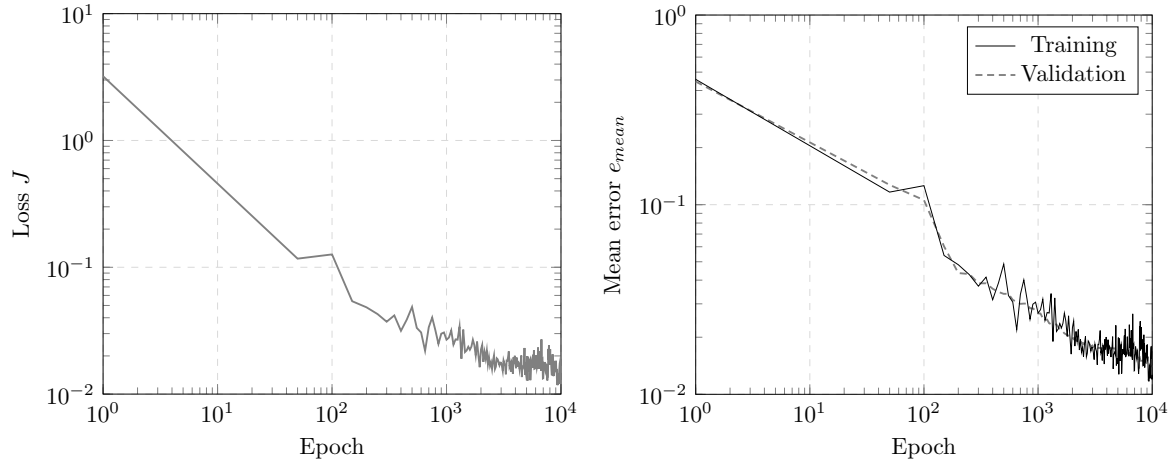

(a) Loss function.

(b) Mean error.

Figure 5.7: Offline training results for node with highest maximum Norton error adapted from Dey et al. [13, Fig. 7].

5.3.4 Validation of DMN database

Fatigue-damage model

Before deploying the DMN in a two-scale simulation, we focus on verifying the deep material network's predicted stress response. Firstly, we use the fatigue-damage model and parameters described in Section 5.2.1 as the constitutive model for the matrix and a linear elastic model for the fibers to check the fidelity of the trained DMN database. We compare the composite response under high-cycle fatigue using the DMNs for all 15 microstructure realizations at each node over the FOT triangle, see Fig. 5.3. Furthermore, to assess the predictive capabilities of the database outside the training domain we generate

microstructures at the centroids of all 16 sub-triangles, see Fig. 5.3. At these microstructure realizations, we interpolate the stress response from the nearby trained DMN states instead of directly computing it with the trained DMN as outlined in Section 5.2.3 and suggested by Köbler et al. [92]. However, this technique raises the effort by a factor of three, both in terms of computation time and memory use, because three DMN states must be examined for each macroscopic Gauss point.

We use the microstructure realizations generated using the SAM algorithm [127] at each node and centroid to evaluate the full-field FFT response using FeelMath [133]. The DMN response is evaluated using one tetrahedron element in Abaqus [120] with the help of the DMN online phase UMAT at each node and the fiber interpolation UMAT at every centroid. We subject the composite to cyclic loading with a constant stress amplitude and a stress ratio of $R = 0$, where

$$R = \frac{\sigma_{\texttt{min}}}{\sigma_{\texttt{max}}}. \tag{5.3.10}$$

To account for the anisotropic response, we instantaneously ramp up to a constant stress of 100 MPa till $\bar{N} = 6$, applied in 60 equidistant load steps for the three principal directions denoted by $\bar{\sigma}_{ii}$ where $i = 1, 2, 3$. We evaluate the strain $\bar{\varepsilon}_{ii}$ under high cycle fatigue in each direction. Similar to the Norton error, we introduce a fatigue error to evaluate the performance of the trained DMN states and the FOT interpolation w.r.t. the FFT computations,

$$e^f_{ii,t} = \frac{\left|\bar{\varepsilon}^{\texttt{DMN},f}_{ii,t} - \bar{\varepsilon}^{\texttt{FFT},f}_{ii,t}\right|}{\max_\tau \left|\bar{\varepsilon}^{\texttt{FFT},f}_{ii,\tau}\right|} \quad \text{for} \quad i = 1, 2, 3, \tag{5.3.11}$$

along with the maximum errors

$$e^f_{ii} = \max_\tau e^f_{ii,\tau} \quad \text{as well as} \quad e^f_{\texttt{max}} = \max_{ii} e^f_{ii}. \tag{5.3.12}$$

In addition, we introduce a mean error

$$e^f_{\texttt{mean}} = \max_{ii} \frac{1}{\tau} \int_0^T e^f_{ii,t} dt, \tag{5.3.13}$$

where $\tau = [0, T]$ denotes the time interval. The maximum (5.3.12) and mean (5.3.13) errors are evaluated at all centroids and nodes and are plotted in Fig. 5.8 over the FOT triangle.

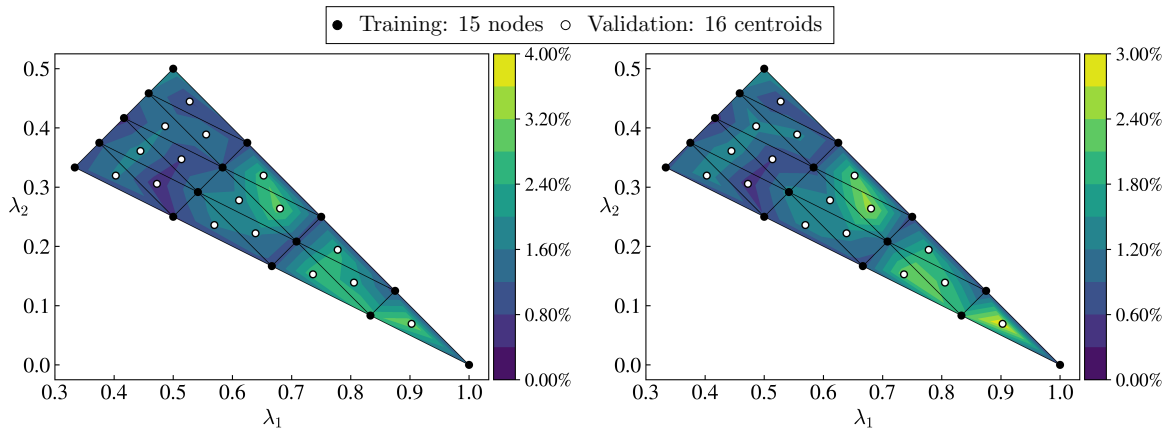

(a) Maximum error $e^f_{\texttt{max}}$.

(b) Mean error $e^f_{\texttt{mean}}$.

Figure 5.8: Maximum and mean error for fiber orientation interpolation under high cycle fatigue adapted from Dey et al. [13, Fig. 8].

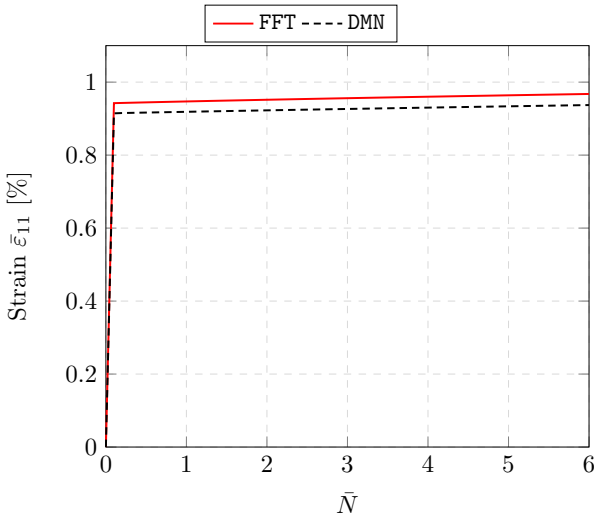

Figure 5.9: Comparison of DMN and full-field results under high-cycle fatigue for node having the worst maximum error over the FOT triangle adapted from Dey et al. [13, Fig. 9].

We observe that the maximum error and the mean errors over the complete FOT triangle lie below 4 % and 3%, respectively. The errors observed at the nodes where the DMNs are trained are slightly lower compared to the interpolated centroids. This is in accordance with the MOR-based fiber orientation interpolation outlined in Magino et al. [93, § 4.3.4]. However, in our case the maximum error at the nodes are around 2 % which is several

magnitudes higher than the MOR-based system. This is to be expected since the DMN is a more general approach which only learns the spatial geometry in contrast to the MOR approach [93] where the nodes are trained on modes of the specific loading paths. Nevertheless, the maximum interpolated errors at the centroids of the triangle using the DMNs are slightly lower when compared to the maximum errors of 5 % for the MOR-based system [93]. In this work, the maximum error of 3.14 % over the entire FOT triangle is observed under extension in the 11-direction at a centroid having eigenvalues $\lambda_1 = 0.9$ and $\lambda_2 = 0.07$. The comparison of the DMN and full-field results for this specific load case is shown in Fig. 5.9.

Coupled plasticity and creep model

We additionally validate the performance of the DMN and the fiber orientation interpolation with the help of the plasticity and creep coupled law for the matrix material described in Section 4.2.3, along with the material parameters outlined in Table 4.11. The model can represent both plasticity and creep at different time scales. We start with the plasticity and introduce the maximum relative elasto-plastic error $e^p_{\texttt{max}}$ [11, eq. 3.9], following Dey et al. [11]. The loading conditions and simulation workflows are the same as used in Dey et al. [11]. Furthermore, we introduce a mean error similar to the fatigue loading scenario,

$$e^p_{\texttt{mean}} = \max_{ij} \frac{1}{\tau} \int_0^T e^p_{ij,t} dt, \tag{5.3.14}$$

where

$$e^p_{ij,t} = \frac{\left|\bar{\sigma}^{\texttt{DMN}}_{ij,t} - \bar{\sigma}^{\texttt{FFT}}_{ij,t}\right|}{\max_\tau \left|\bar{\sigma}^{\texttt{FFT}}_{ij,\tau}\right|}. \tag{5.3.15}$$

The errors are plotted over the FOT triangle in Fig. 5.10.

The maximum elasto-plastic error is observed to be 11.6 % under uni-axial extension in 11-direction in the uni-directional microstructure realization, see Fig. 5.12(a). The representation of the elasto-plastic response of the uni-directional microstructure realization, using the DMN, appears difficult and is also observed in Gajek et al. [72]. The overall maximum error remains fairly consistent over the FOT triangle. More fluctuations can be observed in the mean error with a maximum value below 5 %, see Fig. 5.10(b).

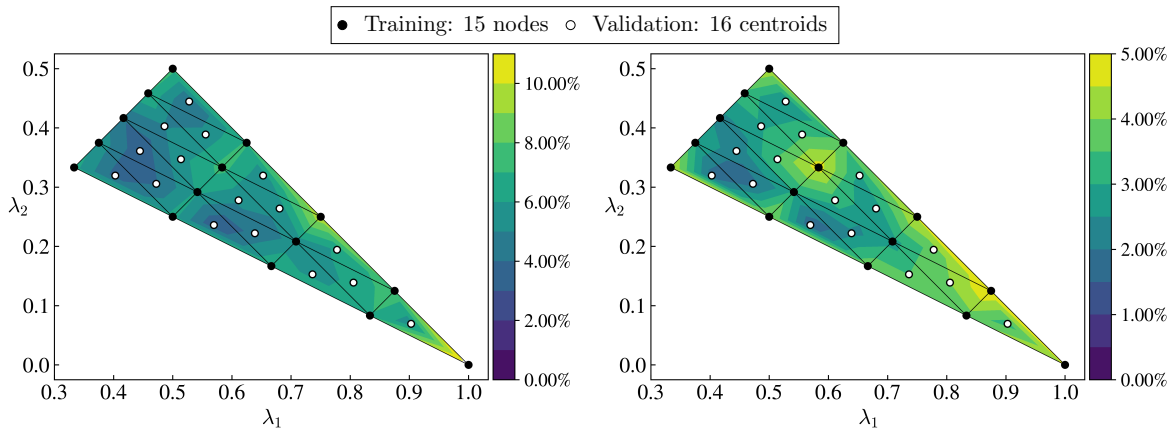

(a) Maximum error $e^p_{\texttt{max}}$. (b) Mean error $e^p_{\texttt{mean}}$.

Figure 5.10: Maximum and mean error for fiber orientation interpolation under elasto-plastic loading adapted from Dey et al. [13, Fig. 10].

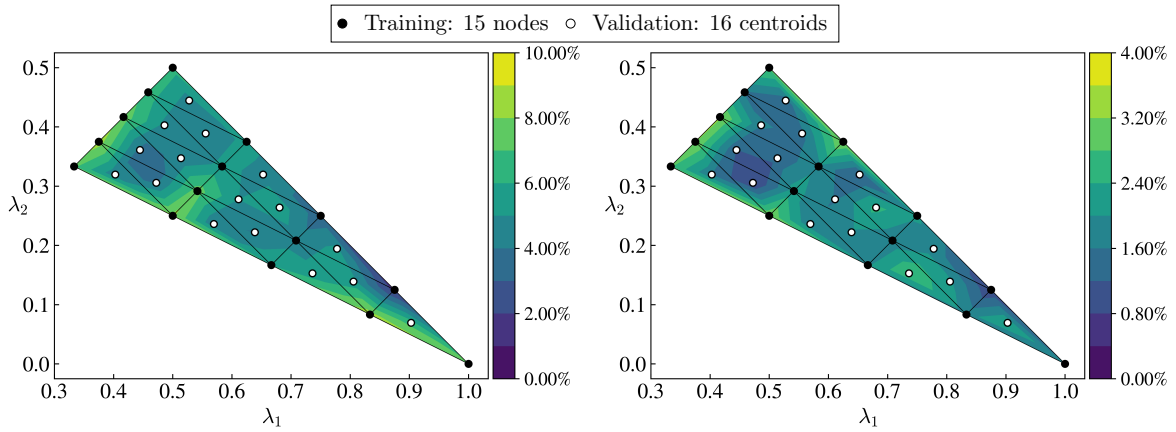

(a) Maximum error $e^c_{\texttt{max}}$. (b) Mean error $e^c_{\texttt{mean}}$.

Figure 5.11: Maximum and mean error for fiber orientation interpolation under creep loading adapted from Dey et al. [13, Fig. 11].

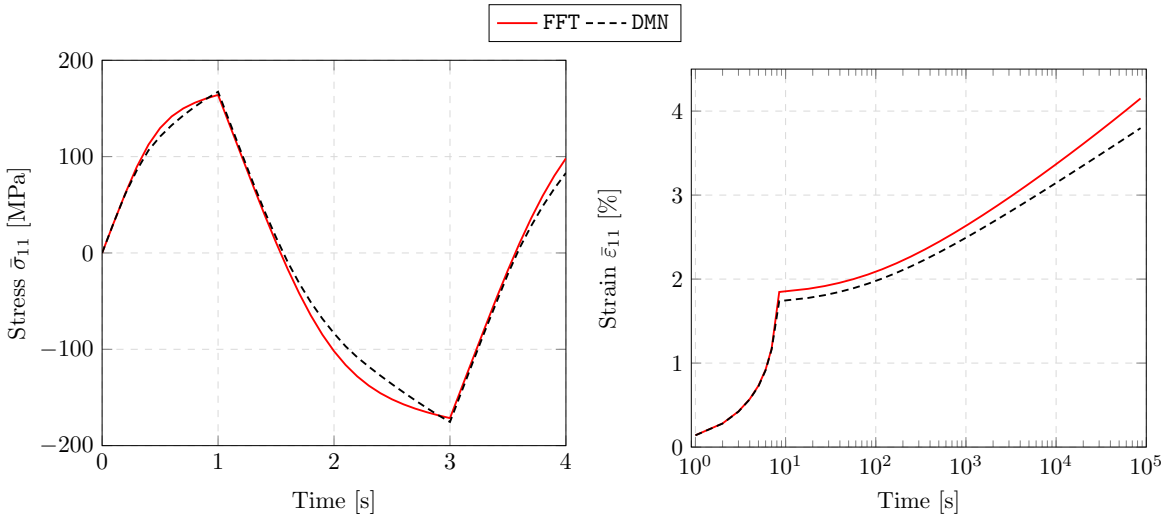

(a) Uniaxial extension in 11-direction.

(b) Creep strain in 11 direction.

Figure 5.12: Comparison of DMN and full-field simulation for elasto-plasticity and creep for node having the worst maximum errors over the FOT triangle adapted from Dey et al. [13, Fig. 12].

The loading conditions for the validation of the creep response are similar to the ones introduced for the Norton error in Section 5.3.3. At every node, a uni-axial tensile stress of 60 MPa is applied, which is ramped up in 8.5 s and subsequently held constant for 8.64×10^4 s in the three principal directions denoted by $\bar{\sigma}_{ii}$ where $i = 1, 2, 3$. However, at nodes where λ_1 has a value greater than 0.6, the uni-axial tensile stress is reduced to 30 MPa in the 22 and 33-directions. In the case of all centroids, a uni-axial tensile stress of 40 MPa is used in all directions. The maximum and mean error for computing the DMN and full-field response using the creep strain component $\bar{\varepsilon}_{ii}$ is introduced

$$e^c_{\texttt{max}} = \max_{ii} \max_{\tau} e^c_{ii,\tau} \quad \text{and} \quad e^c_{\texttt{mean}} = \max_{ii} \frac{1}{\tau} \int_0^T e^c_{ii,t} dt, \tag{5.3.16}$$

respectively, where

$$e^c_{ii,t} = \frac{\left|\bar{\varepsilon}^{\texttt{DMN,c}}_{ii,t} - \bar{\varepsilon}^{\texttt{FFT,c}}_{ii,t}\right|}{\max_\tau \left|\bar{\varepsilon}^{\texttt{FFT,c}}_{ii,\tau}\right|} \quad \text{for} \quad i = 1, 2, 3. \tag{5.3.17}$$

The maximum and mean error for the FOT triangle under creep loading is shown in Fig. 5.11. The maximum errors do not show any major fluctuations with a maximum value of 8.5 % in the 11-direction at a node near the isotropic fiber orientation state. The FFT and DMN responses for the maximum error are visualized in Fig. 5.12(b).

The overall maximum errors for creep appear to be higher than the errors reported in Dey et al. [11]. A probable cause is the use of fewer training data points in this work. However, the mean errors show very little fluctuations and are below 4 %, see Fig. 5.11(b).

5.3.5 Computation time

Finally, we discuss the computational cost of the deep material network based fiber orientation interpolation and compare it to the MOR-based fiber orientation interpolation [93]. To this effect, we use an Abaqus [120] tetrahedron element simulation containing one Gauss point which we run on a single node having a single CPU. We apply a uniaxial load of 100 MPa for $\bar{N} = 6$ in 60 equidistant load steps. The fiber orientation concept based on DMNs requires 27 ms for solving the material law at the Gauss point for a prescribed macro increment in the logarithmic cycle space. It is to be noted that at every Gauss point, three separate DMNs need to be evaluated for finding the interpolated material response. On the other hand, the MOR-based approach using 15 proper orthogonal decomposition modes for the reduced-order model from Magino et al. [93] requires around 2.4 ms for identifying the material response at the Gauss point for a prescribed macro increment in the logarithmic cycle space.
Therefore, the computational cost is increased by a factor of around 10 when using individually trained DMNs for fiber orientation interpolation. Nevertheless, the versatility of the DMN makes it an attractive choice. The trained DMNs can not only model the fatigue response with high fidelity but also the plasticity-creep response as shown in Section 5.3.4. This is unlike the MOR-based approach which is configured for predicting the fatigue response only. Moreover, the decoupling of the material response of the constituents from the geometric state, in the DMN response, opens a vast array of opportunities to modify existing material models and parameterize them based on the composite response.

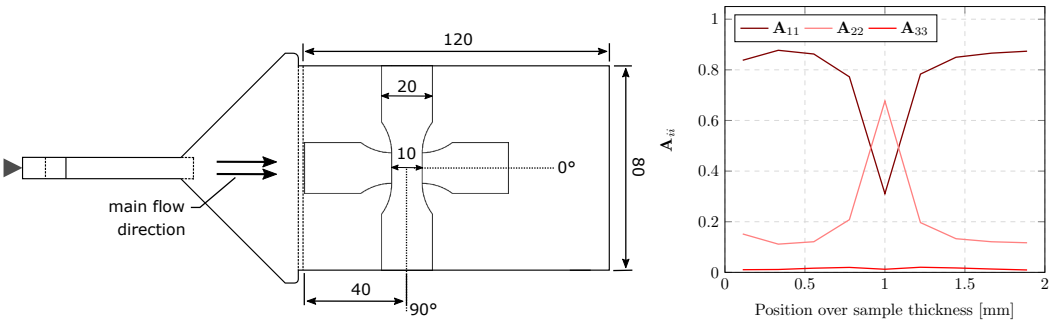

(a) Specimen geometry having thickness of 2 mm prepared from an injection molded plate.

(b) Fiber orientation over layers.

Figure 5.13: Geometry and fiber orientation of the sample adapted from Magino et al. [97].

5.4 Extension of fatigue-damage model

5.4.1 Experimental investigations

The stiffness degradation under fatigue loading for fiber-reinforced polymers are investigated with the help of experiments performed using the reinforced PBT composite [97]. The experiments were performed on samples cut out from an injection molded plate. We use the samples cut out in the 0° and 90° direction w.r.t. the flow direction during injection molding as shown in Fig. 5.13(a). The layered fiber orientation tensor over the thickness of the sample was extracted from μCT scans performed using a small volume of the identified samples [7]. The FOT using nine layers over the thickness of the sample is depicted in Fig. 5.13(b) [97].

Both the samples were subjected to cyclic loading with a stress ratio of $R = 0$ using a range of stress amplitudes [97]. Moreover, the experiment for each load case was repeated three times to determine the variation of the measurements [97]. The decrease of dynamic stiffness of the material under fatigue loading is of interest to us. As a result, for each cycle, we recorded the maximum strain $\varepsilon_{\mathtt{max}}$ and the minimum strain $\varepsilon_{\mathtt{min}}$. Finally, the dynamic stiffness of the sample is calculated,

$$E_{\text{dyn}} = \frac{\sigma_{\mathtt{max}} - \sigma_{\mathtt{min}}}{\varepsilon_{\mathtt{max}} - \varepsilon_{\mathtt{min}}}. \tag{5.4.1}$$

The experiments corresponding to each stress level are conducted at different frequencies. This was done to study the viscoelastic effect of the composite on the stiffness degradation, see Magino et al. [97]. However, in this work, the viscoelastic effects are not taken in account during the modeling approach. Therefore, we normalize the dynamic stiffness using the initial dynamic Young's modulus of the sample at $\bar{N} = 0$, $E_{\text{dyn}}(0)$. We plot the normalized dynamic stiffness against the logarithmic cyclic variable $\bar{N}$ for different stress amplitudes in the 0° and 90° directions in Fig. 5.14.

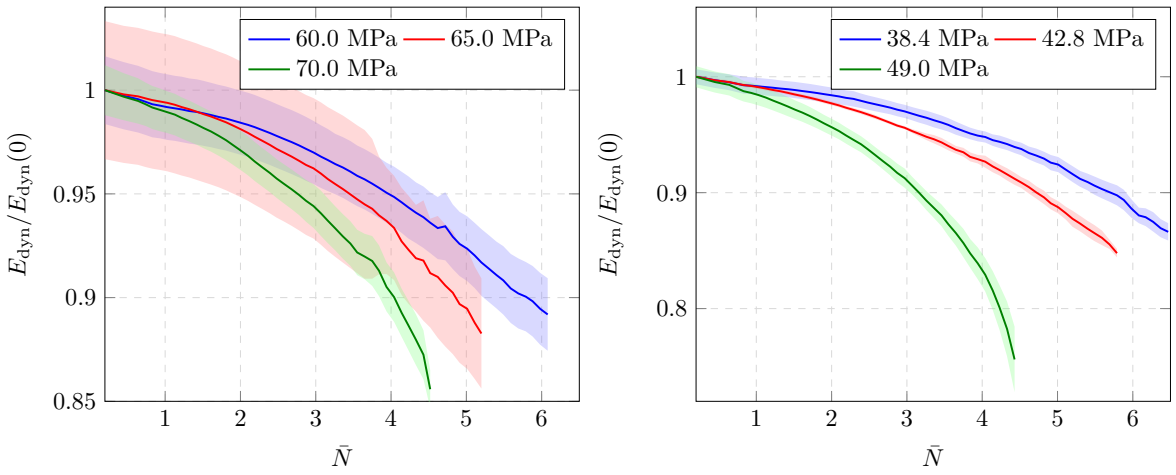

(a) 0° direction.

(b) 90° direction.

Figure 5.14: Stiffness degradation under high-cycle fatigue loading adapted from Dey et al. [13, Fig. 14].

At first glance, it can be seen that the scattering of the experiments is significantly higher in the 0° direction when compared to the 90° direction, see Figs. 5.14(a)and 5.14(b). Moreover, the stiffness degradation in both directions show a steady linear decrease up to around $\bar{N} = 2$, i.e., in the primary stage. However, after 100 cycles, i.e., secondary stage and beyond, the stiffness degradations due to fatigue-damage shows a strongly non-linear response. Hence, it was clear to us that the elegant fatigue-damage model for the matrix, formulated using a linear damage evolution, in Magino et al. [93] (Section 5.2.1) is not sufficient to fully represent the highly non-linear stiffness degradation of the composite material. Therefore, in the following section, we introduce a novel fatigue-damage model for the matrix material, based on a non-linear damage evolution, and seek a better fit to the composite experiments shown in Fig. 5.14.

5.4.2 Power-law fatigue-damage model

In this section, we extend the fatigue-damage model with a linear damage evolution, proposed in Magino et al. [93] and briefly outlined in Section 5.2.1. We follow the approach from Magino et al. [93] and formulate the model in the logarithmic cycle space denoted by a continuous positive variable $\bar{N}$. Furthermore, the improved power-law fatigue-damage model is defined in the GSM setting [101] and can be directly integrated in the DMN framework.

We use the free energy density of the model defined in eq. (5.2.1), with the help of the macroscopic strain tensor $\boldsymbol{\varepsilon}$, the initial fourth-order stiffness tensor $\mathbb{C}$ and a positive scalar damage variable d, which serves as the internal variable. The stress is thereby computed as defined in eq. 5.2.2. However, we formulate a new dissipation potential, dependent not only on the damage evolution $d' = \mathrm{d}d/\mathrm{d}\bar{N}$ as in eq. (5.2.3), but also on the damage variable d and formulated in the GSM framework as

$$\phi(d', d) = \frac{1}{2\alpha\left(1 + A\left\langle d - d_{\mathtt{crit}}\right\rangle_{+}\right)^{n}}(d')^2, \tag{5.4.2}$$

in terms of the parameter α controlling the speed at which damage evolves, a critical damage value $d_{\mathtt{crit}}$, a pre-factor A and an exponent n.

Finally, the evolution of the internal variable d obtained using the Biot's equation associated to this specific model, in an explicit form, is defined as

$$d' = \frac{\alpha\left(1 + A\left\langle d - d_{\mathtt{crit}}\right\rangle_{+}\right)^{n}}{2(1+d)^2}\,\boldsymbol{\varepsilon} : \mathbb{C} : \boldsymbol{\varepsilon}, \tag{5.4.3}$$

where the damage variable d increases in a linear fashion over the logarithmic cycle space $\bar{N}$ up to $d \leq d_{\mathtt{crit}}$, if the stress amplitude is prescribed. In the case when the damage variable $d > d_{\mathtt{crit}}$, the damage evolution is scaled based on a power-law which is dependent on the exponent n, the remaining damage $d - d_{\mathtt{crit}}$ and the pre-factor A. This condition is encoded in the model with the help of the Macauley bracket

$$\left\langle d - d_{\mathtt{crit}}\right\rangle_{+} = \max(0, d - d_{\mathtt{crit}}). \tag{5.4.4}$$

The evolution equation (5.4.3) is discretized using an implicit setting in the logarithmic cycle space. The fatigue-damage model with the linear damage evolution, defined in eq. (5.2.4), can be obtained by setting the parameter $A = 0$ in the non-linear damage evolution (5.4.3).

We aim to understand the damage evolution of the non-linear model in detail with the help of a uniaxial extension in a one-dimensional setting under a constant stress amplitude $\sigma_{\mathtt{max}}$ of 30 MPa. Moreover, we consider the evolution of the dynamic stiffness $E_{\mathtt{eff}}$ with an initial value of 3 GPa. The exact integration of the damage evolution (5.4.3) under a constant stress amplitude and initial condition of $d(0) = 0$ is plotted in Fig. 5.15(a) for different values of the exponent n. We assign the pre-factor A and α a value of 2 and 0.11, respectively, and the non-linear evolution starts when the damage reaches a critical value $d_{\mathtt{crit}} = 0.05$. We also compare the non-linear response with the linear response where we set the parameter A to zero. We observe that the parameter α determines the initial slope of the damage evolution which remains constant up to $\bar{N} = 6$ in the linear case ($A = 0$). However, in the non-linear case ($A = 2$), the damage evolution progresses exponentially when the damage variable d reaches the critical damage $d_{\mathtt{crit}}$. The damage evolution is stronger with increase in the value of exponent n, see Fig. 5.15(a). We also plot the effective dynamic stiffness $E_{\mathtt{eff}}$ degradation defined as

$$E_{\mathtt{eff}} = \frac{1}{1+d} E \tag{5.4.5}$$

over the logarithmic cycle variable $\bar{N}$ normalized with the elastic modulus E, which equals the effective stiffness in the undamaged initial state, in Fig. 5.15(b). We see that the slope of the curve remains constant for the linear case ($A = 0$) and the effective Young's modulus decreases due to the damage under fatigue loading. Nevertheless, in the non-linear case ($A = 2$), we observe a behavior corresponding to the damage evolution, where the rate of stiffness degradation increases after the critical damage threshold is reached and is dependent on the value of exponent n. Thus, for a higher number of cycles, the stiffness degradation is sped up and reproduces the stiffness degradation observed in the experiments performed on the composite rather well, see Fig. 5.14. Therefore, the improved matrix model, incorporating non-linear power-law damage evolution under high-cycle fatigue, should in principle be able to better reproduce the composite experiments depicted in Fig. 5.14.

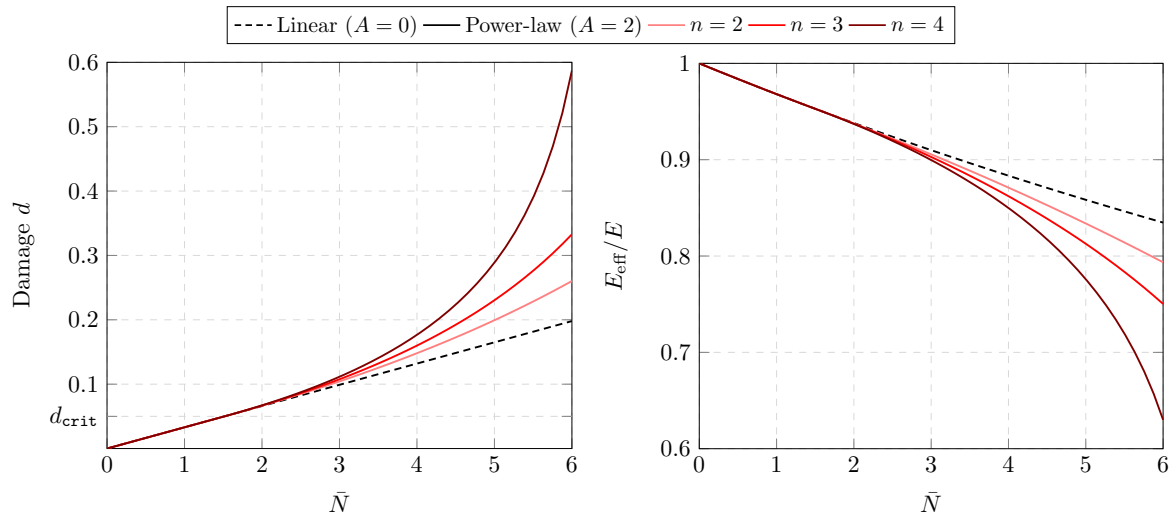

(a) Non-linear evolution of fatigue damage. (b) Evolution of effective dynamic stiffness.

Figure 5.15: Effect of changing the exponent n on the non-linear polymer matrix behavior adapted from Dey et al. [13, Fig. 15].

5.4.3 Inverse calibration of power-law fatigue-damage model

Exploiting the additional freedom enabled by the power-law fatigue-damage model, proposed in Section 5.4.2, requires identifying three new parameters $d_{\mathtt{crit}}$, A and n in addition to the two parameters of the linear model (Section 5.2.1) E and α. These five parameters need to be calibrated using experimental results. The inverse calibration approach introduced in Dey et al. [12, Fig. 1] enables us to efficiently calibrate all the parameters directly from composite experiments, see Fig. 5.14.

However, in contrast to Dey et al. [12], instead of using a single element computation in Abaqus [120] for the inverse calibration, we use the complete sample shown in Fig. 5.13(a) by leveraging the FOT interpolation introduced in Section 5.2.3. We observe, in the fatigue testing sample, a slight stress intensity factor rendering the macroscopic response slightly inhomogeneous. Therefore, the structural simulation of the full geometry is deemed necessary. We assign a nine-layered fiber orientation structure to the macroscopic sample depicted in Fig. 5.13(b). Each element in the sample is assigned the respective orientation state and the material response can be efficiently computed using the trained DMNs attached to the three closest orientation states via the fiber orientation interpolation, see Section 5.2.3. Therefore, the trained DMN database over the FOT triangle has

a two-fold advantage. In addition to enabling the evaluation of the material response at any orientation state, the model-free nature of the DMN permits us to inversely calibrate matrix properties from a single set of composite experiments.

In our case, we calibrate the power-law fatigue-damage model for the matrix, introduced in Section 5.4.2, based on composite experiments performed in the 0° direction. The inverse calibration is performed in two distinct steps. In the first step, we calibrate the model based on linear damage evolution by setting the parameter A to 0 and optimizing with the experiments performed in the 0° direction up to a normalized dynamic stiffness value of 0.98. This is the primary stage of the stiffness degradation under fatigue loading which can be described by a linear model. We aim to find the Young's modulus E and the damage-speed parameter α and consider a fixed Poisson's ratio $\nu = 0.4$. The macroscopic sample is evaluated in Abaqus [120] and the simulation is iteratively called in an OptiSlang [119] optimization workflow. We simulate the fatigue loading with three different stress amplitudes with a stress ratio $R = 0$. We set up a minimization problem wherein the area under the normalized dynamic stiffness curve obtained from the composite experiment and from the simulation using the macroscopic sample is considered for each stress level. The objective function minimizes the sum of the areas for the three stress amplitudes.

We use the One-Click-Optimization (OCO) algorithm in OptiSlang [119] and generate 100 samples of the parameters using Latin Hypercube Sampling (LHS) [155]. The best fitting parameters, stored in Table 5.5, are obtained when the objective function reaches a minimum value of 0.5%. The plots comparing the composite experiments and the simulations using the linear damage with the best fitting parameters is shown in Fig. 5.16. We observe that the linear model represents the stiffness degradation of the composite experiments in the primary stage to a reasonable accuracy. The inverse parameter approach also results in higher values of the Young's modulus E when compared to the Young's modulus obtained using experiments from the matrix material [93], see Table 5.1.

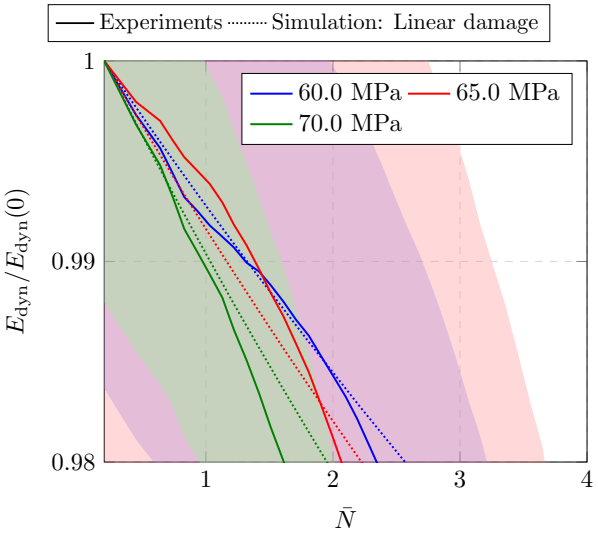

Figure 5.16: Experimental and simulation results with best fitting parameters in 0° direction using linear damage evolution adapted from Dey et al. [13, Fig. 16].

In the next step, we fix the identified linear-damage parameters and aim to find the parameters for the non-linear power-law damage evolution. We follow a similar approach like the linear damage but now we use the complete experimental stiffness degradation of the composite in the 0° direction for three different stress amplitudes, see Fig. 5.14(a). We again use the same optimization and objective function in OptiSlang [119] and find the best fitting parameters using 100 LHS parameter sets. The best fitting parameters, reported in Table 5.5, were found with a minimum value of the objective function of 11.6 %. The composite experiments in the 0° direction are plotted against the best fitting simulation using both the linear and power-law damage evolution in Fig. 5.17(a). We find that the power-law damage evolution can better model the stiffness degradation under fatigue. This is mainly because the rate of stiffness degradation remains fixed in the case of linear damage evolution, and it can model the stiffness degradation up to 100 cycles or primary stage only, with reasonably accuracy. On the other hand, the power-law damage evolution can predict the stiffness degradation within the scattering of the experiment for the entire logarithmic cycle window for the lower stress amplitudes. In case of the maximum stress amplitude of 70 MPa, the stiffness degradation beyond 10,000 cycles is not well represented since the model does not account for localizing effects.
Furthermore, the best fitting parameters are used to simulate the composite experiments at different stress amplitudes in the 90° direction, see Fig. 5.17(b), to validate

the anisotropic response. As in the 0° direction, we observe that the power-law damage evolution provides a better fit compared to the linear case for all stress amplitudes. However, in the 90° direction the fit is worse when compared to the 0° direction. A possible reason might be that the localization effects are stronger in the 90° direction since the composite is weaker, especially for higher stress amplitudes. Nevertheless, the power-law fatigue-damage model introduced in Section 5.4.2 fits the composite experiments in both 0° and 90° directions with reasonable fidelity when compared to the matrix model with linear damage evolution introduced in Magino et al. [93]. Therefore, the FOT interpolation based on the DMNs allow us not only to extend or modify material laws of the constituents but also enable us to efficiently identify the material parameters with a reduced number of experiments via inverse calibration.

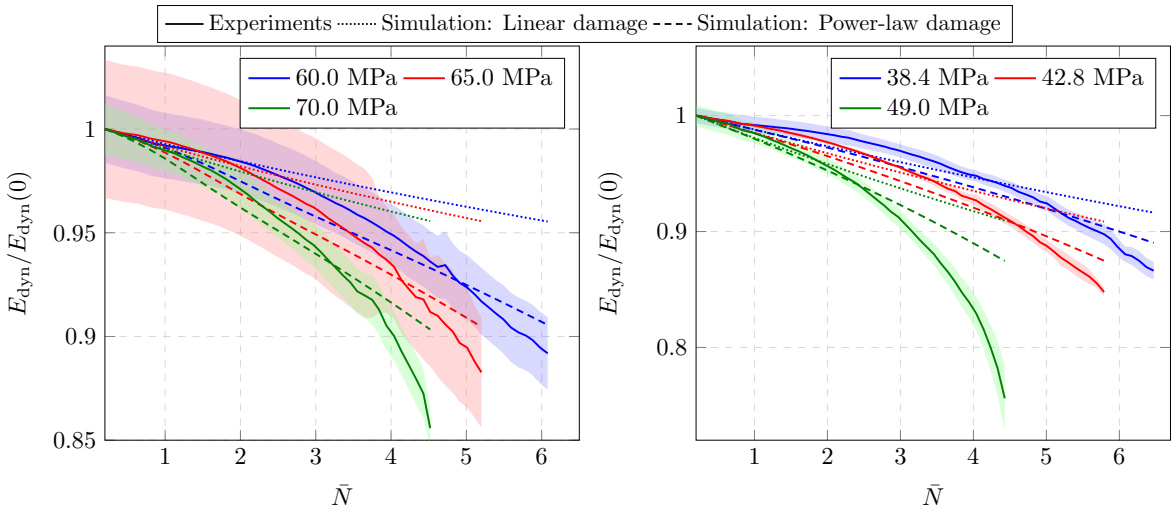

(a) 0° direction - Optimized.

(b) 90° direction - Predicted.

Figure 5.17: Experimental and simulation results with best fitting parameters under high-cycle fatigue adapted from Dey et al. [13, Fig. 17].

5.5 Conclusion

In the work at hand, we consider the problem of multi-scale modeling of short fiber reinforced thermoplastics for all possible orientation states under long-term loading using the

Matrix	Elastic	$E = 2871.5$ MPa	$\nu = 0.4$	
	Damage (Linear)	$\alpha = 0.07$ 1/MPa		
	Damage (Power-law)	$d_{\texttt{crit}} = 0.06$	$A = 4$	$n = 1.4$

Table 5.5: Matrix parameters for fatigue loading identified with inverse calibration of the composite experiments adapted from Dey et al. [13, Tab. 6].

DMNs as a surrogate for the micro-scale. This is in contrast to FE^2 approaches where each Gauss point in the macro-scale finite element simulation is equipped with a finite element model of the microstructure that is used to solve the cell problem. Although the FE^2 method delivers accurate results, it is computationally expensive, especially when the microstructure definition varies in the macro-scale. In this regard, MOR-based approaches are computationally efficient. However, there exists a trade-off in the numerical performance when selecting the proper quadrature essential for accuracy [168, 169]. Magino et al. [93] uses specific material models to circumvent the quadrature problem, which in turn restricts modeling freedom. Nevertheless, one of the major drawbacks of the MOR approach is that any further change in the constitutive model requires a re-calibration of the complete micro-scale approach.

We are interested in a more general approach where the matrix model for fatigue-damage can be modified and tuned based on performance at the composite level. The DMNs offer us an efficient surrogate for micromechanics and is able to model the inelastic composite response for a variety of design tasks. Several works [72, 74, 76] have introduced upscaling techniques by training/re-training a single DMN a priori over an array of microstructural descriptors. However, with a view to long-term load cases such as fatigue or creep [11], we use the fiber orientation interpolation introduced in Köbler et al. [92] and train multiple DMNs over the complete FOT triangle for the a posteriori evaluation of the composite response. We integrate the fatigue-damage model introduced in Magino et al. [93] in the FOT interpolation framework and validate the composite response for all possible orientation states with the help of full-field FFT response. We demonstrate the generalizability of the DMN-based FOT interpolation by integrating and validating the system with a coupled plasticity-creep law [12]. We show that the trained DMN database can reproduce the composite response for fatigue, quasi-static and creep load cases simultaneously with a reasonable fidelity.

Finally, we critically examine the stiffness degradation of the composite based on experi-

mental results. We find that after a few hundred cycles (primary stage) the stiffness degradation becomes strongly non-linear in nature. Therefore, we introduce an improved matrix model with a non-linear power-law damage evolution for modeling fatigue of SFRTs. We circumvent the drawback of re-calibrating the multi-scale workflow imposed by the MOR-based approach [93] with the DMN based approach. The DMNs decouple the constitutive model of the constituents from the geometric state. Thus, we integrate the power-law fatigue-damage model into the DMN-based multi-scale framework with minimum effort. We inversely calibrate [12] the power-law fatigue-damage model for the matrix based on composite experiments and demonstrate that this model enables us to better fit the stiffness degradation beyond the primary stage. Nevertheless, the modeling of the stiffness degradation in the tertiary stage before failure will be better served with a localizing approach.

The DMN framework coupled with the FOT interpolation framework from Köbler et al. [92] creates an off-the-shelf all-inclusive database for calibrating the composite response for all possible orientation states under a range of load cases. This framework can also be used for component simulation with a varying spatial response, albeit with further speed-up using sparse matrices in the DMN online phase [72] creating a one-stop solution for multi-scale modeling of SFRTs. Furthermore, extending the database framework for interpolation over other geometric descriptors such as fiber length and capturing the uncertainties arising out of the microstructure [74] may also be worth the effort.

6 Conclusion

The main contribution of this thesis is the development of a complete multi-scale virtual characterization workflow for SFRTs under long-term load cases such as creep and fatigue. The virtual characterization results in the saving of both time and resources. The micromechanical solution is accelerated by using the direct DMN framework introduced in the Ph.D. thesis of Sebastian Gajek [10] which gives us several orders of speed-up when compared to full-field FFT approaches with reasonable fidelity. The inverse calibration approach introduced with the help of DMNs enables us to calibrate the material models directly from a single set of composite experiments. This is especially useful in long-term loading since, with a traditional forward calibration approach, multiple experiments need to be performed on the pure matrix and also the composite. Each experimental procedure often lasts weeks and is resource intensive.

In Chapter 3, we developed the basis of the thesis, wherein we introduce the deep material networks which, in principle, act as a high-level surrogate for a finite element discretization of an N-phase microstructure. Furthermore, we critically discuss the shortcomings of the elasticity-based training of DMNs when a high degree of nonlinearity and rather larger time scales are involved. We offered (more or less clear) instances of DMNs that fail to generalize from linear elasticity to creep, in this work. We devised a solution for this problem based on the early-stopping approach, which is common in deep learning, wherein we provide an inelastic input to the elasticity-based training. We provided evidence that such a strategy yields predictable and trustworthy training outcomes for DMNs, allowing them to be employed confidently in the case of long-term loading.

With the DMN framework for the micromechanical solution ready, we introduce a fully coupled-plasticity and creep model for the matrix material in Chapter 4. We show, with the help of experimental results, that this novel model can reproduce both plasticity and creep at different timescales for the pure matrix. However, the calibration of the material model to the composite experiments is necessary for the complete virtual characterization.

Herein, we use the DMN framework to design an inverse calibration workflow identifying the parameters for the constitutive model (in our case, a fully coupled plasticity-creep law) of the polymer matrix by experiments performed on the composite. We demonstrated that such a method can effectively identify material properties from composite experiments and accurately reflect the anisotropic response of the composite. Due to the longer runtime of full-filed simulations when compared to DMN simulations, such a technique using typical FFT computations would be a daunting task.

We extend the DMN framework to model the stiffness degradation under fatigue loading using a linear fatigue-damage law for the matrix in Chapter 5. Furthermore, aiming at a generalized approach where the material response under long-term loading can be predicted for a variety of microstructure states, we use the fiber orientation interpolation concept introduced in Köbler et al. [92] and train multiple DMNs over the complete FOT triangle for the a posteriori evaluation of the composite response. We test this approach with the help of full-field simulation for both fatigue and creep loading. Moreover, we leverage the model-free nature of the DMN to further tune the fatigue law using a power-law component with the help of experiments performed on the composite. Therefore, we demonstrate the usability of the DMN framework coupled with the FOT interpolation where we can calibrate multiple material models for all possible orientation states.

In this thesis, we created an off-the-shelf all-inclusive database based on the direct DMN framework for the virtual characterization of SFRTs under creep and fatigue loading. However, it is to be mentioned that the complete fracture of the component cannot be predicted since it is not exactly clear whether DMNs work for softening. Moreover, in the case of DMNs for long-term loading, we used an early-stopping strategy since evaluating the nonlinear constitutive law in the objective function is expensive. It is unclear whether there is a flaw in the linear elasticity-based training itself, or whether a judicious selection of sampled stiffnesses or correctly constructed loss functions could fix the problem.

We use a linear elastic model for the fiber without considering fiber breakage. However, in case of SFRTs, experiments show fiber breakage under long-term loading. The incorporation of fiber breakage in the model and subsequently in the DMN framework is uninvestigated. The developed framework can be utilized for component simulation with varying spatial response, however with additional speed-up employing sparse matrices in the DMN online phase [72]. Furthermore, extending the DMN assisted virtual characterization to interpolate over other geometric parameters such as fiber length and subsequently capturing microstructure uncertainty [74] may be worthwhile.

Bibliography

[1] S. Brinkmann and E. Schmachtenberg, *Saechtling Kunststoff Taschenbuch.* Carl Hanser Verlag GmbH Co KG, 2013.

[2] J. Denault, T. Vu-Khanh, and B. Foster, "Tensile properties of injection molded long fiber thermoplastic composites," *Polymer Composites*, vol. 10, no. 5, pp. 313–321, 1989.

[3] J. Thomason, "The influence of fibre properties of the performance of glass-fibre-reinforced polyamide 6, 6," *Composites Science and Technology*, vol. 59, no. 16, pp. 2315–2328, 1999.

[4] G. Meneghetti, M. Ricotta, G. Lucchetta, and S. Carmignato, "An hysteresis energy-based synthesis of fully reversed axial fatigue behaviour of different polypropylene composites," *Composites Part B: Engineering*, vol. 65, pp. 17–25, 2014.

[5] N. Jia and V. A. Kagan, "Effects of time and temperature on the tension-tension fatigue behavior of short fiber reinforced polyamides," *Polymer composites*, vol. 19, no. 4, pp. 408–414, 1998.

[6] A. Hassan, N. A. Rahman, and R. Yahya, "Moisture absorption effect on thermal, dynamic mechanical and mechanical properties of injection-molded short glass-fiber/polyamide 6, 6 composites," *Fibers and Polymers*, vol. 13, pp. 899–906, 2012.

[7] P. A. Hessman, T. Riedel, F. Welschinger, K. Hornberger, and T. Böhlke, "Microstructural analysis of short glass fiber reinforced thermoplastics based on x-ray micro-computed tomography," *Composites Science and Technology*, vol. 183, p. 107752, 2019.

[8] F. Welschinger, J. Köbler, H. Andrä, R. Müller, M. Schneider, and S. Staub, "Efficient multiscale methods for viscoelasticity and fatigue of short fiber-reinforced polymers," in *Key Engineering Materials*, vol. 809, pp. 473–479, 2019.

[9] J. Köbler, N. Magino, H. Andrä, F. Welschinger, R. Müller, and M. Schneider, "A computational multi-scale model for the stiffness degradation of short-fiber reinforced plastics subjected to fatigue loading," *Computer Methods in Applied Mechanics and Engineering*, vol. 373, p. 113522, 2021.

[10] S. Gajek, *Deep material networks for efficient scale-bridging in thermomechanical simulations of solids.* Doctoral thesis, Karlsruher Institut für Technologie (KIT), 2023.

[11] A. P. Dey, F. Welschinger, M. Schneider, S. Gajek, and T. Böhlke, "Training deep material networks to reproduce creep loading of short fiber-reinforced thermoplastics with an inelastically-informed strategy," *Archive of Applied Mechanics*, vol. 92, pp. 2733—-2755, 2022.

[12] A. P. Dey, F. Welschinger, M. Schneider, S. Gajek, and T. Böhlke, "Rapid inverse calibration of a multiscale model for the viscoplastic and creep behavior of short fiber-reinforced thermoplastics based on deep material networks," *International Journal of Plasticity*, vol. 160, p. 103484, 2023.

[13] A. P. Dey, F. Welschinger, M. Schneider, J. Köbler, and T. Böhlke, "On the effectiveness of deep material networks for the multi-scale virtual characterization of short fiber-reinforced thermoplastics under highly nonlinear load cases," *Archive of Applied Mechanics*, vol. 94, pp. 1177–1202, 2024.

[14] T. Mori and K. Tanaka, "Average stress in matrix and average elastic energy of materials with misfitting inclusions," *Acta Metallurgica*, vol. 21, no. 5, pp. 571–574, 1973.

[15] J. R. Willis, "Variational and related methods for the overall properties of composites," in *Advances in Applied Mechanics*, vol. 21, pp. 1–78, 1981.

[16] Y. Benveniste, "A new approach to the application of Mori-Tanaka's theory in composite materials," *Mechanics of Materials*, vol. 6, no. 2, pp. 147–157, 1987.

[17] R. Hill, "Elastic properties of reinforced solids: some theoretical principles," *Journal of the Mechanics and Physics of Solids*, vol. 11, no. 5, pp. 357–372, 1963.

[18] K. Matouš, M. G. D. Geers, V. G. Kouznetsova, and A. Gillman, "A review of predictive nonlinear theories for multiscale modeling of heterogeneous materials," *Journal of Computational Physics*, vol. 330, pp. 192–220, 2017.

[19] H. Moulinec and P. Suquet, "A fast numerical method for computing the linear and nonlinear mechanical properties of composites," *Comptes Rendus de l'Académie des Sciences. Série II*, vol. 318, no. 11, pp. 1417–1423, 1994.

[20] H. Moulinec and P. Suquet, "A numerical method for computing the overall response of nonlinear composites with complex microstructure," *Computer Methods in Applied Mechanics and Engineering*, vol. 157, pp. 69–94, 1998.

[21] R. A. Lebensohn and A. D. Rollett, "Spectral methods for full-field micromechanical modelling of polycrystalline material," *Computational Materials Science*, vol. 173, p. 109336, 2020.

[22] M. Schneider, "A review of non-linear FFT-based computational homogenization methods," *Acta Mechanica*, vol. 232, pp. 2051–2100, 2021.

[23] S. Lucarini, M. V. Upadhyay, and J. Segurado, "FFT based approaches in micromechanics: fundamentals, methods and applications," *Modelling and Simulation in Materials Science and Engineering*, vol. online, pp. 1–86, 2021.

[24] F. Feyel, "Multiscale FE^2 elastoviscoplastic analysis of composite structures," *Computational Materials Science*, vol. 16, no. 1, pp. 344 – 354, 1999.

[25] F. Feyel and J.-L. Chaboche, "FE^2 multiscale approach for modelling the elastoviscoplastic behaviour of long fibre SiC/Ti composite materials," *Computer Methods in Applied Mechanics and Engineering*, vol. 183, no. 3-4, pp. 309–330, 2000.

[26] F. Feyel, "A multilevel finite element method (FE^2) to describe the response of highly non-linear structures using generalized continua," *Computer Methods in Applied Mechanics and Engineering*, vol. 192, no. 28-30, pp. 3233–3244, 2003.

[27] G. Dvorak, Y. Bahei-El-Din, and A. Wafa, "Implementation of the transformation field analysis," *Computational Mechanics*, vol. 14, no. 14, pp. 201–228, 1994.

[28] G. Dvorak, Y. Bahei-El-Din, and A. Wafa, "The modeling of inelastic composite materials with the transformation field analysis," *Modelling and Simulation in Material Science and Engineering*, vol. 2, no. 2, pp. 571–586, 1994.

[29] J. L. Chaboche, P. Kanouté, and A. Roos, "On the capabilities of mean-field approaches for the description of plasticity in metal matrix composites," *International Journal of Plasticity*, vol. 21, pp. 1409–1434, 2005.

[30] J. C. Michel and P. Suquet, "Nonuniform transformation field analysis," *International Journal of Solids and Structures*, vol. 40, pp. 6937–6955, 2003.

[31] J. Michel and P. Suquet, "Computational analysis of nonlinear composite structures using the nonuniform transformation field analysis," *Computer Methods in Applied Mechanics and Engineering*, vol. 193, pp. 5477–5502, 2004.

[32] J.-C. Michel and P. Suquet, "A model-reduction approach in micromechanics of materials preserving the variational structure of constitutive relations," *Journal of the Mechanics and Physics of Solids*, vol. 90, pp. 254–285, 2016.

[33] F. Fritzen and T. Böhlke, "Nonuniform transformation field analysis of materials with morphological anisotropy," *Composites Science and Technology*, vol. 71, no. 4, pp. 433–442, 2011.

[34] F. Fritzen and T. Böhlke, "Reduced basis homogenization of viscoelastic composites," *Composites Science and Technology*, vol. 76, pp. 84–91, 2013.

[35] R. Largenton, J.-C. Michel, and P. Suquet, "Extension of the nonuniform transformation field analysis to linear viscoelastic composites in the presence of aging and swelling," *Mechanics of Materials*, vol. 73, pp. 76–100, 2014.

[36] F. Fritzen and M. Leuschner, "Reduced basis hybrid computational homogenization based on a mixed incremental formulation," *Computer Methods in Applied Mechanics and Engineering*, vol. 260, pp. 143–154, 2013.

[37] J.-C. Michel and P. Suquet, "A model-reduction approach to the micromechanical analysis of polycristalline materials," *Computational Mechanics*, vol. 57, no. 3, pp. 483–508, 2016.

[38] J.-C. Michel and P. Suquet, "Effective potentials in nonlinear polycrystals and quadrature formulae," *Proceedings of the Royal Society A*, vol. 473, p. 20170213, 2017.

[39] Z. Liu, M. A. Bessa, and W. K. Liu, "Self-consistent clustering analysis: An efficient multi-scale scheme for inelastic heterogeneous materials," *Computer Methods in Applied Mechanics and Engineering*, vol. 306, pp. 319–341, 2016.

[40] S. Wulfinghoff, F. Cavaliere, and S. Reese, "Model order reduction of nonlinear homogenization problems using a Hashin-Shtrikman type finite element method," *Computer Methods in Applied Mechanics and Engineering*, vol. 330, pp. 149–179, 2018.

[41] M. Schneider, "On the mathematical foundations of the self-consistent clustering analysis for non-linear materials at small strains," *Computer Methods in Applied Mechanics and Engineering*, vol. 354, pp. 783–801, 2019.

[42] J. Oliver, M. Caicedo, A. E. Huespe, J. A. Hernández, and E. Roubin, "Reduced order modeling strategies for computational multiscale fracture," *Computer Methods in Applied Mechanics and Engineering*, vol. 313, pp. 560–595, 2017.

[43] M. Raschi, O. Lloberas-Valls, A. Huespe, and J. Oliver, "High performance reduction technique for multiscale finite element modeling (HPR-FE2): Towards industrial multiscale FE software," *Computer Methods in Applied Mechanics and Engineering*, vol. 375, p. 113580, 2021.

[44] H. Moulinec and P. Suquet, "A numerical method for computing the overall response of nonlinear composites with complex microstructure," *Computer Methods in Applied Mechanics and Engineering*, vol. 157, no. 1-2, pp. 69–94, 1998.

[45] D. J. Eyre and G. W. Milton, "A fast numerical scheme for computing the response of composites using grid refinement," *The European Physical Journal-Applied Physics*, vol. 6, no. 1, pp. 41–47, 1999.

[46] J. Spahn, H. Andrä, M. Kabel, and R. Müller, "A multiscale approach for modeling progressive damage of composite materials using fast Fourier transforms," *Computer Methods in Applied Mechanics and Engineering*, vol. 268, pp. 871–883, 2014.

[47] M. Schneider, F. Ospald, and M. Kabel, "Computational homogenization of elasticity on a staggered grid," *International Journal for Numerical Methods in Engineering*, vol. 105, no. 9, pp. 693–720, 2016.

[48] J.-C. Michel and P. Suquet, "Nonuniform transformation field analysis," *International Journal of Solids and Structures*, vol. 40, no. 25, pp. 6937–6955, 2003.

[49] T. Guo, O. Rokoš, and K. Veroy, "A reduced order model for geometrically parameterized two-scale simulations of elasto-plastic microstructures under large deformations," *Computer Methods in Applied Mechanics and Engineering*, vol. 418, p. 116467, 2024.

[50] B. Le, J. Yvonnet, and Q.-C. He, "Computational homogenization of nonlinear elastic materials using neural networks," *International Journal for Numerical Methods in Engineering*, vol. 104, no. 12, pp. 1061–1084, 2015.

[51] V. M. Nguyen-Thanh, L. T. K. Nguyen, T. Rabczuk, and X. Zhuang, "A surrogate model for computational homogenization of elastostatics at finite strain using high-dimensional model representation-based neural network," *International Journal for Numerical Methods in Engineering*, vol. 121, no. 21, pp. 4811–4842, 2020.

[52] Y. Shen, K. Chandrashekhara, W. Breig, and L. Oliver, "Neural network based constitutive model for rubber material," *Rubber Chemistry and Technology*, vol. 77, no. 2, pp. 257–277, 2004.

[53] M. N. Jadid, "Prediction of stress-strain relationships for reinforced concrete sections by implementing neural network techniques," *Journal of King Saud University-Engineering Sciences*, vol. 9, no. 2, pp. 169–188, 1997.

[54] D. Penumadu and R. Zhao, "Triaxial compression behavior of sand and gravel using artificial neural networks (ANN)," *Computers and Geotechnics*, vol. 24, no. 3, pp. 207–230, 1999.

[55] G. Srinivasu, R. Rao, T. Nandy, and A. Bhattacharjee, "Artificial neural network approach for prediction of titanium alloy stress-strain curve," *Procedia Engineering*, vol. 38, pp. 3709–3714, 2012.

[56] A. Zhang and D. Mohr, "Using neural networks to represent von Mises plasticity with isotropic hardening," *International Journal of Plasticity*, vol. 132, p. 102732, 2020.

[57] D. W. Abueidda, S. Koric, N. A. Sobh, and H. Sehitoglu, "Deep learning for plasticity and thermo-viscoplasticity," *International Journal of Plasticity*, vol. 136, p. 102852, 2021.

[58] D. P. Jang, P. Fazily, and J. W. Yoon, "Machine learning-based constitutive model for J2-plasticity," *International Journal of Plasticity*, vol. 138, p. 102919, 2021.

[59] C. Settgast, G. Hütter, M. Kuna, and M. Abendroth, "A hybrid approach to simulate the homogenized irreversible elastic–plastic deformations and damage of foams by neural networks," *International Journal of Plasticity*, vol. 126, p. 102624, 2020.

[60] M. Al-Haik, M. Hussaini, and H. Garmestani, "Prediction of nonlinear viscoelastic behavior of polymeric composites using an artificial neural network," *International Journal of Plasticity*, vol. 22, no. 7, pp. 1367–1392, 2006.

[61] M. Raissi, P. Perdikaris, and G. E. Karniadakis, "Physics-informed neural networks: A deep learning framework for solving forward and inverse problems involving nonlinear partial differential equations," *Journal of Computational physics*, vol. 378, pp. 686–707, 2019.

[62] L. Wu, N. G. Kilingar, and L. Noels, "A recurrent neural network-accelerated multi-scale model for elasto-plastic heterogeneous materials subjected to random cyclic and non-proportional loading paths," *Computer Methods in Applied Mechanics and Engineering*, vol. 369, p. 113234, 2020.

[63] F. Ghavamian and A. Simone, "Accelerating multiscale finite element simulations of history-dependent materials using a recurrent neural network," *Computer Methods in Applied Mechanics and Engineering*, vol. 357, p. 112594, 2019.

[64] S. B. Tandale and M. Stoffel, "Recurrent and convolutional neural networks in structural dynamics: a modified attention steered encoder–decoder architecture versus lstm versus gru versus tcn topologies to predict the response of shock wave-loaded plates," *Computational Mechanics*, vol. 72, no. 4, pp. 765–786, 2023.

[65] L. Linden, D. K. Klein, K. A. Kalina, J. Brummund, O. Weeger, and M. Kästner, "Neural networks meet hyperelasticity: A guide to enforcing physics," *Journal of the Mechanics and Physics of Solids*, vol. 179, p. 105363, 2023.

[66] M. Franke, D. K. Klein, O. Weeger, and P. Betsch, "Advanced discretization techniques for hyperelastic physics-augmented neural networks," *Computer Methods in Applied Mechanics and Engineering*, vol. 416, p. 116333, 2023.

[67] D. K. Klein, R. Ortigosa, J. Martínez-Frutos, and O. Weeger, "Finite electro-elasticity with physics-augmented neural networks," *Computer Methods in Applied Mechanics and Engineering*, vol. 400, p. 115501, 2022.

[68] D. K. Klein, R. Ortigosa, J. Martínez-Frutos, and O. Weeger, "Nonlinear electro-elastic finite element analysis with neural network constitutive models," *Computer Methods in Applied Mechanics and Engineering*, vol. 425, p. 116910, 2024.

[69] Z. Liu, C. Wu, and M. Koishi, "A deep material network for multiscale topology learning and accelerated nonlinear modeling of heterogeneous materials," *Computer Methods in Applied Mechanics and Engineering*, vol. 345, pp. 1138–1168, 2019.

[70] Z. Liu and C. Wu, "Exploring the 3D architectures of deep material network in data-driven multiscale mechanics," *Journal of the Mechanics and Physics of Solids*, vol. 127, pp. 20–46, 2019.

[71] S. Gajek, M. Schneider, and T. Böhlke, "On the micromechanics of deep material networks," *Journal of the Mechanics and Physics of Solids*, vol. 142, p. 103984, 2020.

[72] S. Gajek, M. Schneider, and T. Böhlke, "An FE-DMN method for the multiscale analysis of short fiber reinforced plastic components," *Computer Methods in Applied Mechanics and Engineering*, vol. 384, p. 113952, 2021.

[73] V. D. Nguyen and L. Noels, "Interaction-based material network: A general framework for (porous) microstructured materials," *Computer Methods in Applied Mechanics and Engineering*, vol. 389, p. 114300, 2022.

[74] N. Meyer, S. Gajek, J. Görthofer, A. Hrymak, L. Kärger, F. Henning, M. Schneider, and T. Böhlke, "A probabilistic virtual process chain to quantify process-induced uncertainties in sheet molding compounds," *Composites Part B: Engineering*, p. 110380, 2022.

[75] S. Gajek, M. Schneider, and T. Böhlke, "An FE-DMN method for the multiscale analysis of thermodynamical composites," *Computational Mechanics*, vol. 69, p. 1087–1113, 2022.

[76] Z. Liu, H. Wei, T. Huang, and C. Wu, "Intelligent multiscale simulation based on process-guided composite database," *arXiv preprint arXiv:2003.09491*, 2020.

[77] E. N. D. C. Andrade, "On the Viscous Flow in Metals, and Allied Phenomena," *Proceedings of the Royal Society of London. Series A, Containing Papers of a Mathematical and Physical Character*, vol. 84, no. 567, pp. 1–12, 1910.

[78] K. Naumenko and H. Altenbach, *Modeling of Creep for Structural Analysis*. Foundations of Engineering Mechanics, Berlin, Heidelberg: Springer Berlin Heidelberg, 2007.

[79] F. H. Norton, *The creep of steel at high temperatures*. McGraw-Hill Book Company, 1929.

[80] F. K. Odqvist, "Creep stresses in a rotating disc," in *Proceedings of 4th International Congress of Applied Mechanics*, pp. 228–229, 1934.

[81] R. W. Bailey, "The utilization of creep test data in engineering design," *Proceedings of the Institution of Mechanical Engineers*, vol. 131, no. 1, pp. 131–349, 1935.

[82] I. N. Rabotnov, I. U. Nikolaevich, and F. A. Leckie, *Creep problems in structural members*. Amsterdam: North-Holland Publishing Company, 1969.

[83] J.-L. Chaboche, "Thermodynamic formulation of constitutive equations and application to the viscoplasticity and viscoelasticity of metals and polymers," *International Journal of Solids and Structures*, vol. 34, no. 18, pp. 2239–2254, 1997.

[84] J. N. Martinez-Guerrero, *Flexural creep analysis of recycled polymeric structural elements*. Doctoral thesis, Louisiana State University and Agricultural & Mechanical College, 1999.

[85] B. Klimkeit, S. Castagnet, Y. Nadot, A. El Habib, G. Benoit, S. Bergamo, C. Dumas, and S. Achard, "Fatigue damage mechanisms in short fiber reinforced PBT+ PET GF30," *Materials Science and Engineering: A*, vol. 528, no. 3, pp. 1577–1588, 2011.

[86] E. Chebbi, J. Mars, M. Wali, and F. Dammak, "Fatigue behavior of short glass fiber reinforced polyamide 66: experimental study and fatigue damage modelling," *Periodica Polytechnica Mechanical Engineering*, vol. 60, no. 4, pp. 247–255, 2016.

[87] L. G. M. Lise, *Investigation of damage evolution due to cyclic mechanical loads and load/frequency spectra-effects in short-fibre-reinforced thermoplastics.* Doctoral thesis, Universidade Federal de Santa Catarina, 2020.

[88] H. Nouri, F. Meraghni, and P. Lory, "Fatigue damage model for injection-molded short glass fibre reinforced thermoplastics," *International Journal of Fatigue*, vol. 31, no. 5, pp. 934–942, 2009.

[89] W. Van Paepegem and J. Degrieck, "A new coupled approach of residual stiffness and strength for fatigue of fibre-reinforced composites," *International Journal of Fatigue*, vol. 24, no. 7, pp. 747–762, 2002.

[90] K. Matouš, M. G. Geers, V. G. Kouznetsova, and A. Gillman, "A review of predictive nonlinear theories for multiscale modeling of heterogeneous materials," *Journal of Computational Physics*, vol. 330, pp. 192–220, 2017.

[91] C. Miehe, M. Hofacker, and F. Welschinger, "A phase field model for rate-independent crack propagation: Robust algorithmic implementation based on operator splits," *Computer Methods in Applied Mechanics and Engineering*, vol. 199, no. 45-48, pp. 2765–2778, 2010.

[92] J. Köbler, M. Schneider, F. Ospald, H. Andrä, and R. Müller, "Fiber orientation interpolation for the multiscale analysis of short fiber reinforced composite parts," *Computational Mechanics*, vol. 61, pp. 729–750, 2018.

[93] N. Magino, J. Köbler, H. Andrä, F. Welschinger, R. Müller, and M. Schneider, "A multiscale high-cycle fatigue-damage model for the stiffness degradation of fiber-reinforced materials based on a mixed variational framework," *Computer Methods in Applied Mechanics and Engineering*, vol. 388, p. 114198, 2022.

[94] J. Görthofer, M. Schneider, A. Hrymak, and T. Böhlke, "A convex anisotropic damage model based on the compliance tensor," *International Journal of Damage Mechanics*, vol. 31, no. 1, pp. 43–86, 2022.

[95] R. H. Peerlings, W. M. Brekelmans, R. de Borst, and M. G. Geers, "Gradient-enhanced damage modelling of high-cycle fatigue," *International Journal for Numerical Methods in Engineering*, vol. 49, no. 12, pp. 1547–1569, 2000.

[96] N. Magino, J. Köbler, H. Andrä, F. Welschinger, R. Müller, and M. Schneider, "A space-time upscaling technique for modeling high-cycle fatigue-damage of short-fiber reinforced composites," *Composites Science and Technology*, vol. 233, p. 109340, 2022.

[97] N. Magino, J. Köbler, H. Andrä, F. Welschinger, R. Müller, and M. Schneider, "Accounting for viscoelastic effects in a multiscale fatigue model for the degradation of the dynamic stiffness of short-fiber reinforced thermoplastics," *Computational Mechanics*, vol. 71, no. 3, pp. 493–515, 2023.

[98] P. Haupt, *Continuum mechanics and theory of materials*. Springer Science & Business Media, 2002.

[99] G. A. Holzapfel, *Nonlinear Solid Mechanics: A Continuum Approach for Engineering Science*. Kluwer Academic Publishers Dordrecht, 2002.

[100] I.-S. Liu, *Continuum mechanics*, vol. 5. Springer, 2002.

[101] N. Halphen and Q. Nguyen, "Sur les Matériaux standards generalisés," *Journal de Mécanique*, vol. 14, pp. 508–520, 1975.

[102] W. Voigt, *Lehrbuch Der Kristallphysik (mit Ausschluß Der Kristalloptik)*, vol. 34. Johnson Repr., 1966.

[103] A. Reuß, "Berechnung der Fließgrenze von Mischkristallen auf grund der Plastizitätsbedingung für Einkristalle.," *ZAMM-Zeitschrift für Angewandte Mathematik und Mechanik*, vol. 9, no. 1, pp. 49–58, 1929.

[104] Z. Hashin and S. Shtrikman, "A variational approach to the theory of the elastic behaviour of multiphase materials," *Journal of the Mechanics and Physics of Solids*, vol. 11, no. 2, pp. 127–140, 1963.

[105] I. Gitman, H. Askes, and L. Sluys, "Representative volume size as a macroscopic length scale parameter," in *5th International Conference on Fracture Mechanics of Concrete and Concrete Structures*, vol. 1, pp. 483–491, 2004.

[106] I. M. Gitman, H. Askes, L. J. Sluys, and O. Lloberas, "The concept of representative volume for elastic, hardening and softening materials," in *Proceedings of XXXII International Summer School-Conference Advance problems in Mechanics*, pp. 180–184, 2004.

[107] P. Suquet, "Elements of homogenization for inelastic solid mechanics," *Homogenization techniques for composite media*, vol. 272, pp. 193–278, 1987.

[108] N. Henkelmann, *Data-driven exact model order reduction for computational multiscale methods to predict high-cycle fatigue-damage in short-fiber reinforced plastics*. Doctoral thesis, Karlsruher Institut für Technologie (KIT), 2023.

[109] I. Goodfellow, Y. Bengio, and A. Courville, *Deep Learning*. Cambridge: MIT Press, 2016.

[110] V. D. Nguyen and L. Noels, "Micromechanics-based material networks revisited from the interaction viewpoint; robust and efficient implementation for multi-phase composites," *European Journal of Mechanics - A/Solids*, vol. 91, p. 104384, 2022.

[111] D. Balzani, D. Brands, and J. Schröder, *Construction of Statistically Similar Representative Volume Elements*, pp. 355–412. Vienna: Springer, 2014.

[112] L. Scheunemann, D. Balzani, D. Brands, and J. Schröder, *Construction of Statistically Similar RVEs*, pp. 219–256. New York: Springer, 2015.

[113] Z. Liu, "Deep material network with cohesive layers: Multi-stage training and interfacial failure analysis," *Computer Methods in Applied Mechanics and Engineering*, vol. 363, p. 112913, 2020.

[114] Z. Liu, "Cell division in deep material networks applied to multiscale strain localization modeling," *Computer Methods in Applied Mechanics and Engineering*, vol. 384, p. 113914, 2021.

[115] F. Ospald, M. Schneider, and M. Kabel, "A model order reduction method for computational homogenization at finite strains on regular grids using hyperelastic laminates to approximate interfaces," *Computer Methods in Applied Mechanics and Engineering*, vol. 309, pp. 476–496, 2016.

[116] J. Fish and T. Belytschko, *A First Course in Finite Elements*. Wiley, 2008.

[117] J. W. Brewer, "A note on Kronecker matrix products and matrix equation systems," *SIAM Journal on Applied Mathematics*, vol. 17, no. 3, pp. 603–606, 1969.

[118] F. Becker, *Entwicklung einer Beschreibungsmethodik für das mechanische Verhalten unverstärkter Thermoplaste bei hohen Deformationsgeschwindigkeiten*. Doctoral thesis, Martin-Luther University Halle-Wittenberg, 2009.

[119] J. Will (Dynardo GmbH), "optiSLang - Robust design optimization(RDO) – key technology for resource-efficient product development and performance enhancement." Accessed 25 July 2023.

[120] Simulia, "Abaqus CAE." Accessed 09 July 2023.

[121] I. Doghri, L. Brassart, L. Adam, and J.-S. Gérard, "A second-moment incremental formulation for the mean-field homogenization of elasto-plastic composites," *International Journal of Plasticity*, vol. 27, no. 3, pp. 352–371, 2011.

[122] K. Breuer and M. Stommel, "RVE modelling of short fiber reinforced thermoplastics with discrete fiber orientation and fiber length distribution," *SN Applied Sciences*, vol. 2, p. 91, 2020.

[123] K. Breuer and M. Stommel, "Prediction of Short Fiber Composite Properties by an Artificial Neural Network Trained on an RVE Database," *Fibers*, vol. 9, no. 2, p. 8, 2021.

[124] R. F. de Paiva, M. Bisiaux, J. Lynch, and E. Rosenberg, "High resolution x-ray tomography in an electron microprobe," *Review of Scientific Instruments*, vol. 67, no. 6, pp. 2251–2256, 1996.

[125] H. Shen, S. Nutt, and D. Hull, "Direct observation and measurement of fiber architecture in short fiber-polymer composite foam through micro-CT imaging," *Composites Science and Technology*, vol. 64, no. 13–14, pp. 2113–2120, 2004.

[126] S. Garcea, Y. Wang, and P. Withers, "X-ray computed tomography of polymer composites," *Composites Science and Technology*, vol. 156, pp. 305–319, 2018.

[127] M. Schneider, "The sequential addition and migration method to generate representative volume elements for the homogenization of short fiber reinforced plastics," *Computational Mechanics*, vol. 59, pp. 247–263, 2017.

[128] S. Montgomery-Smith, W. He, D. Jack, and D. Smith, "Exact tensor closures for the three-dimensional Jeffery's equation," *Journal of Fluid Mechanics*, vol. 680, pp. 321–335, 2011.

[129] S. Montgomery-Smith, D. Jack, and D. E. Smith, "The Fast Exact Closure for Jeffery's equation with diffusion," *Journal of Non-Newtonian Fluid Mechanics*, vol. 166, pp. 343–353, 2011.

[130] M. Kabel, D. Merkert, and M. Schneider, "Use of composite voxels in FFT-based homogenization," *Computer Methods in Applied Mechanics and Engineering*, vol. 294, pp. 168–188, 2015.

[131] M. Kabel, A. Fink, and M. Schneider, "The composite voxel technique for inelastic problems," *Computer Methods in Applied Mechanics and Engineering*, vol. 322, pp. 396–418, 2017.

[132] R. Charière, A. Marano, and L. Gélébart, "Use of composite voxels in FFT based elastic simulations of hollow glass microspheres/polypropylene composites," *International Journal of Solids and Structures*, vol. 182–183, pp. 1–14, 2020.

[133] M. Kabel (Fraunhofer ITWM), "FeelMath – Mechanical and Thermal Properties of Microstructures." Accessed 08 July 2023.

[134] M. Schneider, "On non-stationary polarization methods in FFT-based computational micromechanics," *International Journal for Numerical Methods in Engineering*, vol. 122, no. 22, pp. 6800–6821, 2021.

[135] J. Zeman, J. Vondřejc, J. Novák, and I. Marek, "Accelerating a FFT-based solver for numerical homogenization of periodic media by conjugate gradients," *Journal of Computational Physics*, vol. 229, no. 21, pp. 8065–8071, 2010.

[136] S. Brisard and L. Dormieux, "FFT-based methods for the mechanics of composites: A general variational framework," *Computational Materials Science*, vol. 49, no. 3, pp. 663–671, 2010.

[137] M. Schneider, "A dynamical view of nonlinear conjugate gradient methods with applications to FFT-based computational micromechanics," *Computational Mechanics*, vol. 66, no. 1, pp. 239–257, 2020.

[138] E. Anderson, Z. Bai, C. Bischof, S. Blackford, J. Demmel, J. Dongarra, J. Du Croz, A. Greenbaum, S. Hammarling, A. McKenney, and D. Sorensen, *LAPACK Users' Guide*. Philadelphia, PA: Society for Industrial and Applied Mathematics, third ed., 1999.

[139] L. Schmelzle, "Implementierung und Bewertung eines Deep Material Networks zur Effektiven Beschreibung des Deformationsverhaltens Kurzglasfaserverstärkter Thermoplaste," Master's thesis, Karlsruher Institut für Technologie (KIT), 2020.

[140] A. Paszke, S. Gross, S. Chintala, G. Chanan, E. Yang, Z. DeVito, Z. Lin, A. Desmaison, L. Antiga, and A. Lerer, "Automatic differentiation in PyTorch," *NIPS Autodiff Workshop*, p. 4, 2017.

[141] S. J. Reddi, S. Kale, and S. Kumar, "On the Convergence of Adam and Beyond," *arXiv:1904.09237 [cs, math, stat]*, 2019.

[142] I. Loshchilov and F. Hutter, "SGDR: Stochastic Gradient Descent with Warm Restarts," *arXiv:1608.03983 [cs, math]*, 2017.

[143] M. Kabel, S. Fliegener, and M. Schneider, "Mixed boundary conditions for FFT-based homogenization at finite strains," *Computational Mechanics*, vol. 57, no. 2, pp. 193–210, 2016.

[144] P. Eisenlohr, M. Diehl, R. A. Lebensohn, and F. Roters, "A spectral method solution to crystal elasto-viscoplasticity at finite strains," *International Journal of Plasticity*, vol. 46, pp. 37–53, 2013.

[145] H. Pan, X. Wang, S. Jia, Z. Lu, J. Bian, H. Yang, L. Han, and H. Zhang, "Fiber-induced crystallization in polymer composites: a comparative study on poly (lactic acid) composites filled with basalt fiber and fiber powder," *International Journal of Biological Macromolecules*, vol. 183, pp. 45–54, 2021.

[146] R. Pantani, I. Coccorullo, V. Speranza, and G. Titomanlio, "Modeling of morphology evolution in the injection molding process of thermoplastic polymers," *Progress in Polymer Science*, vol. 30, no. 12, pp. 1185–1222, 2005.

[147] S. Felder, H. Holthusen, S. Hesseler, F. Pohlkemper, T. Gries, J.-W. Simon, and S. Reese, "Incorporating crystallinity distributions into a thermo-mechanically coupled constitutive model for semi-crystalline polymers," *International Journal of Plasticity*, vol. 135, p. 102751, 2020.

[148] H. Shen, S. Nutt, and D. Hull, "Direct observation and measurement of fiber architecture in short fiber-polymer composite foam through micro-CT imaging," *Composites Science and Technology*, vol. 64, no. 13-14, pp. 2113–2120, 2004.

[149] K. Robb, O. Wirjadi, and K. Schladitz, "Fiber orientation estimation from 3D image data: Practical algorithms, visualization, and interpretation," in *7th international conference on hybrid intelligent systems (HIS 2007)*, pp. 320–325, IEEE, 2007.

[150] Synopsys Simpleware^{TM}, "ScanIP." Accessed 24 June 2021.

[151] J. C. Simo and T. J. R. Hughes, *Computational Inelasticity*. New York: Springer, 1998.

[152] Y. Kostenko and K. Naumenko, "Power plant component design using creep and fatigue damage analysis," *Proceedings of the 5th Australasian Congress on Applied Mechanics*, pp. 89–94, 2007.

[153] Y. Gorash, H. Altenbach, and K. Naumenko, "Modeling of primary and secondary creep for a wide stress range: Creep for a wide stress range," *Proceedings in Applied Mathematics and Mechanics*, vol. 8, no. 1, pp. 10207–10208, 2008.

[154] J. Will and T. Most, "Metamodel of optimized prognosis (MoP)-an automatic approach for user friendly parameter optimization," *Weimarer Optimierungs-und Stochastiktage*, vol. 6, 2009.

[155] M. D. McKay, R. J. Beckman, and W. J. Conover, "A comparison of three methods for selecting values of input variables in the analysis of output from a computer code," *Technometrics*, vol. 42, no. 1, pp. 55–61, 2000.

[156] T. Böhlke and C. Brüggemann, "Graphical representation of the generalized Hooke's law," *Technische Mechanik*, vol. 21, no. 2, pp. 145–158, 2001.

[157] S. K. Kugler, A. Kech, C. Cruz, and T. Osswald, "Fiber orientation predictions - a review of existing models," *Journal of Composites Science*, vol. 4, no. 2, p. 69, 2020.

[158] V. Müller and T. Böhlke, "Prediction of effective elastic properties of fiber reinforced composites using fiber orientation tensors," *Composites Science and Technology*, vol. 130, pp. 36–45, 2016.

[159] T. Huang, Z. Liu, C. Wu, and W. Chen, "Microstructure-guided deep material network for rapid nonlinear material modeling and uncertainty quantification," *Computer Methods in Applied Mechanics and Engineering*, vol. 398, p. 115197, 2022.

[160] P. Fernandez-Zelaia, Y. Lee, S. Dryepondt, and M. M. Kirka, "Creep anisotropy modeling and uncertainty quantification of an additively manufactured Ni-based superalloy," *International Journal of Plasticity*, vol. 151, p. 103177, 2022.

[161] M. Schneider, "An FFT-based method for computing weighted minimal surfaces in microstructures with applications to the computational homogenization of brittle fracture," *International Journal for Numerical Methods in Engineering*, vol. 121, pp. 1367–1387, 2020.

[162] F. Ernesti and M. Schneider, "A Fast Fourier Transform based method for computing the effective crack energy of a heterogeneous material on a combinatorially consistent grid," *International Journal for Numerical Methods in Engineering*, vol. 122, pp. 6283–6307, 2021.

[163] F. Ernesti and M. Schneider, "Computing the effective crack energy of heterogeneous and anisotropic microstructures via anisotropic minimal surfaces," *Computational Mechanics*, vol. 69, pp. 45–57, 2022.

[164] G. W. Milton, *The Theory of Composites*. Cambridge: Cambridge University Press, 2002.

[165] S. G. Advani and C. L. Tucker III, "The use of tensors to describe and predict fiber orientation in short fiber composites," *Journal of Rheology*, vol. 31, no. 8, pp. 751–784, 1987.

[166] M. Schneider, "An FFT-based fast gradient method for elastic and inelastic unit cell homogenization problems," *Computer Methods in Applied Mechanics and Engineering*, vol. 315, pp. 846–866, 2017.

[167] M. Schneider, "Superaccurate effective elastic moduli via postprocessing in computational homogenization," *International Journal for Numerical Methods in Engineering*, vol. 123, no. 17, pp. 4119–4135, 2022.

[168] J. Hernández, J. Oliver, A. E. Huespe, M. Caicedo, and J. Cante, "High-performance model reduction techniques in computational multiscale homogenization," *Computer Methods in Applied Mechanics and Engineering*, vol. 276, pp. 149–189, 2014.

[169] R. A. van Tuijl, J. J. Remmers, and M. G. Geers, "Integration efficiency for model reduction in micro-mechanical analyses," *Computational Mechanics*, vol. 62, pp. 151–169, 2018.